UNIVERSITY OF SOUTHAMPTON

FACULTY OF PHYSICAL SCIENCES AND ENGINEERING

Physics

Design and Characterisation of Ultrafast Semiconductor Disk Lasers

by

Andrew P. Turnbull

Thesis for the degree of Doctor of Philosophy

June 2015

UNIVERSITY OF SOUTHAMPTON

ABSTRACT

FACULTY OF PHYSICAL SCIENCES AND ENGINEERING
Physics

Doctor of Philosophy

DESIGN AND CHARACTERISATION OF ULTRAFAST SEMICONDUCTOR DISK LASERS

by Andrew P. Turnbull

In this thesis I present my work on improving the design of semiconductor gain and saturable absorber structures towards the goal of a Watt-level, sub-200 fs mode-locked vertical-external-cavity surface-emitting laser (ML-VECSEL). The performance of ML-VECSELs has increased significantly in recent years with sub-500 fs pulse durations demonstrated at Watt-level average output powers. However, ML-VECSELs with sub-200 fs pulse durations have only been reported with milliwatt average output powers.

Absence of detailed knowledge of the dynamic response of both gain and saturable absorber structures makes it difficult to develop new designs for improved laser performance. It is, therefore, critical to fully characterise the macroscopic parameters of the semiconductor laser structures used in ML-VECSELs. Here, I present the characterisation of ultrafast surface-recombination semiconductor saturable absorbers, with a design that has given the shortest pulse durations from a ML-VECSEL to date. I demonstrate a ML-VECSEL utilising a cavity design based on the extracted absorber parameters that would be suitable for high average mode-locked output powers using surface-recombination absorbers.

An understanding of fundamental mode-locking mechanisms present in ML-VECSELs is vital for optimising structures as pulse durations approach 100 fs. The evolution of the spectral components present from lasing onset and during pulse formation in a ML-VECSEL is measured; identifying three distinct regimes in the spectral evolution. I interpret the measured transients to extract a value for pulse-shortening per cavity round-trip, allowing a qualitative description of pulse formation in ML-VECSELs to be developed.

I present construction and characterisation of a ML-VECSEL containing new "short-microcavity" gain structures that have demonstrated FWHM pulse durations of 193 fs with 1 KW peak output powers; a benchmark result for peak output power from a ML-VECSEL with sub-200 fs pulse duration.

Contents

List of Figures

List of Tables

Acknowledgements

First and foremost I would like to thank my supervisor, Professor Anne Tropper, for her unending support, encouragement and inspiration over the many years. My thanks also go to Dr Keith Wilcox for the rewarding discussions and the invaluable lessons in the art of laser construction.

Thank you to all of the group members I have had the fortune to work with over the years. In particular, Olly Morris , for the infinite enthusiasm he brought to the office, and Robin Head, for his valuable insights and technical help. Thank you Ed Shaw and Theo Chen-Sverre for providing entertaining and informative conversations.

Without the support of the technical staff in the department this work would not have been possible. Thank you to all of the mechanical and electrical workshop staff, who provided beautifully engineered devices, and the teaching lab technicians for letting me borrow lab equipment whenever it was needed.

Thank you to all my collaborators, especially Dr Ian Farrer, Dr Harvey Beere and Alex Hein for providing the samples without which this work would not have been possible and also to the group at ETH-Zürich for allowing me to come and use their equipment.

I am indebted to my friends at the university, particularly Amelie, Matt, Joe, Mark, Duncan, Woody, and Lewis who have helped keep me going throughout the course of my PhD, and those outside of the university who will likely never read this.

Thanks go to my family for constant encouragement, especially my brothers Matt and Frank who have been there with advice and support at any hour of the day.

Last, but by no means least, I would like to thank Suzie Plumb, who has supported me, looked after me, and put up with me over this long and, at times, stressful journey.

Andrew Turnbull

To Suzie

Declaration of Authorship

I, Andrew P. Turnbull , declare that the thesis entitled *Design and Characterisation of Ultrafast Semiconductor Disk Lasers* and the work presented in the thesis are both my own, and have been generated by me as the result of my own original research. I confirm that:

- this work was done wholly or mainly while in candidature for a research degree at this University;
- where any part of this thesis has previously been submitted for a degree or any other qualification at this University or any other institution, this has been clearly stated;
- where I have consulted the published work of others, this is always clearly attributed;
- where I have quoted from the work of others, the source is always given. With the exception of such quotations, this thesis is entirely my own work;
- I have acknowledged all main sources of help;
- where the thesis is based on work done by myself jointly with others, I have made clear exactly what was done by others and what I have contributed myself;
- parts of this work have been published as in my list of publications

Signed:.....

Date:.....

Chapter 1

Introduction

The vertical-external-cavity surface-emitting laser (VECSEL) is a semiconductor laser that combines the high-output power and good beam quality of diode-pumped solid-state lasers with the design flexibility and cheap cost of semiconductor materials. Since the first demonstration by Kuznetsov et al. (1997), device performance has improved significantly and as a result they have attracted much interest as a compact laser source for applications.

The external laser cavity is formed around an epitaxially grown semiconductor gain structure. The flexibility of the semiconductor materials used gives 3 distinct advantages over other doped crystal or glass solid-state gain media. First, semiconductor fabrication allows several hundred laser devices to be manufactured from a single wafer, greatly reducing the overall device cost.

Second, being epitaxially grown structures, there is inherent flexibility in the layer structure design of the gain region. Gain structures can be optimised for the required laser application, for example, they can be engineered for high average output powers (Heinen et al. (2012)) or ultra-short pulse durations (Klopp et al. (2011); Quarterman et al. (2009)).

Third, the fundamental emission wavelength of a VECSEL can be tailored through choice of semiconductor materials and composition, rather than being restricted to direct

atomic transitions. Continuous-wave (CW) VECSELs have been demonstrated operating at wavelengths up to 5 μm using PbTE material systems (Rahim et al. (2010)). The shortest direct emission wavelength from a VECSEL was using GaInP/AlGaInP/GaAs materials at 674 nm reported by Hastie et al. (2005). The external cavity and optical pumping schemes allow scaling to high powers. 1-μm VECSEL structures using InGaAs QWs have demonstrated the best performance with 106 W of average output power in multi-mode operation reported by Heinen et al. (2012).

The cavity formed by external spherical mirrors produces excellent beam quality and facilitates the inclusion of additional cavity elements. Using intracavity frequency doubling crystals CW-VECSELs with emission wavelengths around 332 nm have been demonstrated by Kahle et al. (2014). Intracavity frequency doubled CW-VECSELs with a 532 nm emission wavelength have had much interest as low-noise pump sources for commercial solid-state mode-locked lasers and are commercially available with average output powers up to 20 W (Coherent Inc.).

Pulsed laser sources operate by emitting intense bursts of light in the form of optical pulses and have been developed to cover a wide range of applications including material processing, communication, medical science and many more (Webb and Jones (2004)). Typical methods of forming optical pulses from a laser cavity include Q-switching, active mode-locking, and passive mode-locking. Mode-locking is the formation of pulses by imposing a fixed phase relationship between each cavity mode that makes up the optical spectrum of the laser. The addition of the phase-locked modes generates an ultrashort pulse circulating in the cavity.

In Q-switched operation, energy is stored in a gain medium in a cavity with very high loss. The losses are then reduced to a small value and the pulse is allowed to build. The laser is switched between these low and high Q-factor states either actively or passively to emit trains of pulses. Q-switching is used to generate relatively long ($\sim$ ns) pulses with large ($\sim$ mJ) pulse energies with repetition rates typically in the range of 1-100 KHz with little coherence between each pulse. The short nanosecond upperstate lifetime in VECSEL gain structures results low energy storage by the gain medium and

in suppression of Q-switching; as a result it is not a viable method of forming pulses using VECSELs.

Active mode-locking relies on actively modulating the cavity losses using an intracavty element such as an acousto-optic modulator (AOM) or electro-optic modulator (EOM). In electrically pumped semiconductor lasers the active region gain can be directly modulated using a sinusoidal drive current. The pulse in an actively mode-locked laser is formed where the cavity loss is the lowest and the pulse shortening effect is provided by the attenuation on the wings of the pulse. The pulse shaping mechanism is relatively weak and therefore actively mode-locked lasers are typically limited to $\sim$ ps pulse durations. For stable operation the drive electronics must be able to accurately match the modulation frequency to the cavity frequency.

Passive mode-locking relies on the introduction of a cavity element that introduces an intensity dependent loss or gain, such as a saturable absorber, making it energetically favourable for the laser to operate in a pulsed regime. Unlike active mode-locking where the modulation of cavity loss is independent of the pulse duration, in passive mode-locking the loss is directly modulated by the passage of the intracavity pulse resulting in loss modulation that occurs faster with shorter pulses.

Figure 1.1 shows three models of passive mode-locking in ultrafast lasers. Passive mode-locking is achievable using a fast saturable absorption effect (1.1(a)) which directly follows the temporal profile of the pulse. An example of a fast effect exploited for passive mode-locking is the intensity dependent Kerr lens that causes a self-focussing of laser mode causing high-intensity operation to see less loss in the cavity (Brabec et al. (1992)). Kerr lens mode-locking (KLM) has been used to generate pulses with sub-10-fs pulse durations directly from Ti:Sapphire laser systems (Sutter et al. (1999); Morgner et al. (1999)). Lasers exploiting KLM for the formation of ultrashort pulses typically have cavities that operate on the edge of stability leading to reduced long term laser stability and critical cavity design. Kerr lens mode-locked lasers typically require some perturbation of the initial cavity to begin mode-locking or they can be started and stabilized by the inclusion of a slow saturable absorber in the cavity (Kaertner et al. (1995)).

Mode-locking can also be achieved using saturable absorbers with a recovery time long on the time scale of the pulse (1.1(b)) such as a semiconductor saturable absorber mirrors (SESAMs). For the work presented in this thesis I will be solely considering the passive mode-locking of VECSELs using SESAMs. Slow saturable absorbers typically exhibit self-starting mode-locking with stable trains of pulses (Paschotta and Keller (2001)). Cavity design for SESAM mode-locked lasers is only semi-critical; it is only the mode-area on the absorber and the saturation fluence that directly influences the saturation and hence the pulse formation.

For pulse durations on the order of picoseconds the formation of a passively mode-locked pulse is balanced by the pulse shortening from the slow saturable loss and the lengthening from a finite gain bandwidth. As pulse durations decrease towards several hundred femtoseconds it, at first, seems that the direct modulation from the slow absorber is not fast enough to support stable trains of pulses. At femtosecond pulse durations the effect of chromatic dispersion and non-linear phase shifts such as self-phase modulation (SPM) cause significant pulse lengthening. The change in phase of the optical modes results in a spreading of the energy from the pulse and hence an increase in pulse length. In order to reach femtosecond pulse durations the phase changing effects in the cavity must be balanced to reach a quasi-soliton mode-locking regime which allows the pulses to be shortened well below the recombination times of the saturable absorber used (Paschotta et al. (2002)). Quasi-soliton mode-locking in passively mode-locked VECSELs (ML-VECSELs) was confirmed by Hoffmann et al. (2010).

The epitaxial growth and design of semiconductor gain and SESAM structures gives an advantage over the solid-state gain media that rely on soliton-like mode-locking to reach ultrashort pulse durations. In soliton mode-locked solid-state lasers the intrinsic chromatic dispersion and non-linear phase introduced by the gain medium are typically compensated by either prism pairs or chirped mirrors to ensure that the net phase change per round trip is zero. By carefully designing the semiconductor structures it is possible to introduce dispersion compensation directly into both gain and SESAM structures, resulting in a simplified cavity design with fewer elements. Through engineering of the

SESAM it is also possible to develop a structure with parameters that are well suited to mode-locking with VECSEL gain structures.

Fundamental Repetition rates of passively mode-locked VECSELs are on the order of GHz due to the ∼nanosecond upper-sate gain lifetime. In the GHz regime SESAM mode-locked diode-pumped solid-state lasers (DPSSLs) are the current competitive laser sources with sub-100 fs pulse duration with Watt-level average output powers (Klenner et al. (2014)). However, at multi-GHz repetition rates DPSSLs suffer from Q-switching instabilities caused by small gain cross-sections and low pulse energies which limits achievable laser performance. In spite of the technical difficulty high performance has been achieved at multi-GHz repetition rates although with longer pulse durations (Okhrimchuk and Obraztsov (2015); Pekarek et al. (2012)). Semiconductor gain with its short upper-state lifetime and large gain cross-section is intrinsically capable of supporting pulses at high GHz repetition rates. However, in order for ML-VECSELs to be competitive laser sources and to take advantage of the low mass-production cost, mode-locked performance must be improved in-line with that of the current state-of-the-art DPSSLs.

Passively ML-VECSELs were first demonstrated by Hoogland et al. (2000). By including a SESAM in the external cavity, the ML-VECSEL emitted 22-ps pulses at a repetition rate of 4.4 GHz. Through optimisation of gain and absorber designs for mode-locked operation, Garnache et al. (2002) demonstrated the first sub-500 fs pulses from a ML-VECSEL with FWHM pulse duration of 477 fs, 100-mW average output power and a repetition rate of 1.21 GHz. Through power-scaling the first Watt-level ML-VECSEL was reported by Hoffmann et al. (2011) emitting a train of 784-fs pulses at a repetition rate of 5.4 GHz. The current benchmark for average power from a ML-VECSEL was demonstrated by Scheller et al. (2012) who reported an average power of 5.1 W and pulse durations of 682 fs. Laurain et al. (2013) demonstrated peak powers up to 13.3 KW with a pulse duration of 800 fs. 4.35 KW have been reported by Wilcox et al. (2013) from a ML-VECSEL with an average power of 3.3 W and a pulse duration of 400 fs. The shortest reported pulse durations are 60 fs in pulse groups (Quarterman et al. (2009)) and 107 fs for single pulses (Klopp et al. (2011)).

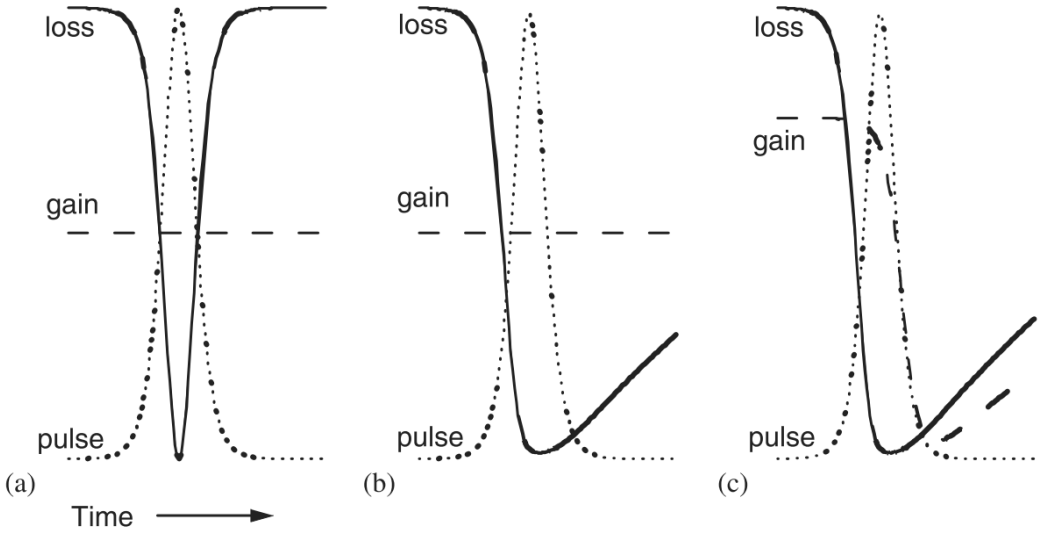

Figure 1.1: Three models of passive mode-locking in ultrafast lasers. (a) fast saturable absorber mode-locking where the recovery time of the absorber occurs on time-scales shorter than the pulse. (b) slow saturable absorber mode-locking without dynamic gain saturation where the absorber recovers on time-scales long compared to the pulse duration. (c) slow saturable absorber mode-locking with dynamic gain saturation where both gain and absorber saturate to form a short window of net gain. Figure from Keller and Tropper (2006).

The above mode-locked results all use lasers operating around 1000-nm in InGaAs/AlGaAs material systems which exhibit best VECSEL performance. SESAM ML-VECSELs have been demonstrated at wavelengths above (Rautiainen et al. (2008); Härkönen et al. (2008)) and below (Bek et al. (2013); Ranta et al. (2013)) 1 μm although with reduced performance. Frequency doubling of an InGaAs/AlGaAs based ML-VECSEL was reported by Casel et al. (2005), doubling the fundamental emission of 5.8 ps pulses to 489-nm with 6 mW average output power.

Fundamental repetition rates have been demonstrated from 100 MHz (Zaugg et al. (2013)) to 100 GHz (Mangold et al. (2014)) and repetition rates up to 200 GHz have been reported using harmonic mode-locking (Wilcox et al. (2011a,b); Sieber et al. (2012)). Through the use of an external tapered fibre amplifier, a sub-picosecond harmonically ML-VECSEL has been demonstrated by Saarinen et al. (2015) with an average power of 53 W at a repetition rate of 193 GHz. The capability to tune pulse repetition rates over a broad range has also been demonstrated in several reports (Mangold et al. (2014); Wilcox et al. (2011b); Sieber et al. (2011)).

Recently, SESAM-free mode-locking, or self-mode-locking, in VECSELs has been reported. Initial reports by Chen et al. (2011) and Kornaszewski et al. (2012) demonstrated a self-ML-VECSEL exhibiting sub-picosecond pulses with greater than Watt-level average output powers. The mode-locking mechanism was cited as a self-focussing caused by a non-linear change of refractive index in the gain structure. However, incomplete characterisation of the lasers lead to scepticism about the reported results (Wilcox and Tropper (2013)). The first direct frequency-doubled output of a self-mode-locked VECSEL indicating a mode-locked output was demonstrated by Gaafar et al. (2014). The presence of a non-linear lens formed in a VECSEL gain structure when probed with a pulsed laser source was shown by Quarterman et al. (2015), where the extracted change in focal length was of a magnitude large enough to perturb VECSEL operation. Work on self-mode-locked lasers is outside of the scope of this thesis; I shall be solely concerning myself with the SESAM ML-VECSELs.

The semiconductor nature of gain and SESAM structures allows both to be incorporated into a single cavity element. The Mode-locked Integrated External-Cavity Surface Emitting Laser (MIXSEL) was first demonstrated by Maas et al. (2007) and has since been reported with record average output powers of 6.4 W, albeit with relatively long 22-ps pulses (Rudin et al. (2010)). Mangold et al. (2013) demonstrated the first femtosecond MIXSEL exhibiting 620-fs pulse at a repetition rate of 4.8 GHz with an average output power of 101 mW. Continuous repetition rate tunability from 5 GHz to 100 GHz has also been reported, demonstrating the highest fundamental repetition rate from VECSEL based technology (Mangold et al. (2014)).

In recent years VECSELs have become an attractive source for a range of applications due to the rapid increase in laser performance. VECSELs have been demonstrated as compact sources for single frequency (Scheller et al. (2010)) and broadband (Mihoubi et al. (2008)) THz generation. Morris et al. (2014) has demonstrated GHz ML-VECSELs as an attractive source for two-photon generation used in quantum-information transfer. The feasibility of the VECSEL as a solar-powered orbital laser platform for direct energy transfer has also been demonstrated by Quarterman and Wilcox (2015) who reported designs for efficient solar pumping schemes for VECSEL gain structures.

One topic that has attracted great interest in recent yeas is the use of ML-VECSELs as a compact source of coherent octave-spanning supercontiuum (SC) generation with GHz mode-spacing. An indication that ML-VECSEL performance was reaching a point where octave-spanning SC could be realised arose when Wilcox et al. (2013) demonstrated spectral broadening to 175 nm of a 400 fs pulse launched into a 2-m length of photonic crystal fibre (PCF). Head et al. (2013) reported on a fibre amplified ML-VECSEL used to generate SC bandwidths up to 280 nm. The 20-mW 400-fs fundamental output of a 1040-nm ML-VECSEL was amplified using a 3-stage fibre amplifier up to 40 W with 3 ps pulse durations. The pulses were recompressed to 400 fs before being launched into a 1-m long PCF, after which a SC with 280-nm bandwidth was measured. The generated bandwidth was limited by the amount of average power that could be launched into the PCF before inducing thermal damage in the fibre.

The first coherent octave-spanning SC and carrier-envelope offset (CEO) measurement was performed by Zaugg et al. (2014b), where the output of a 100-mW, 231-fs ML-VECSEL with a repetition rate of 1.75 Ghz was amplified and compressed to 85 fs with 2.2 W average output power. 800 mW of the available power was then launched into a 1.3-m long PCF after which octave-spanning SC was measured. The CEO measurement was performed with an f-2f interferometer and was measured with a signal-to-noise ratio of 17 dB, approximately 10 dB less than measured with a GHz solid-state laser (Pekarek et al. (2011)).

To create a compact source of octave-spanning SC the amplification stages after the ML-VECSEL output must be removed. However, in order for this to happen laser performance needs to increase in line with what has been shown by Zaugg et al. after the amplification stages. Pekarek et al. (2011) investigated the required laser performance to generate octave-spanning SC in a 2-m long highly-nonlinear PCF using a GHz mode-locked Yb:KGW laser. The laser output needed was found to be 100-fs pulse duration with 1 W of average output power at a repetition rate of 1 GHz. Whilst supercontinuum generation is not the sole application of interest, the strict characteristics required serve as a good benchmark for desired ML-VECSEL performance.

Current benchmarks in VECSEL laser performance are limited to either mW-level output powers with around-100-fs pulse durations (Quarterman et al. (2009); Klopp et al. (2011)) or Watt-level average powers at >400-fs pulse durations (Scheller et al. (2012); Wilcox et al. (2013)). In this thesis I approach the required improvement of laser performance from two main directions. The first is the characterisation of laser structures and the investigation of pulse formation dynamics. The second is improved gain structure designs to improve the average output powers achieved by ML-VECSELs at sub-200 fs pulse durations.

1.1 Thesis Overview

In chapter 2 I describe the factors considered for design of the ML-VECSELs. I introduce the design concepts for both gain and absorber structures optimised to build an ultrafast ML-VECSEL. In section 2.1.1.1 I report on new gain structures designed to achieve sub-200 fs pulse durations at higher pulse energies than have been reported in literature to date. Section 2.2 describes the thermal management techniques used in literature to increase the average output power obtained from VECSELs. The chapter concludes with the work I have performed on developing a substrate removal technique for high-power ML-VECSELs and some results from the procedure when applied to VECSEL gain structures grown by the University of Cambridge.

In chapter 3 I provide a description of the pulse formation mechanisms in ML-VECSELs related to the experimentally measurable macroscopic structure parameters. The chapter covers effects from each individual cavity element and how the theory motivates design choices for high-power ML-VECSEL operation. I conclude the chapter with an overview of the reports of predictive modelling of pulse formation in current literature; highlighting the assumptions and limitations due to unmeasured laser parameters.

Knowledge of the macroscopic structure parameters is critical for cavity designs and to evaluate the effect of design choices on laser performance. In chapter 4 I describe the characterisation of 3 surface-recombination SESAMs. Broadband reflectivity measurements are used to ascertain correct growth of the structures. I extract structure

parameters through non-linear reflectivity measurements and compare the results to the current benchmarks put forward in the simulation by Sieber et al. (2013) for a 1-W 200-fs ML-VECSEL. The temporal response of the absorbers is then evaluated through a reflective pump-probe setup to measure the carrier recombination times. I conclude the chapter with an evaluation of how the measured parameters affect VECSEL cavity designs and go on to demonstrate the operation of a low gain-SESAM mode-area ratio VECSEL.

In chapter 5 I report on the work I have performed spectrally resolving the pulse formation in VECSELs. By combining the tempo-spectral technique reported by Head et al. (2014) with the measurement of the fundamental and second harmonic power transients I show the spectral evolution of the pulse from lasing onset to steady-state. The onset of a measured second harmonic signal indicates the initial formation of a self-reproducing pulse circulating in the cavity. When combined with the measured spectrum as a function of time after lasing onset, I can show the spectral behaviour of the laser at the time of mode-locking onset.

The mode-locked results from the new gain structure designs described in section 2.1.1.1 are presented in chapter 6. Initial CW characterisations are performed to ascertain structure performance when compared to existing structure designs. Pulses are observed using two surface-recombination SESAMs designed for 1000 nm and 1030 nm respectively. I also describe mode-locking results from structures designed for high average powers grown by the University of Ulm. The structures investigated in this chapter represent the first investigation into optimising structures for high-power operation at sub-200 fs pulse durations.

I conclude this thesis with a report of the major results in chapter 7 before going onto discuss avenues for further research based on the topics presented here.

Chapter 2

Design of Mode-locked VECSELs for Sub-200-fs Pulse Durations

At the start of my PhD in 2011 there had been only a few reports of ML-VECSELs with pulse durations of below 300 fs (Klopp et al. (2011); Quarterman et al. (2009, 2011)). As discussed in the introduction, for ML-VECSELs to be perceived as competitive ultrafast laser sources improvements in both pulse duration and average power needed to be made. This chapter describes the essential design factors that need to be considered to improve ML-VECSEL performance. Initially I shall describe the key factors for cavity and structure design before discussing thermal management techniques for high average output power operation.

A passively ML-VECSEL consists of an external laser cavity formed around an epitaxially grown semiconductor gain structure and a passive cavity element that introduces saturable loss. For the work in this thesis the saturable cavity element considered is a semiconductor saturable absorber mirror known as a SESAM. The SESAM preferentially selects high intensity pulsed operation by opening up a short window of net gain, as shown in figure 1.1. The SESAMs considered here have recovery rates long compared to the time-scale of the pulse and are typically considered slow saturable absorbers.

The performance of the ML-VECSEL is directly linked to the macroscopic structure and laser parameters listed in table 2.1. The epitaxial growth gives great control over the

semiconductor design allowing optimization of both gain and SESAM structures, and their related macroscopic structure parameters, independently of the overall laser cavity design. We are particularly concerned with the design of structures and parameters suited to high-power ultrafast mode-locked operation.

We require a gain structure with a large gain bandwidth capable of supporting a broad optical laser spectrum. The broader the spectrum the greater the number of laser cavity modes that can contribute to the optical pulse, reducing the pulse length. The phase relation between the cavity modes must be linear to ensure the all modes contribute to the formation of the pulse. In ML-VECSELs the balance of second order dispersion and non-linear phase shifts, such as self-phase modulation (SPM) is required to form ultrafast quasi-soliton pulses (Paschotta et al. (2002)). Large values of small signal gain and gain saturation fluence are required for the ML-VECSEL to support high energy pulses. Gain structure designs optimised for ultrafast pulses are considered in section 2.1.1

The passage of a pulse through a SESAM attenuates the pulse asymmetrically in time giving a pulse shortening effect. The initial temporal wing of the pulse bleaches the saturable loss present allowing the rest of the pulse to propagate without attenuation. It is necessary for the SESAM to fully recover between successive pulses giving rise to the need for fast (∼10s of picoseconds) recovery times. The formation of pulses in ML-VECSELs requires the SESAM to saturate faster than the gain structure (Keller and Tropper (2006)) which motivates the need for a small value of SESAM saturation fluence. The modulation depth must be sufficiently large to modulate the pulse but small enough to not prevent high-power lasing. SESAM structure designs optimised for the formation of ultrashort pulses are considered in section 2.1.3.

Macroscopic Structure and Laser Parameters			
Gain Structure		SESAM	
Small Signal Gain	g_{ss}	Modulation Depth	ΔR
Gain Saturation Fluence	F_{sat}^{gain}	SESAM Saturation Fluence	F_{sat}^{abs}
Gain Bandwidth	Ω_g	Non-saturable Loss	R_{ns}
Upperstate Gain Lifetime	τ_g	Induced Absorption Parameter	F_2
		Fast (Slow) Absorber Recovery Times	$\tau_{fast(slow)}$
Mode-Locked Laser Parameters			
Average Output Power	P_{ave}	Pulse Length	τ
Repetition Rate	f_{rep}	Round-Trip Time	T_{RT}
Gain Mode Area	A_{gain}	SESAM Mode Area	A_{abs}

Table 2.1: Macroscopic gain and SESAM parameters used in structure design. Laser parameters used in characterising ML-VECSEL performance.

2.1 The VECSEL

Figure 2.1 shows a VECSEL cavity in its simplest form, consisting of an optically pumped gain structure and an output coupler mirror. Typical output couplings lie in the range between 0.3% and 2% due to the low-gain nature of the semiconductor quantum-well (QW) based gain structure and are dependent on gain structure design, pumping conditions, and loss added by intracavity elements. The inclusion of extra cavity elements is possible in a cavity design modified from the straight cavity in figure 2.1, to a more complex cavity design, such as the z-cavity configuration shown in figure 2.2. Particularly relevant for the work performed in this thesis is the inclusion of a SESAM for passive mode-locking. Design of the external cavity makes it possible to choose the laser mode area on gain and SESAM as well as cavity length; parameters critical for passively mode-locked laser operation.

The set temperature of the Peltier-controlled heat-sink can be used to adjust the gain and SESAM operating wavelength due to the temperature sensitive nature of the semiconductor gain and absorption profile (Okhotnikov (2010)). It is possible to optimise the

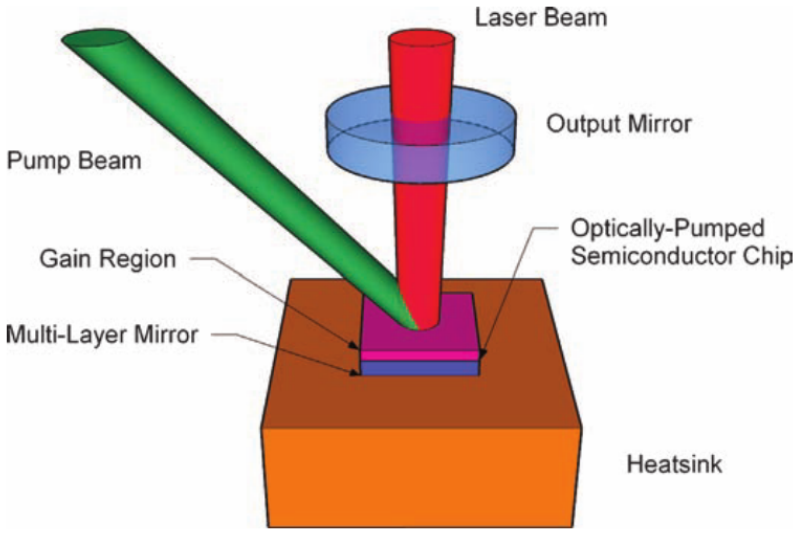

Figure 2.1: Schematic of an optically-pumped VECSEL in a straight cavity configuration. The cavity is formed by the output mirror and the multi-layer mirror at the bottom of the gain structure. The gain is provided by an optically pumped gain region. Figure from Okhotnikov (2010).

laser performance, or better overlap operating wavelengths, through tuning the heat-sink temperature.

2.1.1 Gain Structure Design

In a surface-emitting laser the gain region is contained within a microcavity structure several microns thick which is coupled to an external cavity. The design of this microcavity is crucial for ultrashort pulse generation.

A typical gain structure is a semiconductor "active mirror" device grown by either molecular beam epitaxy (MBE) or metal organic chemical vapour deposition (MOCVD). The epitaxial growth takes place on a semiconductor substrate, which due to lattice matching constraints is GaAs. The growth can be divided into three regions as shown by the schematic in figure 2.3.

The first region is the Distributed Bragg Reflector (DBR), forming a laser mirror in the cavity. The DBR consists of alternating high- and low-index semiconductor materials

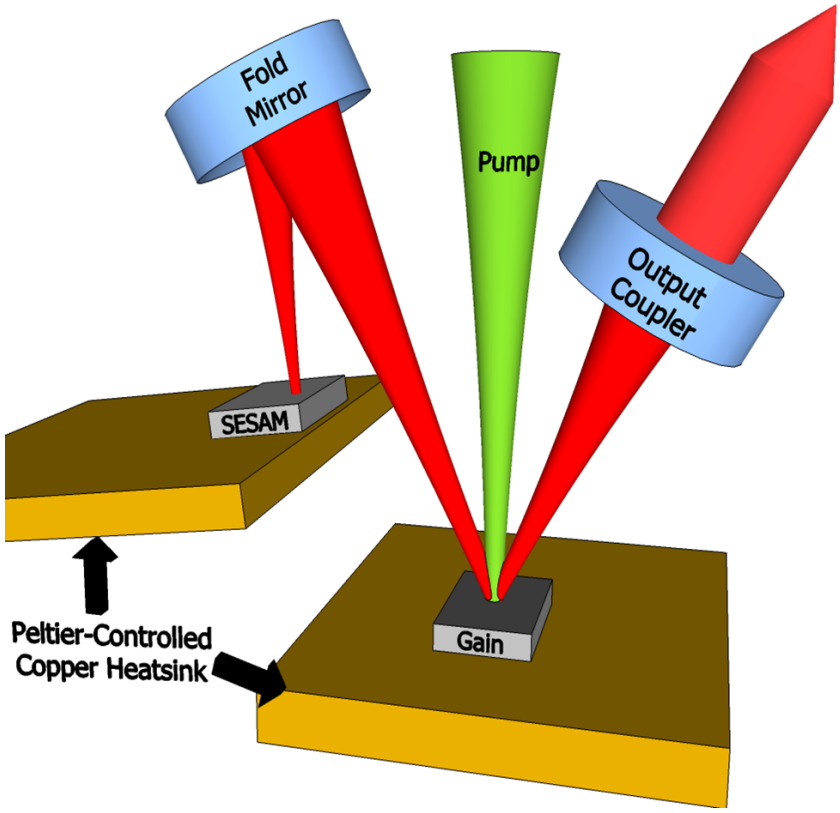

Figure 2.2: Schmatic a z-cavity configuration used for passively mode-locked an optically-pumped VECSEL. The addition of a fold mirror allows the inclusion of a SESAM for mode-locked operation. The fold-mirror - gain distance and the fold-mirror - SESAM distance allow for control of the mode-area size and repetition rate of the laser.

of $\lambda/4$ thickness. For the 1-μm wavelength the materials used are GaAs and AlAs, with 27.5 repeat pairs giving a reflectivity of $\simeq 99.99\%$.

The active region is then grown on top, consisting of QWs to provide gain, separated by bulk pump-absorbing barrier layers. The QWs are situated near the anti-nodes of the electric field at the design wavelength to give a resonant periodic gain design (Corzine et al. (1989)). The emission wavelength can be tailored by adjusting the quantum confinement of the QWs and by altering the semiconductor composition, which changes the material bandgap as shown in figure 2.4. Due to the change in lattice size with semiconductor composition, it may be necessary to include strain-compensation layers to prevent dislocation in the structure; GaP is the semiconductor compound typically used for strain-compensation around 1-μm. All of the structures presented in this thesis

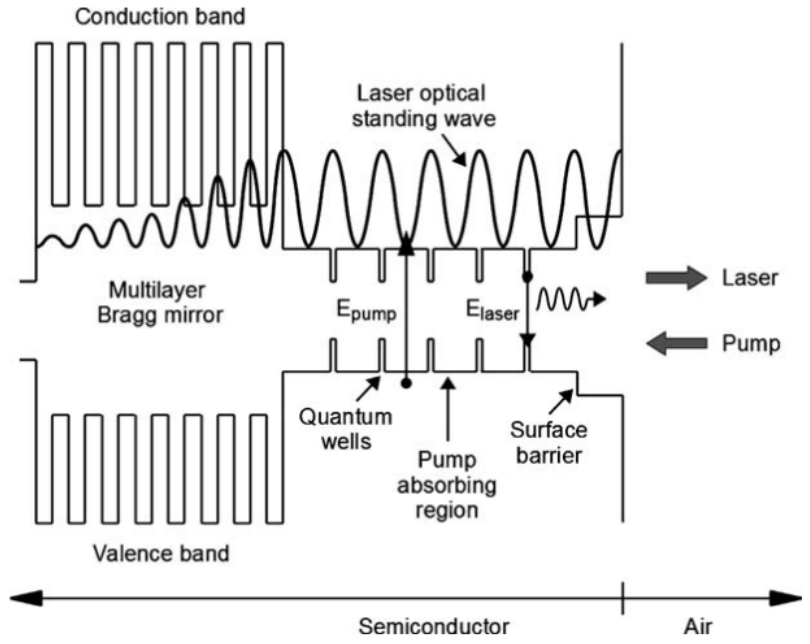

Figure 2.3: Schematic of a typical VECSEL gain structure. The gain is provided by QWs situated at the anti-nodes of the electric field at the design wavelength. The QWs are separated by bulk, pump-absorbing material. A surface barrier is used to prevent non-radiative surface recombination of the carriers whilst also setting the electric field enhancement on the QWs. A multilayer Bragg mirror forms one of the cavity mirrors and is composed of alternating $\lambda/4$ thickness layers of semiconductor material with high refractive index contrast. Figure from Okhotnikov (2010).

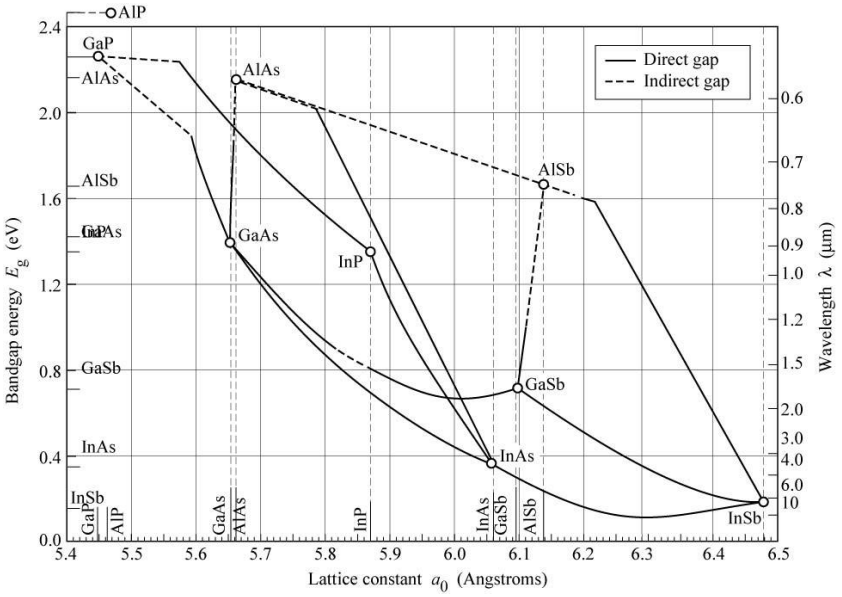

Figure 2.4: Bandgap and emission wavelength of III-V semiconductor materials as a function of lattice constant. The joining lines indicate a ternary material composed of the compounds of the nodes located at the ends of the lines. Figure from Schubert (2006).

are InGaAs/GaAs/AlAs based and have used QWs designed for emission between 1000-nm and 1030-nm.

The final layer is a window layer, whose thickness and composition set the longitudinal confinement factor (LCF), giving a spectrally-dependent enhancement to the gain provided by the QWs. The structure is then capped by a 2-nm thick GaAs layer to prevent surface oxidation. The LCF is a measure of the overlap between the laser field inside the cavity and the active region containing the QWs and governs the strength of the light-matter interaction that provides the laser gain.

In a simple two level laser system the rate of stimulated emission, β_{st}, is proportional to the product of the laser gain, g and the optical intensity of the laser mode, I (Coldren and Corzine (2005)):

$$\begin{aligned} \beta_{st} &\propto g \cdot I \\ &\propto g \cdot |E_0|^2 \end{aligned}$$

where $|E_0|^2$ is the modulus squared of the electric field in the laser cavity. As the microcavity can be designed to alter the electric field penetration into the gain sample, it is therefore necessary to introduce some scaling factor, the LCF, which scales the optical field seen by the QWs. β_{st} then becomes:

$$\beta_{st} \propto \Gamma_z \cdot g \cdot |E_0|^2. \tag{2.1}$$

The LCF is defined by the following relationship:

$$\Gamma_z = n_{QW} \frac{\sum |E(z_n)|^2}{|E_0|^2}, \tag{2.2}$$

where $|E(z_n)|^2$ is the squared modulus of the electric field at the position of the n^{th} QW and n_{QW} is the refractive index of the QW. Γ_z can be calculated using standard

multilayer matrix calculations used to evaluate the penetration of the electric field inside a multi-layer structure (Coldren and Corzine (2005)). The overall modal gain profile, $G(\lambda)$, of the structure is the combination of the LCF and the intrinsic QW gain profile, G_{QW}:

$$G(\lambda) = \Gamma_z(\lambda) \times G_{QW}(\lambda). \tag{2.3}$$

Figure 2.5 shows a schematic of 3 structure designs with different window layers and the resulting LCF.

From the multilayer calculation it is also possible to calculate the group-delay dispersion (GDD) spectral profile for the structure design. The GDD is defined as the second derivative of the spectral phase, ϕ, with respect to the angular frequency, ω:

$$GDD = \frac{\partial^2 \phi}{\partial \omega^2}, \tag{2.4}$$

where the spectral phase is the phase of each oscillating longitudinal laser mode. GDD introduces a spectral phase change:

$$\Delta\phi(\omega) = \frac{GDD}{2}(\omega - \omega_0)^2, \tag{2.5}$$

where ω_0 is the angular frequency at the centre of the optical spectrum. We require the phase relation between the discreet cavity modes to be linear to ensure that all laser modes contribute to the formation of an ultrashort pulse. The GDD profile must be engineered to ensure that the net phase change per cavity round-trip introduced by the interaction of the pulse with the intracavity elements is small. It is necessary to use GDD to balance the phase shifts introduced by non-linear light-matter interactions such as self-phase modulation (SPM) due to the line-width enhancement factor, which are discussed in section 3.2.3. The balance of linear and non-linear phase changes is critical for the quasi-soliton mode-locking present in ML-VECSELs (Paschotta et al. (2002)). Figure 2.6 shows the corresponding GDD profiles to the structures shown in figure 2.5.

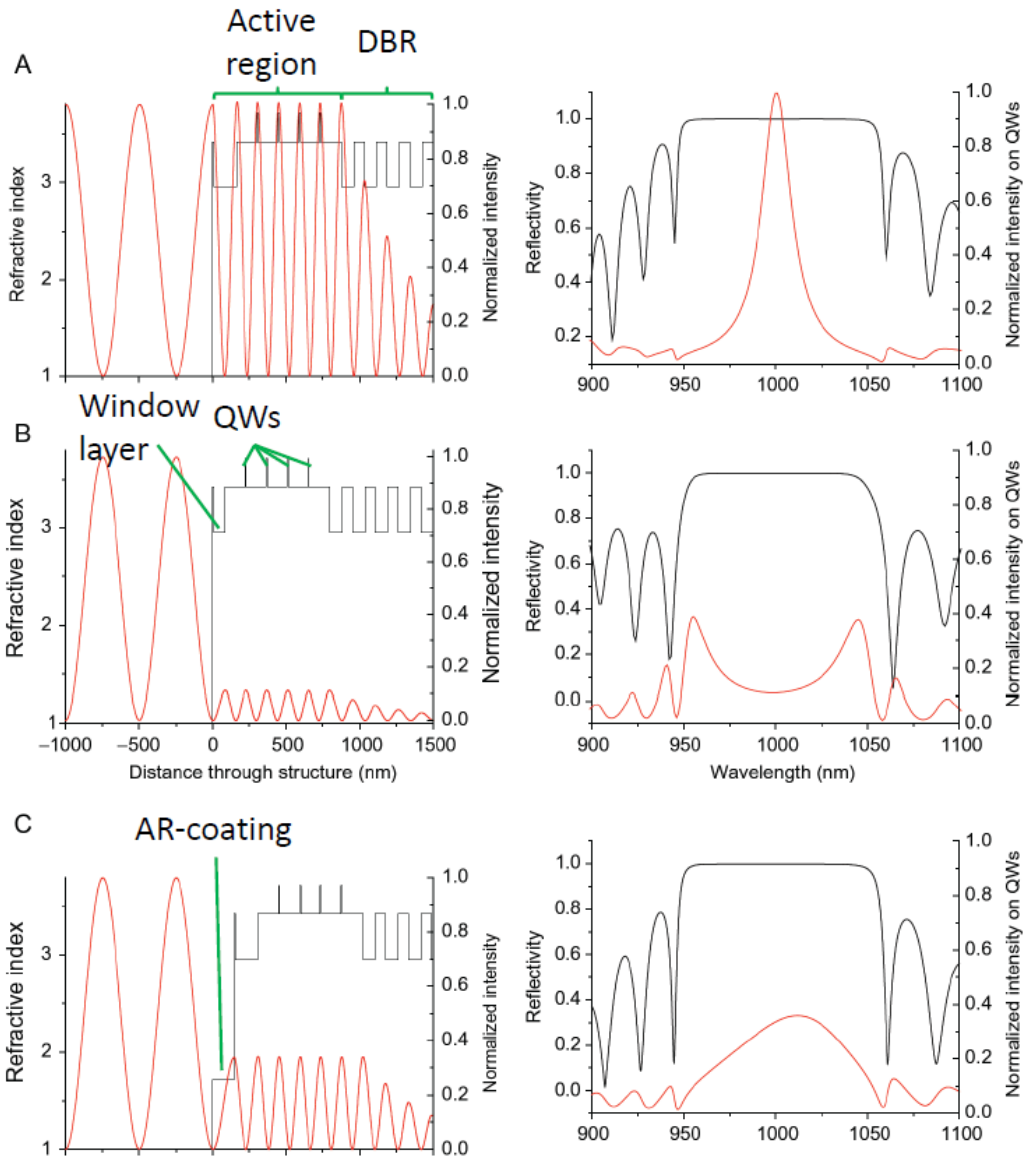

Figure 2.5: Structure designs and spectral characteristics of 1000-nm VECSEL gain chips. The left-hand plots show the structure designs and resulting standing wave intensity as a function of distance through the structure for A) a resonant structure, B) a semiconductor anti-resonant structure and C) a dielectric-AR-coated structure. The right-hand plots show the corresponding longitudinal confinement factors and reflectivity profiles as a function of wavelength. Figure from Tropper et al. (2012).

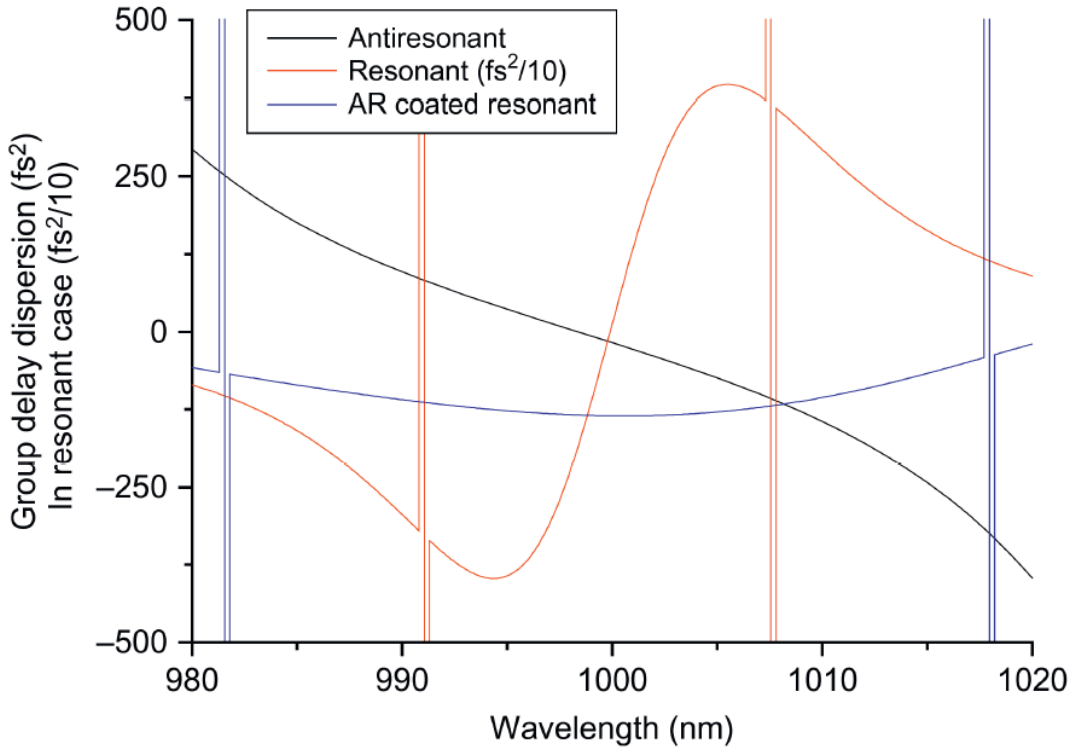

Figure 2.6: GDD as a function of wavelength for the resonant, anti-resonant and dielectric-AR-coated structure designs shown in figure 2.5. Figure from Tropper et al. (2012).

As well as considering the Γ_z and GDD profiles when designing gain structures, it is also necessary to evaluate design choices on macroscopic parameters such as the small signal gain (g_{ss}),gain saturation fluence (F_{sat}^{gain}), and the gain bandwidth (ω_g). The gain saturation fluence is defined as the fluence required to reduce the gain to $1-1/e$ ($\approx$67%) of g_{ss}. I will be discussing the effect of structure design and capping layer thickness and composition on the gain parameters listed in table 2.1.

Figure 2.5 (a) shows a resonant structure. The window layer is set to be $\lambda/2$ thick at the design wavelength which sets an anti-node of the electric field at the air-surface interface, resulting in almost no reduction of electric field intensity. Heinen et al. (2012) have used a resonant structure to demonstrate 100-Watt level average output powers from a CW VECSEL. The sharp peak results in strong enhancement, and maximum gain, at the design wavelength. The enhancement drops off rapidly at higher and lower wavelengths resulting in a narrow spectral gain profile. This, combined with the rapidly changing

GDD shown in figure 2.6 results in a structure that is not suited to the formation of ultrashort pulses and as such has not been considered in this work.

Figure 2.5 (b) and (c) show a semiconductor anti-resonant structure and a single-layer dielectric anti-reflection (AR) coated resonant structure; these two designs form the basis of structures that have achieved the shortest pulses to date (Quarterman et al. (2009); Klopp et al. (2011)). The purpose of these designs is to form a broad gain bandwidth whilst maintaining a low and spectrally invariant GDD profile.

The semiconductor window layer for the anti-resonant structure is $\lambda/4$ thick at the design wavelength setting a node of the electric field at the air-surface interface. The resulting electric field intensity on the QWs is approximately 10% of the value in air at the design wavelength. Above and below the design wavelength the electric field intensity increases, this is opposite to the curvature of the intrinsic QW gain profile and as such should form a broad, flat gain profile. The semiconductor anti-resonant design was first described by Garnache et al. (2002) as a strategy to increase the bandwidth of a VECSEL gain structure for tunable wavelength operation. Although there is a change in the GDD over the gain profile shown in figure 2.6, the overall variation is small around the design wavelength. It is possible to balance change in GDD with a suitably designed SESAM described later.

By applying a $\lambda/4$ thick dielectric coating to the surface of a resonant structure it is possible to broaden the LCF and smooth the GDD profile. There is a reduction of peak enhancement to approximately 30% of the resonant structure, causing a reduction in the small-signal gain. The shape of the LCF will result in a narrowing of the gain profile and subsequent reduction of gain bandwidth but will provide more gain than the semiconductor anti-resonant structure. The addition of the AR layer results in a GDD profile with little variation over the full spectral range.

For ultrafast operation both a broad gain bandwidth and spectrally invariant GDD are required. From the above designs there is a trade-off between the two parameters and it is therefore critical to understand which is the limiting factor for reaching sub-200 fs. From the work performed on solid-state lasers and modelling of ML-VECSELs, GDD is known to become a dominant pulse stretching mechanism as pulse durations move

towards sub-100 fs operation. However, to reach such pulse lengths a weak enough gain filter to reach a spectral bandwidth capable of supporting sub-100 fs pulse durations is required. The work performed at Southampton University has predominately involved the use of semiconductor anti-resonant structures.

For high-power ultrafast mode-locked VECSELs it is necessary to maximise both g_{ss} and F_{sat}^{gain}. Therefore, it is necessary to consider how their magnitudes are affected by gain design choices. g_{ss} and F_{sat}^{gain} are linked to Γ_z by the following relationships: $g_{ss} \propto \Gamma_z$ and $F_{sat}^{gain} \propto \Gamma_z^{-1}$. The value of Γ_z must therefore be chosen to provide a trade-off between small-signal gain and saturation fluence. The structure must have sufficient gain to tolerate the loss associated with the inclusion of a SESAM for passive mode-locking whilst also have a high enough gain saturation energy to support large intracavity pulse energies. It is possible to further increase the small-signal gain by including additional QWs into the active region, however, carrier concentrations and pumping schemes must be considered to ensure threshold can be reached.

The larger enhancement factor in the dielectric AR coated structure will yield greater g_{ss} at the expense of a smaller F_{sat}^{g}, and vice versa for the semiconductor anti-resonant structure. A balance of the two is required for the pursuit of high-average power sub-200 fs operation.

At the start of my PhD, these two basic structure designs formed the core of the work performed on ultrafast mode-locked VECSELs with, in recent years, more complicated structures and dielectric coatings being designed for improved device performance. As yet, these more complex designs have yet to form shorter pulse durations than those presented by Quarterman et al. (2009) and Klopp et al. (2011); although, average output power has been increased at sub-300 fs pulse durations (Zaugg et al. (2014b)). The work performed during my PhD has been to improve existing designs for ML-VECSEL operation below 200 fs whilst also increasing average output power.

2.1.1.1 Short Microcavity Gain Design

It was necessary to improve on current structure designs to push our device performance below 200-fs pulse duration in a single-pulse regime. The gain structure design at the time was a $7\lambda/2$ long active region containing 6 QWs with a $\lambda/4$ window layer to make the structure anti-resonant, resulting in a total microcavity length of $7.5\lambda/2$. This section covers the considerations made when designing a new structure for ultrafast operation.

The current benchmark for single pulses from a ML-VECSEL is 107 fs as demonstrated by Klopp et al. (2011) who used a dielectric-coated AR gain structure containing 3 QWs in a resonant periodic gain configuration with the substrate removed. The output power was limited to 3 mW. Here I describe the rationale behind the use of the semiconductor antiresonant structure containing 4 QWs, W728, used to generate 200 fs pulses with higher average output powers as described in chapter 6.

The limit of the pulse duration observed by Klopp et al. (2011) was the change of operation from a single pulse in a cavity to a multiple-pulse regime. The pulse splitting was due to gain saturation that caused multiple pulses to be energetically favoured in the cavity. The dielectric-AR-coated structure had higher enhancement at the design wavelength and therefore a larger small-signal gain than the semiconductor anti-resonant designs used. The higher enhancement lead to a smaller gain saturation energy which is one of the parameters identified by Sieber et al. (2013) that must be maximised for high-power sub-200 fs operation. The lower LCF, reduced gain and hence increased gain saturation energy makes semiconductor anti-resonant structures an attractive prospect for sub-200 fs pulses and therefore I opted to keep the semiconductor anti-resonant window layer.

The active region acts as a Fabry-Pérot cavity, and its thickness sets the free spectral range (FSR) of the structure. By decreasing the active region thickness we can increase the FSR, resulting in a broader and flatter region of enhancement around the design wavelength. There are downsides of reducing the active region thickness; the reduction in the number of anti-nodes in the electric field limits the number of QWs that can be

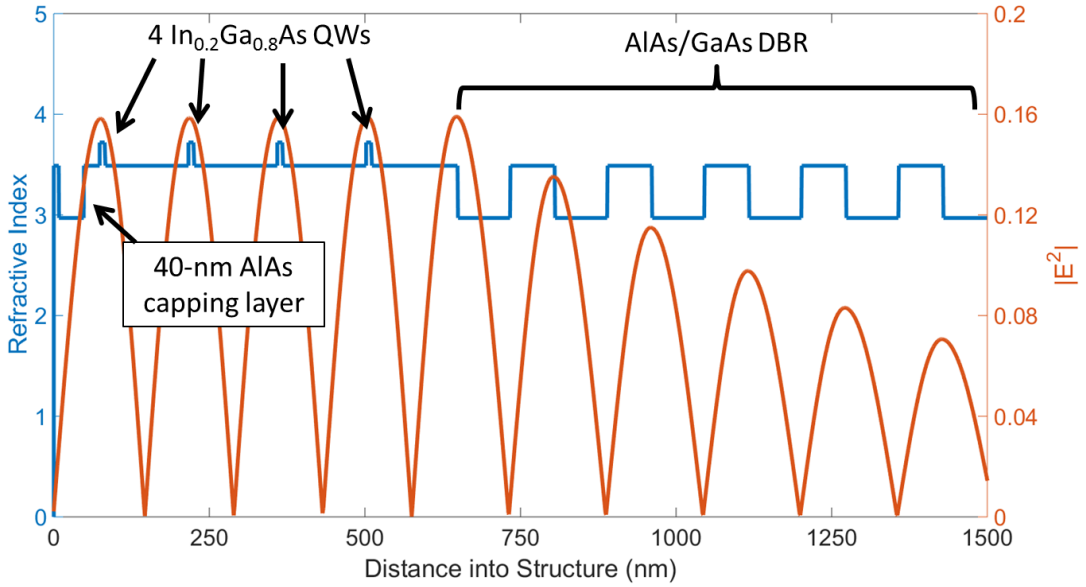

Figure 2.7: Structure of a new "short-microcavity" gain chip design designed for operation at 1000-nm. Overall active region length is $4.5\lambda/2$ and contains 4 InGaAs QWs separated by bulk, pump-absorbing GaAS. The carrier confinement layer is 40-nm AlAs and the structure is capped with 8-nm of GaAs to prevent oxidisation. The active region is grown on a 27.5 pair AlAs/GaAs DBR.

included in the structure reducing the small-signal gain. With a shorter active region there is also less bulk pump-absorbing material which reduces the laser efficiency.

Figure 2.7 shows the layer structure of the new design. The overall length of the active region plus window layer has been shortened to $4.5\lambda/2$. The window layer of this structure is not $\lambda/4$ thick; instead, the whole structure is designed to set a node at the air surface interface and make the structure anti-resonant. The motivation behind this change was to allow the inclusion of an extra QW to provide gain whilst keeping the Fabry-Pérot cavity as short as possible. Figure 2.8 shows a comparison between the LCF and GDD profiles of the existing $7.5\lambda/2$ structure and a new $4.5\lambda/2$ "short microcavity" structure. The "short microcavity" structure shows broader and flatter profiles for both the LCF and GDD and as such is a promising design for the generation of sub-200 fs pulses. The experimental work performed with this structure design is shown in chapter 6.

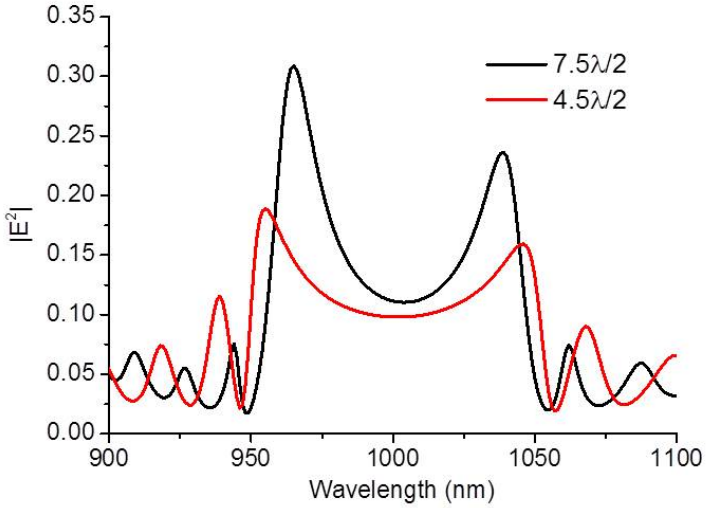

(a)

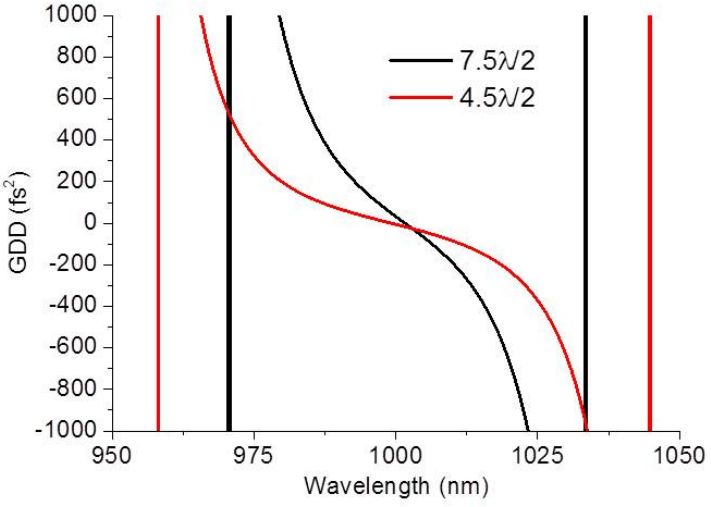

(b)

Figure 2.8: a) Longitundinal confinement factor and b) the GDD profile as function of wavelength for both an existing $7.5\lambda/2$ gain structure and the new "short-microcavity" structure detailed in figure 2.7.

2.1.2 Optical Pumping

Typical pumping schemes in lasers fall into two camps: optical and electrical. The semiconductor nature of VECSELs lends itself well to either scheme due to the inherent electrical properties and device fabrication for electrical pumping and the ability to tailor semiconductor composition for pump absorption in optical pumping.

Electrical pumping of semiconductor lasers is ubiquitous in edge-emitting diode lasers (Coldren and Corzine (2005)) and vertical-cavity surface-emitting lasers (VCSELs) (Jewell et al. (1991)), Whilst edge-emitters can reach very high average output powers due to high gain coefficients they suffer from poor beam quality. VCSELs have good beam quality but are limited to low powers due to the difficulty of keeping uniform pump carrier densities over a large area through the vertical structure. Similar electrical pumping schemes have been applied to VECSELs. These electrically-pumped VECSELs (EP-VECSELs) have had great research interest due to the reduced complexity and footprint, however, they struggle to reach the device performance exhibited by optically pumped VECSELs (Pallmann et al. (2013); Zaugg et al. (2014a)).

The use of an external fibre-coupled diode-based optical pump gives much greater flexibility in laser design, due to the ability to choose the incident spot-size of the pump beam and match it to the cavity mode whilst also tailoring it for the required pump intensities. The ability to scale both incident pump power and spot size to keep constant pump intensity allows easy access to power-scaling to increase average VECSEL output power whilst maintaining good beam quality. Although we rely on an external source for the pumping, increasing the complexity of the setup, there is no extra device fabrication involved. The benchmark high-power results in both CW-VECSELs and ML-VECSEls have been achieved using optically pumped gain structures (Heinen et al. (2012); Scheller et al. (2012); Wilcox et al. (2013)). In this thesis we will be solely considering optically-pumping for the pursuit of high average power ultrafast VECSELs.

2.1.3 Saturable Absorber Design for Passive Mode-locking

To achieve spontaneous passively mode-locked operation an element exhibiting non-linear saturable loss, a saturable absorber, is included in the laser cavity. Standard saturable absorber designs for passively mode-locking VECSELs are SESAMs based on a single QW structure grown on top of a DBR. The SESAM operates by absorbing the leading edge of the temporal pulse which bleaches the QW allowing the rest of the pulse to pass without loss. As SESAMs are slow absorbers the recovery of the absorption takes place on a time-scale longer than the incident pulse. It is possible to achieve pulse durations much shorter than the time-scale of the absorber recovery by operating in a quasi-soliton mode-locking regime where the balance of GDD and SPM serve to shorten the pulse (Paschotta and Keller (2001)). The long recovery of the SESAM aids in stabilization of the pulse train and in reliable self-starting of mode-locked operation. The Keller group at ETH Zürich have pioneered the development and characterisation of saturable absorbers for passive mode-locking in both diode-pumped solid-state lasers and VECSELs (Keller et al. (1992); Kaertner et al. (1995); Keller et al. (1996); Haiml et al. (2004)).

As with the gain structure, design of the absorber structure is critical to optimize the formation of ultrashort pulses. The epitaxial growth of the SESAM structure allows control of the device growth and optimisation of the layer design to create a structure well suited for passively mode-locking VECSELs. The key parameters can be identified and optimized independently of the laser cavity. The supression of Q-switching in ML-VECSELs by the short upper-state gain lifetime lifts some restriction is lifted on the design of SESAMs for use in ML-VECSEls when compared to those used in solid-state lasers (Kaertner et al. (1995)).

Figure 2.9 shows a simulation of the non-linear response of a SESAM as a function of incident pulse fluence. The macroscopic absorber parameters shown, and also listed in table 2.1, are the modulation depth (ΔR), saturation fluence (F_{sat}^{abs}), non-saturable loss (ΔR_{ns}), and induced absorption parameter (F_2). The saturation fluence is defined as the fluence at which the reflectivity of the absorber increases by $1/e$ of the unsaturated

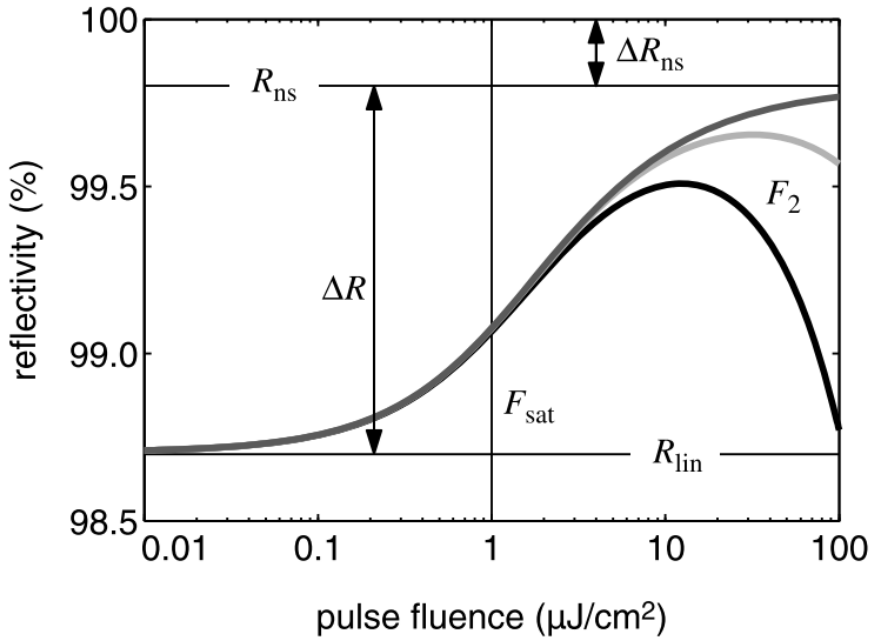

Figure 2.9: Simulated non-linear response of a SESAM showing reflectivity as a function of incident pulse fluence. Initially, the reflectivity increases with fluence. A roll-over in reflectivity due to the induced absorption parameter, F_2, for high fluences. The dark grey curve is simulated with $F_2 = \infty$. The light grey curve has a large value of F_2 and the black curve has a small value of F_2. Figure from Okhotnikov (2010)

reflectivity, R_{lin}. The induced absorption parameter describes the reduction in reflectivity at high fluences dependent on the peak power of the incident pulse. It is defined as the fluence required to reduce the reflectivity to $1/e$ of the value of R_{ns}. The black curve is modelled with a small value of F_2, the light grey curve has a large value of F_2. The dark grey curve is simulated with a value of $F_2 = \infty$.

The recovery time of the absorber plays a key part in the formation of ultrashort pulses as the absorber must recover fully between subsequent pulses. Due to the natural GHz repetition rates of ML-VECSELs this recovery must be on the order of tens of picoseconds. The recovery of an absorber can be split into two mechanisms, as shown by figure 2.10: a fast component, τ_{fast}, and a slow component, τ_{slow}. τ_{fast} is the time constant associated with intra-band thermalization of the carriers which occurs on the order of a few hundred femtoseconds. τ_{slow} is the time-constant for interband carrier recombination which occurs on time-scales between a few picoseconds up to nanoseconds.

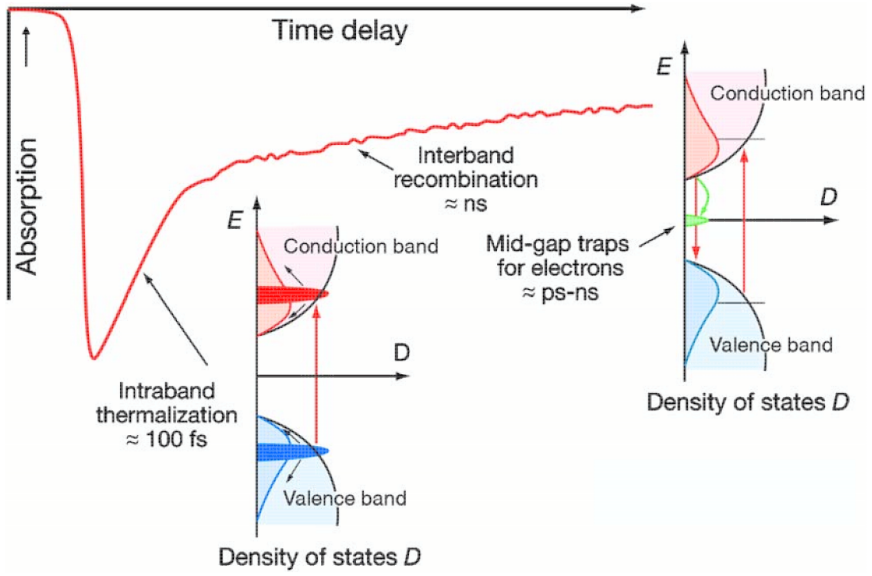

Figure 2.10: Absorption of slow saturable absorber as a function of time after an incident pulse. The absorption decreases until the pulse fully saturates the absorber. The recovery is split into two components. Initially fast intraband thermalization occurs on the order of 100 fs. Interband recombination then takes place over a few ps to ns. Figure from Keller and Tropper (2006)

The key macroscopic parameters for passive mode-locking that must be considered are: F_{sat}^{abs} and ΔR. These parameters are coupled to the electric field enhancement on the QW, Γ_{abs}, by the following relationships: $\Delta \mathrm{R} \propto \Gamma_{abs}$ and $F_{sat}^{abs} \propto \Gamma_{abs}^{-1}$. For passive mode-locking the ratio of F_{sat}^{abs} to F_{sat}^{g} must be less than one, due to the dynamic gain saturation nature of pulse formation in VECSELs, explained in chapter 3. In order to relax cavity constraints on mode-area ratios and reduce local heating of the SESAM, F_{sat} must be minimised. We require ΔR to be sufficiently large to shape the pulse but small enough so that the insertion loss does not prevent laser operation. By increasing Γ_{abs} we can decrease F_{sat} and increase ΔR, however, there is a balance to be sought for high-power operation. Increasing ΔR will reduce the available gain of the laser resulting in lower output powers.

As SESAMs are grown from the same material as the corresponding gain structures, and as such have similar recovery times, material engineering and design choices are required to optimize the absorber for fast recovery whilst also meeting the requirements for low F_{sat}^{abs} and low non-saturable losses.

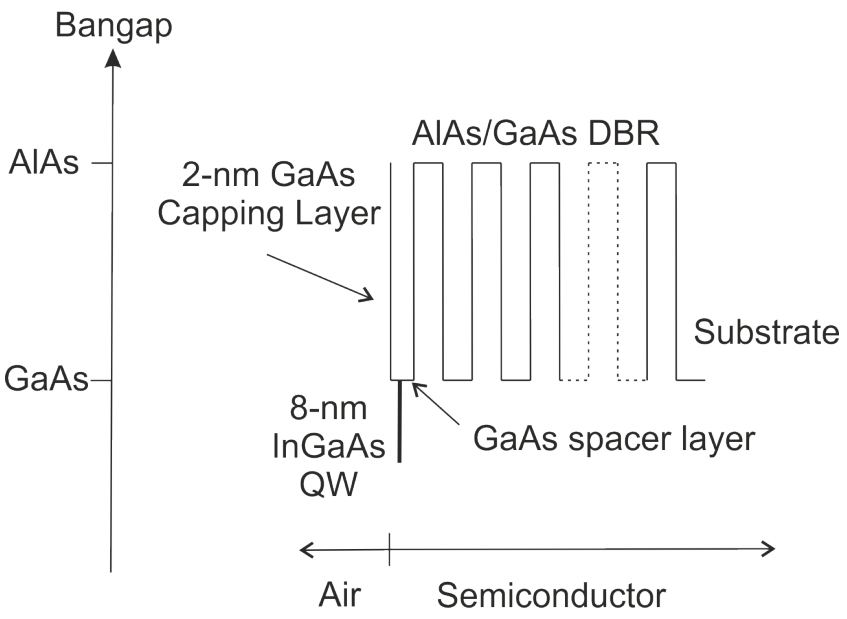

Figure 2.11: Schematic of a surface-recombination SESAM. A single 8-nm InGaAs QW is placed 2-nm from the surface of the structure. The electric field enhancement on the QW is controlled by the thickness of a GaAs spacer layer between the QW and the DBR. An AlAs/GaAs DBR then forms one of the cavity mirrors.

There are two methods predominantly used in current literature. The first is the use of low-temperature (LT) grown semiconductor structures pioneered by the Keller group at ETH Zürich (Paschotta and Keller (2001); Mangold et al. (2013)). These SESAMs have designs similar to that of gain structures; with a single QW placed at the anti-node of an electric field in a cavity and the use of a capping layer to control the enhancement. The reduction in the growth temperature causes an increase in the number of defects in the semiconductor material giving a rapid recombination channel for the carriers absorbed in the QW. However, absorption in the defects leads to a high insertion loss which is not ideal for high-power ML-VECSELs.

Garnache et al. (2002) introduced a new concept, the surface-recombination SESAM, with which they were able to demonstrate for the first time sub-500 fs pulses with 100-mw average output power from a ML-VECSEL. Placing a single QW 2 nm from the surface of the SESAM structure allows carrier tunnelling to surface defects providing a fast recombination channel without need for additional growth defects. The enhancement on the QW is adjusted by the thickness of the spacer layer shown in figure 2.11, and the

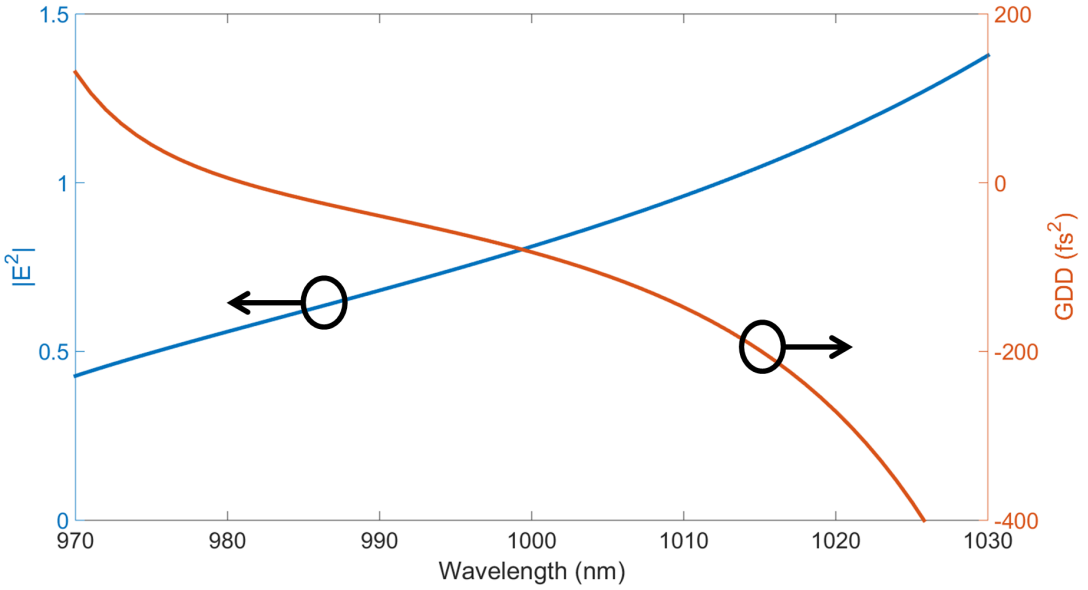

Figure 2.12: (a)E-field enhancement and (b) GDD profile as a function of wavelength for the surface-recombination SESAM shown in figure 2.11 designed to operate at 1000 nm.

resulting electric field enhancement for a spacer layer of 13 nm is shown in figure 2.12. To date the shortest pulses have been demonstrated using surface recombination SESAMs (Quarterman et al. (2009); Klopp et al. (2011)). All of the work performed in this thesis has been done with surface recombination SESAMs. I present in chapter 4 the first work done on characterising the macroscopic parameters and absorber response for the surface-recombination SESAMs described here with a 13.5-nm spacer layer.

As mentioned in the section on gain design, GDD is a key parameter for the formation of ultrashort pulses. GDD contributions from both gain and SESAM work together to form a net cavity dispersion profile that must be minimised and spectrally flat. Figure 2.12 shows the dispersion profile of a surface recombination SESAM, designed to match the dispersion from existing semiconductor anti-resonant gain structures. The slight positive dispersion from the gain at the design wavelength as shown in figure 2.8 is compensated by the slight negative dispersion from the SESAM, resulting in an net dispersion close to zero. Although both gain and SESAM exhibit similar dispersion profiles, the resulting net GDD profile only shows small variation around the design wavelength.

2.2 Thermal Management for High Average Powers

In the previous sections we have solely considered the design considerations to optimize gain and absorber structures for ultrashort pulse operation. In order to reach multi-Watt average output powers with ultrashort pulses it is necessary to consider the thermal management of VECSEL structures. In this section I shall describe my work on developing a wet-chemical substrate removal process as a route towards high-power ML-VECSELs. I shall discuss the rationale behind the choice of substrate removal process and the chemicals used and then present some results from processing structure grown by MBE at Cambridge University.

Efficient thermal management is important for the operation of virtually all lasers, with a limit to the achievable output power normally being set by heating in the gain medium. The technical considerations for thermal management of VECSEL gain structures differ somewhat to the challenges faced by diode-pumped solid-state lasers where the limit on power scaling is set by introduction of a thermal lens at high incident pump powers. VECSEL performance is limited by the local temperature induced carrier losses in the gain structure (Okhotnikov (2010)). As incident pump power is increased the heat load on the structure increases. In a CW-VECSEL increasing the pump power increases the output power until a point at which the temperature induced losses and reduction in gain causes the average output power to reduce; the point at which this occurs is termed thermal roll-over.

The difference in pump photon energy and emitted photon energy, the quantum defect, contributes to significant heating of the gain structure. Increased heating of the gain structure results in temperature effects induced in both the QW and the microcavity structure. The gain amplitude of the QWs is reduced with increasing temperature, dominated by Auger effects at high temperatures, increasing the laser threshold. The emission profile of the QW is also shifted to longer wavelength by ~ 0.3 nm/K. The heating of the microcavity structure introduces a change in refractive index resulting in a change of optical thickness which red-shifts the LCF profile at a rate of approximately 0.1 nm/K. In VECSEL gain structure designs the QWs are situated at the node of the

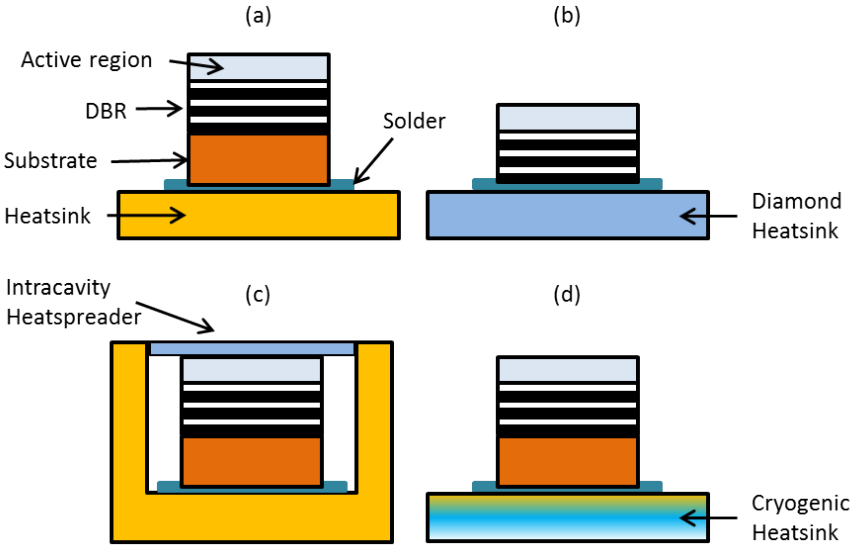

Figure 2.13: Schematic of thermal management techniques used to improve heat extraction from a VECSEL gain structure. (a) Standard VECSEL gain structure growth: no implementation of thermal management technique. (b) Substrate removal: Removal of thick substrate improves heat extraction from the rear surface of the structure. The addition of a high conductivity material, such as diamond, as the heatsink further improves the heat flow. (c) Intracavty heatspreader: contacting a high-conductivity material, such as diamond, to the front surface of the structure improves heat extraction directly from the active region of the gain structure. (d) Cryogenic heatsinks: the use of a heatsink kept at cryogenic temperatures increases the temperature gradient between active region and heatsink, resulting in increased heat flow from the structure.

electric field in the microcavity. The shift of the node away from the QW with increasing temperature reduces the light-matter interaction reducing the gain of the structure. Therefore, in order to minimize the increase of local temperature to stave off thermal-roll over to higher pump powers it is necessary to implement thermal management techniques to improve heat extraction.

Several methods for improving the thermal management of VECSELs exist, including use of intracavity heat-spreaders, substrate removal, and cryogenic cooling. Figure 2.13 shows a schematic of each.

Intracavity heat-spreaders offer an attractive method of thermal management for a broad range of wavelengths as the semiconductor composition does not affect heat extraction through the front surface (Lindberg et al. (2004); Schulz et al. (2008)). As we are interested in the performance increase of mode-locked VECSELs the use of intracavity

heat-spreaders is not an attractive method. The introduction of extra material affects the cavity GDD, and as discussed in previous sections is a critical parameter for ultrashort operation. The heat-spreader will act as an intracavity Fabry-Pérot etalon which applies a further filter to the gain profile reducing the gain bandwidth. The use of an intracavity etalon has, however, had interest for use in harmonic mode-locking regimes to access hundreds of GHz repetition rates (Saarinen et al. (2012); Wilcox et al. (2012)).

Cryogenic cooling is an attractive method to overcome the limit in heat extraction possible through conventional Peltier elements. Chernikov et al. (2011) were able to dissipate more than 300 W of waste heat using a heatsink directly connected to a liquid nitrogen bath and demonstrate a CW-VECSEL with 72 W average output power. In practice the use of cryogenic heatsinks results in damage to the gain structure through lattice dislocation due to the large differential thermal contraction. The technical design and growth considerations for overcoming the strain induced damage make using cryogenic heatsinks and unattractive for high-power ML-VECSELs (Morris (2014)).

Due to the binary semiconductor composition used for the construction of gain structures in the 1-μm wavelength regime wet-chemical removal of the substrate is the most effective method to access high powers. Recent advances in reliability of processing and structure design have allowed demonstration of multi-Watt mode-locked average output powers and above-100-Watt in CW around this wavelength. (Heinen et al. (2012); Wilcox et al. (2013); Scheller et al. (2012)). For longer wavelengths the semiconductor composition required for structure design has worse thermal conductivity, and as such substrate removal for thermal management does not give a significant performance increase (Maclean et al. (2009)).

As my work at Southampton has been focussed on the development of samples in the 1-μm wavelength range I have investigated substrate removal as a route towards Watt-level average output powers for sub 200-fs mode-locked VECSELs.

For substrate removal a "flip-chip" approach is used; the growth of the structure is reversed so that the window layer is grown on the substrate first and the DBR last, as shown in figure 2.14 (a). This growth allows the DBR to be soldered directly to a material with high thermal conductivity, such as diamond, before the substrate is

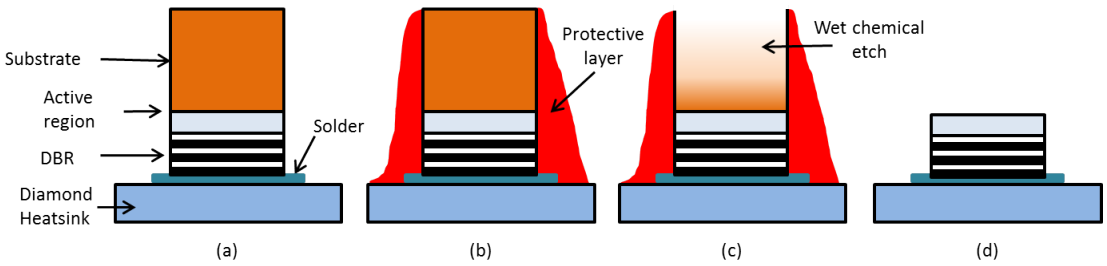

Figure 2.14: Schematic demonstrating the steps involved in a substrate removal process via wet-chemical etching. (a) Soldering of a "flip-chip" sample to a diamond heatsink. (b) Application of an etch-resistant protective layer to the sides of the gain structure to ensure a vertical etch profile. (c) The wet-chemical etch is performed to remove the substrate. (d) Protective layer is removed and the substrate removal is complete.

removed by wet chemical etching, figures 2.14 (b) and (c). The final etched surface must have good optical quality to reduce non-saturable losses and preserve homogeneity across the laser mode. In order to do this, etch-stop layers are included in the growth between the window layer and the substrate. Due to the selective nature, the ability to preferentially etch one semiconductor material over another, of the chemical etchant used these layers provide well defined stopping points for the etch. Whilst it is possible to use a single etch stop layer, in practice multiple alternating layers give greater control over finishing with good surface quality. Typical etch stop layers are based on AlAs due the lattice-matching with the substrate and etchant availability.

2.2.1 Procedure for Substrate Removal

At the start of my PhD, little work at Southampton had been done on the development of a method to reliably bond a "flip-chip" sample to a high thermal conductivity sub-mount and subsequent removal of the substrate. I will discuss the motivations behind each of the steps required and the subsequent choices made to implement substrate removal as a thermal management technique.

Forming a good thermal contact between the DBR and sub-mount is critical for efficient heat extraction from the gain structure. Diamond is the most common sub-mount materials due to its very high thermal conductivity, approximately 10 times that of copper. Due to the difficulty in bonding semiconductors directly to diamond it is necessary

to metallize both materials; Jin and Mavoori (1998) present a discussion of the methods required for using diamond for thermal management. Initially a thin film of carbide forming material was deposited on the diamond allowing a reliable metal-diamond bond. An inert metal was deposited next to protect the reactive surface and provide a layer for solder adhesion. The layers were deposited on both materials to form a strong bond. Due to material availability these metals were chosen to be Cr and Au. An eutectic $Au_{0.8}$ - $Sn_{0.2}$ solder was then used to bond the diamond to the semiconductor. The final soldering is performed with pressure applied under vacuum to remove any air voids that may cause inhomogeneity of the bond.

From the maturity of semiconductor wafer processing there is a wealth of literature on the chemical etchant and methods available for GaAs substrate removal (Baca and Ashby (2005)). Clawson (2001) presents a comprehensive list of the literature reporting on GaAs etchant covering etch rates and selectivity. The choice was narrowed by identifying the important requirements of fast etch rate and high selectivity. A fast etch rate is required to remove hundreds of microns of material in a reasonable time. Orders of magnitude difference between the etch rates of particular III-V semiconductor materials can be achieved using the appropriate etchant. In particular we are concerned with etches that can differentiate between AlAs and GaAs. For the etch to remove the substrate we require an etch that removes the GaAs material whilst not removing AlAs, allowing the etch to stop at the etch stop layer whilst also allowing sufficient time to remove any inhomogeneity in etch across the structure. To remove the etch stop layer, we require the opposite, an etch that stops at a GaAs surface but removes AlAs.

It is critical to protect the sides of the gain structure from exposure to the chemical etchant to stop any horizontal etching causing damage to the structure. In order to do this a protective layer must be applied to every surface not being etched, as shown in figure 2.14, which needs to be chemically inert and easily removed. For these reasons photoresist is used. Once baked it forms a chemically inert surface and can be easily dissolved in solvent based chemicals.

For removing the substrate a two stage etch was developed. The first stage removed the bulk of the substrate rapidly and the second stage provided fine control to reach the

etch stop layer. First step is a sulphuric acid etch composed of one part sulphuric acid, 8 parts H_2O_2 and 11 parts de-ionised water (1 H_2SO_4 : 8 H_2O_2 : 11 H_2O) from Barycka and Zubel (1987) with an etch rate of 3 μm/min and no selectivity of GaAs over AlAs. The second is a citric acid solution in the ratio 5 parts citric acid to 1 part H_2O_2 from Baca and Ashby (2005) who describe a GaAs etch rate of 18 μm/hour. This solution etches AlAs approximately 1000 times slower than GaAs allowing accurate stopping at the etch stop layers (Zhao et al. (1996)). To remove the AlAs etch stop layer a buffered hydroflouric (HF) solution is used due to its high selectivity of AlAs over GaAs. In order to remove multiple etch stop layers citric acid and HF etches are alternated until all etch stop layers are removed.

2.2.2 Substrate Removal of a "Flip-Chip" Gain Structure

The "flip-chip" gain structure designed for substrate removal was 7.5λ/2 semiconductor antiresonant designs with 27.5 layer-pair AlAs/GaAs DBR designed for operation at 1000 nm. A 300-nm AlAs etch-stop layer is grown between the GaAs capping layer and the substrate. The gain chip was grown at Cambridge University by MBE where the III-V growth facilities do not use phosphorous. Therefore, it was not possible to include GaP strain compensation layers in the growth design resulting in large quantities of defects due to lattice relaxation, known as dark-line defects. It is not possible to ascertain the quality of the growth of the gain structure until the sample is processed and as a result makes it impossible to predict device performance.

A simple straight-cavity laser was constructed with a 0.3% output coupler to test the performance of the the "flip-chip" structure processed by the method shown above. A 30-W 808-nm diode laser was used to pump a radius of 60 μm on the gain structure. The sample was mounted on a Peltier-controlled copper heatsink which was kept at 20 °C .

Figure 2.15 shows the output power as a function of pump power for both a processed "flip-chip" structure and an unprocessed structure of the same design. The laser using the processed gain chip had a threshold of 630 mW which is large compared to 300 mW required by unprocessed structures which indicates the presence of large scattering losses and a reduced quantum efficiency. The maximum output power achieved by the

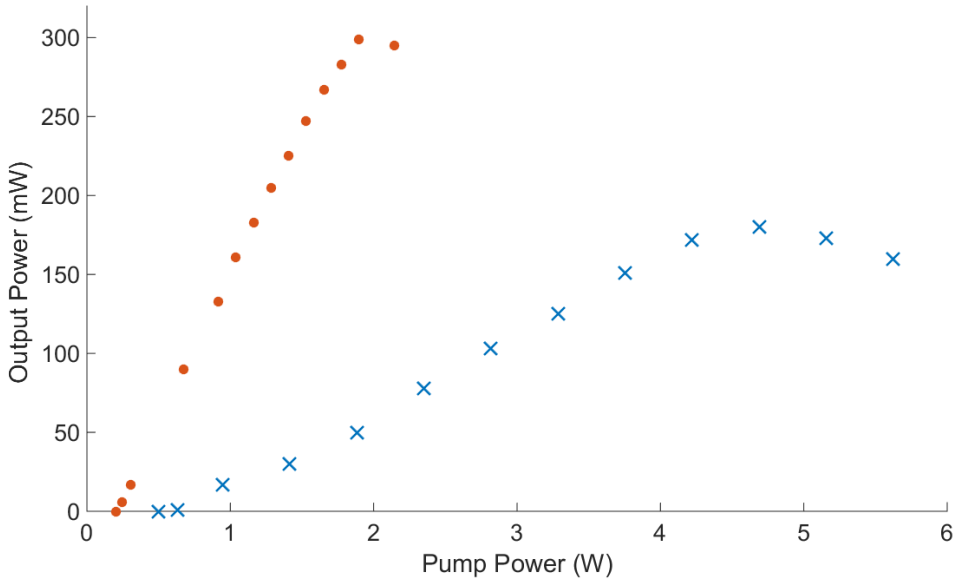

Figure 2.15: Measured output power for a processed "flip-chip" structure (blue crosses) and an unprocessed structure (orange dots) as a function of pump current. The output coupling was 0.3% and the pump radius was 60 μm.

structure was 180 mW at a pump power of 4.5 W. Rollover for unprocessed structures with the same pump area is less than 2 W indicating that the substrate removal and bonding to a high thermal conductivity heatsink has improved the heat removal from the gain structure. The power output of the structure was very low compared to 300 mW achieved using unprocessed structures of a similar design. This can be attributed to the high non-saturable losses indicated by the high laser threshold. Increasing the output coupling to 0.7% resulting in a decrease in the maximum power achieved to 45 mW for the processed structure.

Figure 2.16 shows the observed laser spectrum as a function of incident pump power. It shows that although the gain structure was designed for 1000-nm due to mis-growth it operated closer to 1020 nm. This could be due to either overall mis-growth of the structure or miscalibration of the QW. The mis-growth of the structure may also affect the overall laser performance resulting in the low output powers observed. There was large observed spot dependence on the structure and whether this was due to large numbers of defects in the structure or the substrate removal process is unknown.

Shortly after the growth of the initial "flip-chip" gain structure, the MBE machines

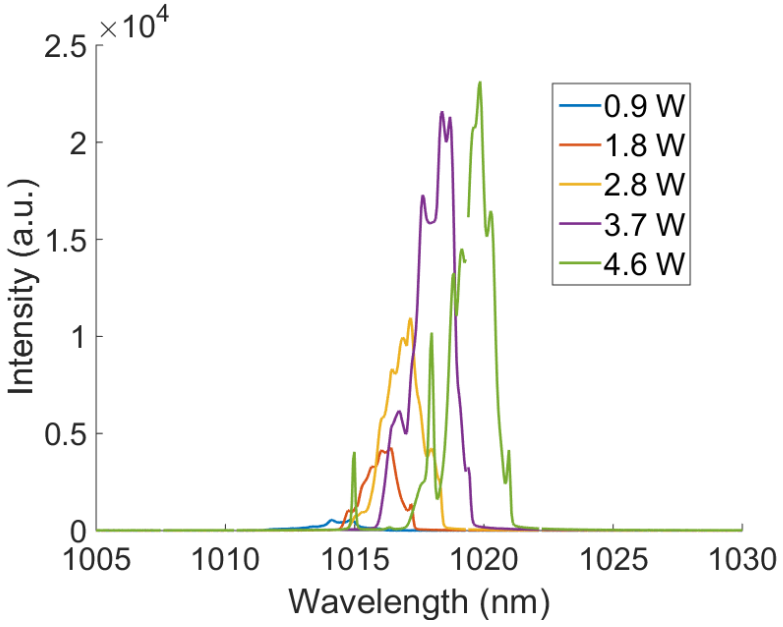

Figure 2.16: Measured laser spectrum for a processed "flip-chip" structure as a function of pump power.

Cambridge University experienced technical faults and were unavailable for regrowth of structures for a considerable period of time. As a result investigation into whether the device performance was limited by either mis-growth or processing was not possible. It was planned to grow both a normal growth and "flip-chip" structure from the same growth run to ascertain whether performance was limited by growth or processing.

Here at Southampton we do not have direct access to III-V semiconductor growth and therefore rely on collaborations to grow to the necessary VECSEL gain structures and SESAMs. With the lack of growth facilities there is also a lack of expertise and equipment used in wet chemical etching for III-V semiconductor processing. I developed the substrate removal and bonding process working with limited equipment and prior knowledge. Good quality growth and establish wafer processing techniques are critical for the pursuit of substrate removal as a route to high-power VECSEL operation.

A collaboration was formed with the Ulm University in Germany that have III-V MBE machines dedicated solely VECSEL growth which gives great improvements in terms of reliability of growth. They also have well established wafer processing facilities with equipment dedicated to bonding and substrate removal processes and a process that has

been refined over many years of wafer growth. They have provided gain structures used for high-power mode-locked operation described in chapter 6.

In spite of the high growth reliability afforded by having dedicated machines and refined processing the structures provided by Ulm University still exhibit spot dependent performance due to inhomogeneity in the surface of the gain structure. Theoretically power-scaling in high-power VECSELs is limited by the inability to extract heat from the centre of large pump spots. In practice, however, device performance is limited by the preservation of homogeneity across the laser mode. An area free of any defects is required, which practically is difficult to achieve as pump spots are made larger.

I have demonstrated the development of a substrate removal and bonding process at Southampton which has demonstrated improved heat extraction from the active region of a gain structure. However, device performance was greatly reduced due to defects arising either from misgrowth or the bonding and substrate removal procedure. In practice, as reliability of growth and processing is critical for device performance, processed structures from Ulm University will be used in pursuit of high-power ultrafast ML-VECSELs.

Chapter 3

Mechanisms of Pulse Formation in Mode-Locked VECSELs

In this chapter I present a discussion on the mechanisms of pulse formation in ML-VECSELs. I shall discuss a qualitative picture of the effects contributed from each cavity element linked to the macroscopic structure parameters discussed in chapter 2.

The process by which ultrashort pulses form in SESAM-mode-locked lasers, described here, can be qualitatively understood and quantitatively modelled based on the insights presented by Siegman (1986) and Haus (2000). A passive cavity element acts to form pulses by the introducing an intensity dependent loss or gain into the laser cavity. As the intensity is increased the loss (gain) is decreased (increased) making it energetically more favourable for a high intensity pulse to propagate in the cavity. In this thesis I will solely be considering the use of a SESAM to passively mode-locked a VECSEL.

VECSELs present a unique model of pulse formation with their relaxation-free class-A laser dynamics, weak pulse shaping interactions and dynamic gain saturation. Many parameters that influence structure and laser design choices that are specific to ML-VECSELs have great influence on the mode-locked performance achievable. The dependence of the gain profile on both carrier density and local temperature effects the laser wavelength and gain bandwidth. The gain and absorber both cause a non-linear phase change in the laser spectrum, however, the magnitude and shape of the effect

are unknown (Paschotta et al. (2002)). The large gain cross-section and corresponding small gain saturation energy lead to gain saturation effects influencing the formation of a pulse. Carrier life-times on the order of a nanosecond give natural operation at GHz repetition rates.

The class-A laser dynamics in VECSELs arise from the high-Q cavity, giving long photon life-times, combined with the short upper-state carrier lifetime. This relatively unique combination in VECSELs results in a very low noise laser source and acts as a low-pass filter effect on spontaneous emission noise (Mvara et al. (2013)). Whilst conventional DPSSLs have photon lifetimes of a similar order of magnitude to those in VECSELs, the upper-state gain lifetime is many orders of magnitude longer (∼ms), allowing the gain to respond to variations in the photon number in the cavity. The resulting complex interplay of gain and cavity dynamic leads to class-B operation which results in large amounts of spontaneous noise. As DPSSLs are scaled to high-repetition rates, and consequently the intracavity pulse energy is decreased, absorber design becomes critical for the suppression of Q-switching instabilities. The class-A laser dynamics coupled with the large semiconductor gain cross-section in ML-VECSELs results in removal of Q-switching instabilities at multi-GHz repetition rates allowing stable mode-locking with very low noise.

3.1 Time and Frequency-Domain Description

We can consider the theory of mode-locking in two different domains: time and frequency. Svelto (2010) gives a full treatment of both. When the laser is first pumped, all the longitudinal modes of the external cavity for which the unsaturated gain exceeds the cavity loss will oscillate with random, unrelated phases at a frequency given by:

$$\omega_m = 2\pi\nu_m = m\frac{\pi C}{L}, \tag{3.1}$$

where m is an integer cavity mode number, C is the vacuum speed of light and L is the optical length of the cavity. The total electromagnetic field in the cavity at any point can be written as a sum of the oscillating laser modes giving the relationship:

$$E(t) = \sum_{m} A(\omega_m) exp(i(\omega_m t + \phi)), \tag{3.2}$$

where $A(\omega_m)$ is the amplitude of each cavity mode defined by the gain spectrum profile and ϕ is the phase of each cavity mode. Figure 3.1 shows a simulated time-varying E-field calculated from equation 3.2 for a laser with gaussian spectral profile with a FWHM width of 0.1 nm and a cavity mode spacing of 1 GHz. Although the spectral bandwidth is small compared to those of typical ML-VECSELs, it is sufficient to provide illustration of the theory being described. Here we can consider two cases. The first is where ϕ is random for each cavity mode and as such there is no phase relation, shown in figure 3.1 (a). The second is where there is a defined phase relationship such that:

$$\phi_m - \phi_{m-1} = \phi, \tag{3.3}$$

shown in figure 3.1 (b). The first condition leads us to pure CW laser operation. When looking at the resulting electromagnetic field output of the laser at time-scales on the order of the cavity round-trip time it can be seen to be composed of a train of random noise spikes. The temporal width, τ, of these spikes is approximately $1/\Delta\nu$, where $\Delta\nu$ is the bandwidth of the laser spectrum. As a result of the random phase, the energy in the cavity is spread out over all noise spikes with no fixed relation resulting in low peak powers.

In the second condition we have each of the longitudinal modes oscillating with a fixed phase which alters the output from a train of noise spikes to a defined series of pulses with a fixed repetition rate. It can be shown that the temporal width of the pulses has the same relationship as in the case of no fixed phase relation ($\tau \sim 1/\Delta\nu$) and successive pulses have a well defined temporal separation given by:

$$\tau_{rep} = \frac{1}{\Delta f}, \tag{3.4}$$

where Δf is the cavity mode spacing (Svelto (2010)). Although the temporal width of the pulses is the same for both cases, the intracavity energy of the mode-locked laser is contained in a single pulse, and as a result the peak power observed in this case is approximately 20 times the peak power with no fixed phase relations. As the spectral bandwidth increases, the pulse duration decreases, further increasing the peak power observed.

If all cavity modes are in phase the resulting pulse is termed to be transform limited and yields the minimum possible time-bandwidth product, which is defined as the product of the FWHM spectral bandwidth in frequency and FWHM pulse duration. The time-bandwidth product for a pulse will yield a value that describes how many times transform limited the pulse giving a measure of how much of the spectrum is contributing the formed pulse. The time-bandwidth product for a transform-limited gaussian pulse is 0.441 and for a pulse with a hyperbolic-secant profile it is 0.315.

We can also consider the onset of mode-locking where the spectrum evolves from the condition in the frequency domain with no fixed phase relation until the final steady-state pulse solution. We begin with an initial train of noise spikes in the cavity and an element with non-linear loss. A noise spike with enough energy will be able to partially saturate the non-linear loss allowing it to be amplified preferentially by the gain. Over the course of subsequent round trips this initial noise spike is shaped by interactions between gain and non-linear loss, eventually balancing to form a steady-state output pulse train. Overall the final steady-state pulse solution relies on balancing not only the dispersive effects in the cavity, as required in a quasi-soliton solution (Keller and Tropper (2006)), but also the balance of gain and loss, and pulse stretching and shortening effects leading to the forming of a dissipative soliton (Grelu and Akhmediev (2012)).

For passively mode-locked VECSELs we can assume that the pulse shaping effects are weak over the course of a single round trip and therefore it is possible to separate out the contribution from each effect. The final solution from the linear addition of pulse

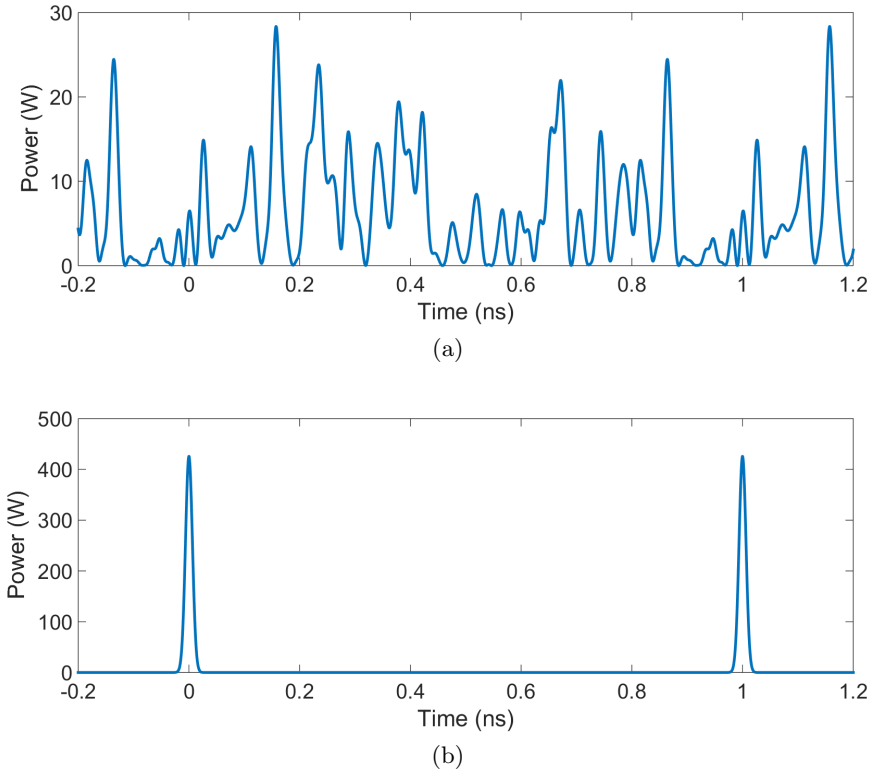

Figure 3.1: Simulated intracavity power as a function of time for a laser with cavity modes which have (a) random phase and (b) constant phase calculated from equation 3.2. The model uses a gaussian spectral profile with a FWHM bandwidth of 0.1 nm and a cavity mode separation of 1 GHz.

shaping effects in a slow saturable absorber regime is given by the master equation developed by Haus (2000). The final solution to the steady-state pulse takes the form of:

$$I(t) = I_0 \, sech^2 \left(t/\tau \right), \tag{3.5}$$

providing the conditions of dynamic gain saturation, discussed in the next section, are met. To understand the qualitative effect of each pulse-shaping interaction they will be considered individually in sections 3.2.1 - 3.2.3.

3.2 Dynamic Gain Saturation

Passive mode-locking can be explained by a range of models including fast saturable absorber mode-locking, slow saturable absorber mode-locking without dynamic gain saturation, and slow saturable absorber mode-locking with dynamic gain saturation as shown in figure 1.1. Due to the high gain cross section in semiconductors the gain experiences a fast pulse induced saturation which recovers between consecutive pulses. As stated in chapter 2, the passive mode-locking work at Southampton has used SESAMs. These are classed as slow saturable absorbers as they have recovery times much longer than the formed pulse. We require saturation of both absorber and gain to open up a short window of net-gain for the pulse. To achieve this the absorber must saturate much faster than the gain leading to the following inequality based on saturation energies:

$$\frac{E_{sat}^{abs}}{E_{sat}^{gain}} = \frac{F_{sat}^{abs} \cdot A_{abs}}{F_{sat}^{gain} \cdot A_{gain}} \ll 1, \tag{3.6}$$

where $F_{sat}^{abs(gain)}$ are the saturation fluences and $A_{abs(gain)}$ are the laser mode areas of the absorber and (gain) respectively. As mentioned in chapter 2 gain and absorber structures are based on similar materials and, as such, have saturation fluences with a similar order of magnitude. Consequently it is necessary to have a large area ratio between the gain and absorber to satisfy the above inequality. A tight focus on the absorber will limit high average powers due to temperature induced loss and potential optical damage. Reducing the absorber saturation fluence and increasing the gain saturation fluence by structure engineering allows operation closer to a 1:1 area ratio which is necessary to reduce cavity design constraints and operate at high average powers. As we must satisfy the inequality in equation 3.6, the cavity design is critically linked to absorber and gain fluences, therefore, characterisation of these parameters is important.

In the next sections we consider the effects of the gain, absorber, and linear and nonlinear phase shifts on the pulse formation and how structure design and parameters will affect the final steady-state pulse duration.

3.2.1 Gain: Amplification and Pulse Stretching

The gain structure serves to amplify the pulse whilst also applying a spectral filter that lengthens its temporal profile.

In the frequency domain the application of a spectral filter amplifies the components at the centre of the spectrum more than the in the wings reducing the spectral width and hence increasing the pulse duration. In the time-domain the leading edge of the pulse is amplified more due to the unsaturated gain, as the pulse propagates in time the gain is saturated resulting in less amplification of the trailing edge. At sufficiently large pulse energies over-saturating the gain makes energetically favourable to support multiple pulses in the cavity. To maximise the pulse energy that the laser can support we require a large gain saturation energy.

As has been verified experimentally by Borgentun et al. (2011) and Mangold et al. (2012) structure design effects the profile of the gain. Small changes in the small signal gain across the profile will have a large effect on the resulting laser output. The spectral filter is dependent on the curvature of the gain profile, therefore a broad, flat gain profile is desirable to minimise the pulse lengthening caused by the gain whilst also amplifying the spectral components equally. The theory described here agrees with the design considerations for a structure optimised for broad gain bandwidth and high gain saturation energy put forward for gain structures in chapter 2.

The gain structure also introduces linear and non-linear phase shifts to the pulse spectrum which will be covered alongside the contributions from the absorber in section 3.2.3.

3.2.2 Absorber: Loss and Pulse Shortening

The SESAM has the effect of shortening the pulse per round trip. At the on-set of mode-locking we require the pulse shortening from the absorber to be greater than the lengthening by the gain. In the steady-state, the contributions from both are balanced. In order to reach ultra-short pulse durations it follows that the pulse shortening from the absorber should be maximised.

For an ideally fast absorber, as shown in figure 1.1 (a), recombination times are on time-scales shorter than the pulse duration. The passage of the pulse through the absorber leads to a loss that follows the profile of the pulse, opening a window of net gain. Both wings of the pulse see more loss than the centre which reduces the temporal pulse width symmetrically. As previously mentioned SESAMs have been characterised to have long time-scale responses and therefore we do not typically consider the fast absorber model. However, it has been suggested that there is some intensity dependent fast absorber effect, or AC Stark effect, that may provide a pulse shortening mechanism at high peak intensities (Garnache et al. (2002); Wilcox et al. (2008)). Although it has not been experimentally verified as a pulse shaping mechanism, it is important to consider all effects when understanding pulse formation.

SESAMs operate with recombination times that are long on the time-scale of the pulse and are therefore considered slow absorbers. In the time domain the leading edge of the pulse is absorbed by the QW in the SESAM promoting carriers from the valance band into the conduction band. Once the carrier density is evenly distributed between the conduction band and valence band the absorber is said to be “bleached” and the remainder of the pulse propagates unchanged. The carriers then recombine non-radiatively between successive pulses. The absorption of the leading edge serves to narrow the pulse. The asymmetrical temporal shortening of the pulse is balanced by asymmetrical lengthening by the gain.

When viewed in the frequency domain, the amplitude modulation of the pulse by the absorber generates in-phase side-bands at multiples of the cavity repetition rate either

side of the central frequency. The creation of extra in-phase spectral components serves to shorten the pulse.

It is important to understand how the absorber responds based on incident pulse fluence to understand the effect cavity design has on the limits of high-power ultra-fast laser performance. Initially we can define the saturation parameter of the absorber as:

$$S = \frac{F_{pulse}}{F_{sat}}, \tag{3.7}$$

where F_{pulse} is the incident pulse fluence on the SESAM and F_{sat} is the saturation fluence, defined previously. By combining S with the response of a slow absorber that does not recombine on the time-scale of the incident pulse we can analyse the absorption, and subsequently the pulse shortening, as a function of the saturation parameter. Kärtner et al. (1996) showed that the absorption over the pulse is given by:

$$q(t) = q_0 \; exp\left(\frac{S}{2}\left[1 + tanh\left(\frac{t}{\tau}\right)\right]\right), \tag{3.8}$$

where q_0 is the modulation depth of the absorber, τ is the pulse width, and t is the time where the pulse is centred at $t = 0$. Figure 3.2 shows the modelled pulse shortening of a single pass of a pulse through a slow absorber as a function of saturation parameter for a fixed pulse duration and modulation depth. Here pulse shortening is defined as the difference between the FWHM pulse duration before and after a single pass through the absorber. The inserts in figure 3.2 show the pulse envelope (blue line) and the modelled absorber reflectivity (orange line) for saturation parameters of (a) 1, (b) 6, and (c) 40. At small values of S the pulse energy is not sufficient to saturate the absorber fully and as a result there is a net absorption across the whole pulse, as shown in (a). As S is increased there is greater saturation of the absorber leading to an increase in pulse shortening until a value of S at which maximum shortening occurs is reached, (b). For values of the saturation parameter greater than that at which the maximum shortening occurs there is a reduction in the pulse shortening by the absorber. At higher pulse energies corresponding to increasing values of S, the leading edge of the pulse is

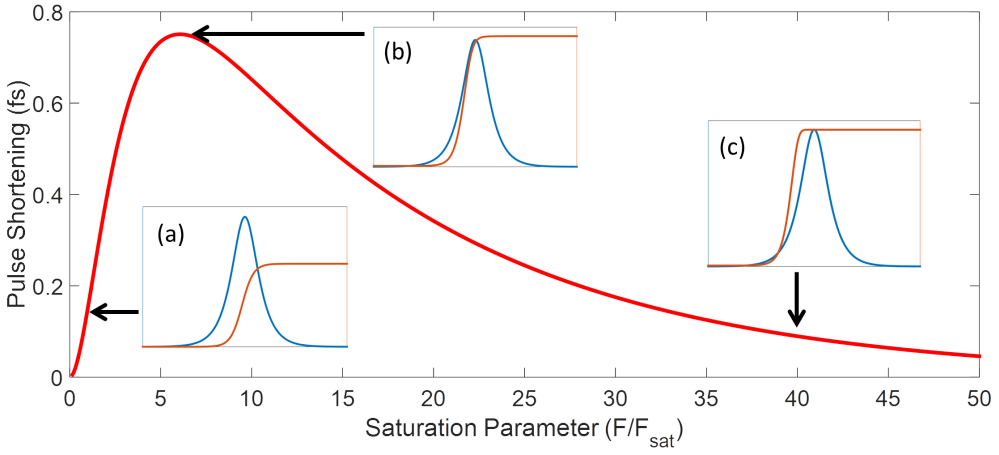

Figure 3.2: Simulated pulse shortening for a single pass through a slow saturable absorber as a function of the saturation parameter, S. The modelled absorber has a modulation depth of 1%, saturation fluence of 10 $\mu J/cm^2$ and a response based on equation 3.8. The incident pulse had sech^2 pulse profile with a FWHM duration of 400 fs. Pulse shortening is defined as the difference between the FWHM pulse duration before and after passage through the absorber. The inserts show the initial pulse envelope (blue line) and the modelled absorber reflectivity (orange line) as a function of time for a saturation parameter of (a) 1, (b) 6, and (c) 40.

able to saturate the absorber. At sufficiently high pulse energies, (c), the effect of the absorber on the pulse is small as the initial wing of the pulse contains sufficient energy to fully saturate the absorber. Literature on mode-locked VECSELs contains reports of saturation parameters ranging from 5 to 30 (Hoffmann et al. (2010); Wilcox et al. (2008)).

For ultrafast operation, critically, the pulse shortening by the absorber must be maximised which can be achieved by altering S and the modulation depth either by structure or cavity design. The pulse shortening can be increased by increasing the modulation depth, however, there are strict limits as the total loss must be lower than the small signal gain to reach laser threshold. Additionally, in pursuit of high average powers, the increasing of the modulation depth will reduce the achievable output power.

As shown in equation 3.7, S is dependent on F_{sat} and the pulse fluence. As we are concerned with the pursuit of high-power ultrafast ML-VECELs we must consider how S scales as we move towards higher pulse energies. As S increases with the pulse fluence, at first glance it may seem sensible to increase F_{sat} to keep the value of S small to maximise

pulse shortening. However, as F_{sat} is also constrained by the inequality in equation 3.6 we must then also decrease the area on the SESAM to satisfy the requirements for dynamic gain saturation. Increasing the pulse energy and decreasing the SESAM mode-area would be likely to induce optical damage in the absorber which is not desirable. As a result it seems that the dynamic gain saturation inequality drives the consideration of minimising F_{sat} for stable ultrafast operation. To support higher pulse energies without increasing S it would therefore be necessary to increase the mode-area on the SESAM to reduce the incident pulse fluence. Increasing the mode-area would be possible through maximising the value of gain saturation energy which would further reduce the mode-area constraints on the absorber. In order to still have maximum shortening at high pulse energies it is therefore critical to not only minimise the absorber saturation fluence but also maximise the gain saturation fluence.

The benchmarks for high-average-power SESAM mode-locked VECSELs demonstrated by Scheller et al. (2012) and Wilcox et al. (2013) have been limited to greater than 400-fs pulse duration. In order to reduce pulse durations at such high intracavity powers careful design and characterisation of both gain and absorber optimised for high-power performance is critical.

3.2.3 Linear and Non-Linear Phase Shifts

As stated in section 3.1 the formation of a dissipative soliton is based not just on the gain and loss interactions but also on the balancing of linear and non-linear phase changes introduced by cavity elements. Phase shifts affecting the longitudinal cavity modes in mode-locked VECSELs can be divided into effects arising from the non-linear phase change due to gain and absorber saturation and from the linear phase change associated with GDD. The relation between non-linear phase change and gain or loss is linked by the phenomenological line-width enhancement factor (LEF), α (Agrawal and Bowden (1993)):

$$\Delta\phi_{gain}(t) = -\alpha_g\, g(t)/2 \;\text{ and }\; \Delta\phi_{abs}(t) = -\alpha_{abs}\, q(t)/2, \tag{3.9}$$

where $g(t)$ is the structure gain and $q(t)$ is the absorber loss and $\Delta\phi(t)$ is the non-linear phase change of gain and SESAM respectively.

The model developed by Paschotta et al. (2002) indicates that we can draw parallels between dispersion requirements in SESAM mode-locked VECSELs and those in well-established Kerr mode-locked solid-state lasers where negative GDD is required to offset the introduction of a positive non-linear phase shift from a non-linear Kerr medium. If the non-linear phase shift in ML-VECSELs is negative, then it follows that positive GDD must be included. The requirement of positive GDD from the combination of gain and absorber puts restrictions on our structure design as discussed in chapter 2, where the combined dispersion profile must be invariant, small, and positive over the whole gain bandwidth.

Hoffmann et al. (2010) presented an experimental verification of the requirement for the combined structure GDD to be positive and minimised. The results demonstrated show significant pulse lengthening for negative GDD and large values of positive GDD. The shortest pulses were observed when a positive GDD between 2000 and 6000 fs^2 was introduced into the laser cavity. The shortest pulse duration of the laser was measured to be 1.5 ps with a 0.86-nm FWHM spectral width. An intracavity etalon was used to tune the output wavelength, however, it was not included in the net cavity GDD calculations. Although the measurements support the quasi-soliton model, due to the relatively long pulse durations and the use of an intracavity etalon the conclusions of the experiment may not apply as pulse duration move towards 100-fs.

The effect of linear dispersion in the frequency domain purely serves to change the relative phases of the cavity modes with respect to the central mode. As previously discussed, we require all modes to be in phase to form the shortest pulse from the available steady-state laser spectrum. In the time domain, the effect of introducing out-of-phase components contributes to energy being spread temporally from the pulse centre and subsequently attenuated due to absorber interaction, with the overall effect of narrowing the spectrum. By compensating with the correct sign and magnitude of GDD the out of phase components can be temporally shifted to contribute to the pulse maximum. From arguments presented by Svelto (2010) dispersion becomes an increasingly

important factor as the pulse durations approach 100-fs because the relative phase shift between short-wavelength and long-wavelength cavity modes becomes a greater effect over a broader laser bandwidth. Therefore it is necessary to ensure that the change in overall cavity dispersion around the design wavelength is minimised and invariant.

Gosteva et al. (2005) presented an analysis of the accuracy achievable by white light interferometers used to measure GDD of optical components, and showed that the overall accuracy of such measurements is limited to approximately ± 100 fs^2. For structure designs optimized for small and invariant GDD it will therefore not be possible to accurately determine GDD values experimentally. As a result, modelling of structure GDD using multilayer calculations provides the best method to determine dispersion as a function of wavelength for both gain and SESAMs. However, it relies on high-quality semiconductor growth to ensure minimal deviation from the expected structure designs and calculated parameters.

3.3 Predictive Pulse Formation Modelling in Mode-Locked VECSELs

A number of authors have described numerical simulations of pulse formation in mode-locked VECSELs to match macroscopic experimental parameters to observed laser outputs. Here I give a brief overview of the work that has been performed in the field of modelling pulse formation in passively mode-locked VECSELs to give an insight into the limitations that still exist and as a motivation to my work experimentally resolving the formation of pulses in chapter 5.

Initial modelling of soliton-like dynamics by Paschotta et al. (2002) explained the early results from passively mode-locked VECSELs which were confirmed experimentally by Hoffmann et al. (2010). The requirement of accurately determining the structure parameters detailed in chapter 2 limited the ability to fully model the pulse formation in mode-locked VECSELs until characterisation techniques developed by ETH Zürich (Haiml et al. (2004); Mangold et al. (2012)) led to accurate experimental parameter

extraction. Subsequently, Sieber et al. (2013) presented an investigation into the quantitative effect of laser parameters on the output pulse duration and average power, based on the model developed in Paschotta et al. (2002) and Paschotta (2004). The results agree with experimentally measured laser performance and validates the model as a useful tool for providing guidelines to improve gain and SESAM structure designs for high-power femtosecond operation. At Southampton, the lack of structure characterisation has prevented the use of such a model to investigate pulse formation in our lasers and motivates the work presented in chapter 4.

Whilst the work presented by Sieber et al. (2013) forms a comprehensive picture of the effect of structure design on pulse formation, there are other structure parameters that have not been experimentally determined leading to assumptions about their magnitude and effect. Two critical parameters are the upper-state gain lifetime and the magnitude of the LEF mentioned in equation 3.9.

Upper-state lifetimes in semiconductor lasers are known to be of the order of ns, however, such short time-scales are difficult to experimentally determine. As a result, this affects the modelling of the recovery time of the gain and the lower limit of cavity repetition rate in single pulse operation.

The LEF is known to be both wavelength and carrier-density dependent (Paschotta et al. (2002)) and change over the course of the pulse interaction with the semiconductor material (Agrawal and Bowden (1993)), However, in the above models it is treated as constant for both gain and absorber. The values are difficult to determine under experimental conditions and therefore the magnitude and the profile of the non-linear phase change is unknown. Sieber et al. (2013) cited the line-width enhancement as being uncritical for the solution of their model, despite the steady-state pulse solution showing strong dependence on both gain and absorber LEF in certain ranges. The assumption of requiring small positive GDD is also based on non-linear phase change from the LEF despite not knowing the overall magnitude and shape of the effect.

As the gain structure is typically situated in the middle of the cavity there are two gain-pulse interactions per round trip included in the models used above, however, the work on probing in-situ response of the gain under operating conditions by Scheller et al. (2015)

Structure Parameters	Gain	SESAM	Cavity Parameters	Values
Saturation Fluence F_{sat} ($\mu J/cm^2$)	100	10	Repetition Rate f_{rep} (GHz)	2.0
Fast SESAM Recovery Time τ_{fast} (fs)	-	460	Output Coupling (%)	1.0
Slow SESAM Recovery Time τ_{slow} (ps)	-	15.6	Net Cavity GDD (fs^2)	50
SESAM Modulation Depth ΔR	-	2	Gain Mode Radius r_g (μm)	200
Small Signal Gain g_{ss} (%)	8	-	SESAM Mode Radius r_{abs} (μm)	200
Gain Bandwidth Ω_g (nm)	30	-		

Modelled Laser Output	
Average Output Power (W)	1.08
Pulse Duration (fs)	193
FWHM Spectral Width (nm)	5.88
Peak Output Power (kW)	2.38

Table 3.1: Macroscopic structure and cavity parameters used by Sieber et al. (2013) in modelling a Watt-level sub-200-fs ML-VECSEL.

has highlighted the difference in gain response due to differing carrier concentrations and finite gain-recovery times. The change in carrier concentrations will result in the pulse seeing different gain and phase change for each interaction per round trip.

In the above quasi-soliton models the absorber profile is treated as spectrally invariant, despite the absorber having a finite bandwidth of a QW. The effect of the unsaturated absorber profile will have an unknown effect on pulse formation and pulse stability in a SESAM mode-locked VECSEL. Any thermal effects arising from the SESAM are also not included in the models.

In spite of the assumptions made by the model presented by Sieber et al. (2013), the simulated device characteristics required for construction of a Watt-level 200-fs VECSEL serve as the best benchmark for required macroscopic structure parameters. The model output parameters for a Watt-level ML-VECSEL with a sub-200 fs pulse duration at a repetition rate of 2 GHz are shown in table 3.1.

Predictive modelling of 100-fs pulses using microscopic many-body simulations has also been performed by (Hader et al. (2011); Moloney et al. (2014)), where Maxwell - semiconductor Bloch equations are used to investigate the role of hot carriers on pulse formation. The models are based on the assumption of idealised semiconductor structures and rely solely on the microscopic carrier interactions rather than macroscopic experimental parameters. The models are heavily computer intensive and, due to the assumption, do not lend themselves to predicting real world laser behaviour.

The above assumptions make experimental verification of the predictive pulse formation models important. At Southampton, much experimental work has been done on spectrally resolving the onset of lasing in CW-VECSELs and extracting laser parameters under operating conditions (Barnes et al. (2010); Head et al. (2014)). In chapter 5, I apply these techniques to experimentally investigate pulse formation in a mode-locked VECSEL.

Chapter 4

Characterisation of Surface-Recombination SESAMs

In November 2013 I spent a week working in the Keller group at ETH-Zürich, using the facilities of the group to make linear and non-linear reflectivity measurements and time-resolved pump-probe measurements on a selection of surface-recombination SESAM structures used in this thesis.

The research group at ETH-Zürich have driven the development and improvement of characterisation techniques for VECSEL gain and absorber structures and, as a result, have a great amount of expertise in the measurement of macroscopic structure parameters. There is a requirement for sensitive characterisation techniques due to the low gain and loss nature of the laser structures .

In 2012, Mangold et al. built on the initial work by Borgentun et al. (2011) to provide a full suite of techniques for the characterisation of VECSEL gain structures to determine small-signal gain (g_0), gain saturation fluence (F_{sat}^{gain}) and gain bandwidth (Ω_g).

The SESAM parameters that we are interested in for laser design are: modulation depth (ΔR), the saturation fluence (F_{sat}^{abs}). and absorber response time constants (τ_{slow} and τ_{fast}). Haiml et al. (2004) was the first to characterise the non-linear reflectivity of an absorber structure to extract F_{sat}^{abs} and ΔR along with the non-saturable losses. Maas et al. (2008) then simplified the experimental setup whilst maintaining the required level

of accuracy As ΔR is of the order of a percent. The experimental techniques used by Haiml et al. (2004) and Maas et al. (2008) achieved a measurement error of <0.05% over 4 orders of magnitude of pulse fluence. Characterising the absorber response time is performed using a standard reflection pump-probe setup. By combining non-linear reflectivity and pump-probe measurements Fleischhaker et al. (2013) have shown a combined experimental technique to extract all of the desired absorber parameters.

Characterisation of surface-recombination SESAMs has been demonstrated by Zorn et al. (2008), where the electric field enhancement on the QW was set by the thickness of a dielectric coating. Structures used in this thesis do not use a dielectric coating, instead, the electric field enhancement is set solely by the thickness of the GaAs spacer layer.

An initial characterisation by R. Grange in 2005 was performed on a "low modulation depth" surface-recombination absorber structure, QT1627. The SESAM was designed with a 40-nm GaAs spacer layer separating a single InGaAs QW from an AlAs/GaAs DBR and a 2-nm GaAs layer capped the structure. The measurement was performed using a mode-locked Yb:YAG laser with a pulse duration of 2.1 ps and a fixed 1030-nm central wavelength. The characterisation of the "low modulation depth" absorber design yielded a ΔR of 0.3 $\pm$ 0.04% and a F_{sat} of 56 $\pm$ 3 $\mu J/cm^2$ as shown by the measured non-linear reflectivity as a function of fluence in figure 4.1. This absorber was used to generate sub-500-fs near transform limited pulses with 40-mW average output power (Wilcox (2006)).

Decreasing the thickness of the spacer layer increases the electric field enhancement on the QW and hence increases the modulation depth and reduces the saturation fluence. A new design of surface-recombination SESAM reduced the spacer layer thickness from 40-nm to 13.5-nm. The electric field enhancement on the QW as a function of wavelength for both designs is shown in figure 4.2. At 1030 nm, where the absorber is designed to operate, there is an increase in enhancement from 0.1 to 0.25 as the spacer layer thickness is decreased from 40 nm to 13.5 nm. Wilcox et al. (2008) described a calculated modulation depth of 0.7% for a 13.5-nm spacer layer SESAM, however, the value of saturation fluence was not reported. The calculated value was obtained by equating the

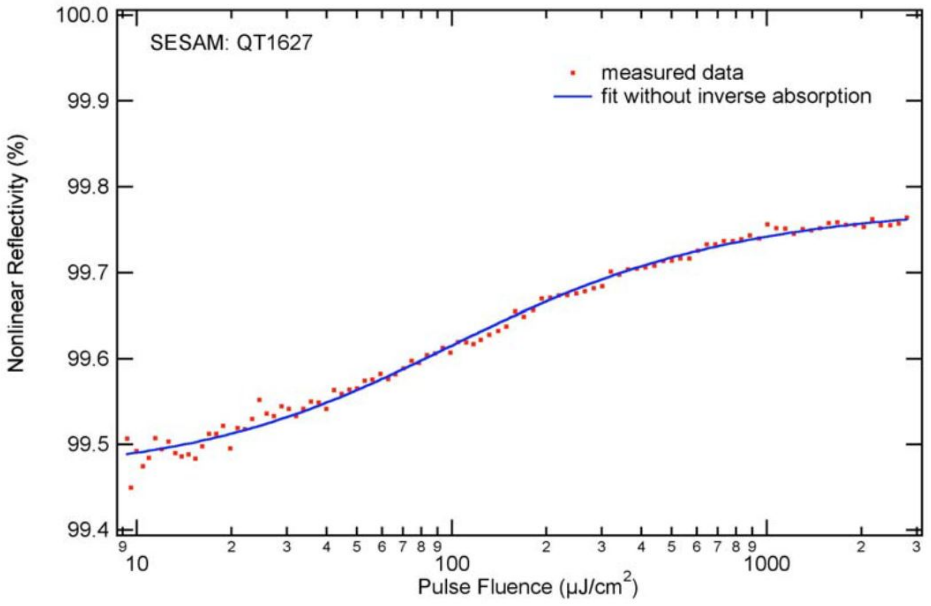

Figure 4.1: Non-linear reflectivity characterisation of QT1627, a surface-recombination SESAM with a 40-nm spacer layer thickness. The extracted F_{sat} was 56 ± 3 μJ/cm^2, ΔR was 0.3 ± 0.04%, and ΔR_{ns} = 0.22 ± 0.04%. The characterisation was performed by R. Grange at ETH-Zürich.

ratio of the modulation depths of the two absorber designs to the squared modulus of the electric field enhancement:

$$\frac{\Delta R_{13.5\,nm}}{\Delta R_{40\,nm}} = \frac{|E_{13.5\,nm}|^2}{|E_{40\,nm}|^2} \tag{4.1}$$

The work presented in this chapter represents the first experimental characterisation of SESAMs with a spacer layer thickness of 13.5 nm.

I completed the measurements with the aid of the Keller group during a visit to ETH-Zürich in November 2013. The design parameters of the characterised structures are outlined in table 4.1. The characterisation techniques performed were: low-power broadband reflectivity measurements (section 4.2), non-linear reflectivity measurements (section 4.3), and pump-probe measurements (section 4.4).

The characterisation was limited to structures designed for 1030 nm due to the availability of laser sources. As a result it was not possible to extract structure parameters

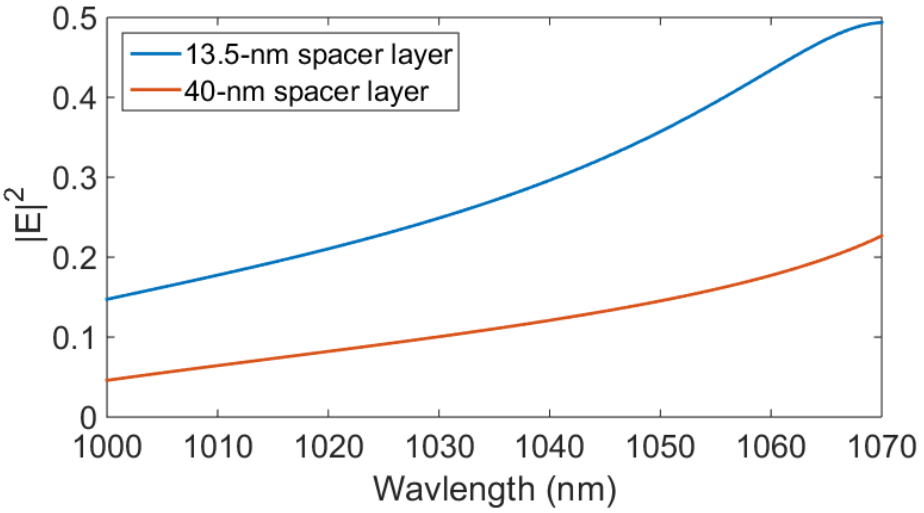

Figure 4.2: Simulated modulus of the electric field squared on the QW in a surface-recombination SESAM as a function of wavelength for an absorber with a 13.5-nm (blue) and 40-nm (orange) thick spacer layer. Normalised to an electric field of 1 in air.

for existing structures designed for operation at 1000-nm, however, due to the similarity in layer design it is likely that the values will be of the same order of magnitude.

From the non-linear reflectivity measurements I present extracted values of the saturation fluence to be on the order of 10 $\mu J/cm^2$; five times smaller than that of the "low modulation depth" design. The modulation depths of the absorbers were found to be >1.9%, approximately three times greater than the value reported by Wilcox et al. (2008). Resolution of the absorber response times was limited by the pulse duration of the pump and probe pulses used, however, almost complete recovery of all the SESAMs under investigation had been observed <20 ps after the pump pulse.

The extracted values of the saturation fluence and modulation depth will have an impact on ML-VECSEL cavity design. In section 4.5 I present an investigation of a low-mode area ratio cavity design. Mode-locked output was observed for an gain-SESAM area ratio of 2:1, representing the lowest observed mode-area ratio in a surface-recombination SESAM ML-VECSEL.

Sample Name	Nominal QW indium concentration (%)	Design Wavelength (nm)	Spacer Layer Thickness (nm)	Stop-band Design Centre Wavelength (nm)
A4234	25	1030	13.5	1020
V623	26	1000	13	1010
W255	28	1040	13.5	1020

Table 4.1: Table containing the design parameters of the surface-recombination SESAM structures under investigation.

4.1 Description of SESAMs Under Investigation

The arrangement of layers for a surface-recombination SESAM is shown in figure 2.11. All 3 structures under investigation are designed with a single $In_xGa_{1-x}As$ QW situated 2 nm from the front surface, and a spacer layer of ~13 nm. The nominal QW Indium concentration, x, and corresponding design wavelength are listed in table 4.1. The indium concentration used is dependent on growth machine and growth conditions and was calibrated prior to the structure growth.

A4234 has been used in the work presented by Quarterman et al. (2009) and Wilcox et al. (2008) and in the work described in chapter 6. V623 was a structure designed for operation at 1000-nm, however, due to mis-calibration of the QW indium concentration the operating wavelength is 1030-nm and has been used in mode-results reported in chapter 6. W255 was designed as a direct copy of A4234 with a greater QW indium concentration to red-shift the operating wavelength.

4.2 Broadband Reflectivity Characterisation

A precise measurement of the linear reflectivity profile provides information about the growth of the structure, location of the absorption feature, and is used to ascertain whether the structure has been grown correctly.

A Cary-5000 UV-Vis-NIR spectrophotometer was used to measure the linear reflectivity of the 3 samples under investigation. Figure 4.3 shows the corresponding measured and designed broadband reflectivity as a function of wavelength on the left, with the right-hand figure in each case showing an expanded view of the measured absorption feature from the QW. The measured absorption feature is a convolution of the intrinsic QW absorption and the electric field enhancement.

Figure 4.3(a) shows the measured and designed reflectivity for A4234. The stopband was designed to be centred at 1020 nm however, when measured the stopband is centred at 1010 nm. The 10-nm offset between design and actual growth will result in a red-shift of both the enhancement and GDD profile by 10-nm, causing an increase in enhancement and magnitude of GDD as shown in figure 2.12. The absorption feature of A4234 is centred at 1018 nm. A4234 was designed to take advantage of the ac Stark effect and, hence was designed to work on the low energy side of the absorber band edge (Wilcox et al. (2008)). For slow-saturable absorber mode-locking, however, operating at a longer wavelength than the centre of the absorption feature will result in a lower modulation depth, and hence, a larger saturation fluence.

The measured and designed reflectivity for V623 is shown in figure 4.3(b). The centre wavelength of the designed and measured stopband are both approximately 1010-nm with a ∼2-nm difference in centre wavelength. The reduction in maximum reflectivity is attributed to the sample dimensions being smaller than the aperture in the spectrophotometer. The absorption feature is centred at 1030 nm, approximately 30 nm longer than the design wavelength. As with A4234, this will result in a red-shift in the absorption and GDD profile.

Figure 4.3(c) shows the measured and designed reflectivity for W255. A centre wavelength of 1020 nm for both the measured and designed reflectivity show good agreement between design and growth. The reduced maximum measured reflectivity is attributed to the mismatch in aperture and sample size. The centre of the absorption feature is approximately 1022 nm. However, as it was a regrowth of A4234, it was also designed to utilise the ac Stark effect and hence operate at a wavelength longer than the absorption feature centre.

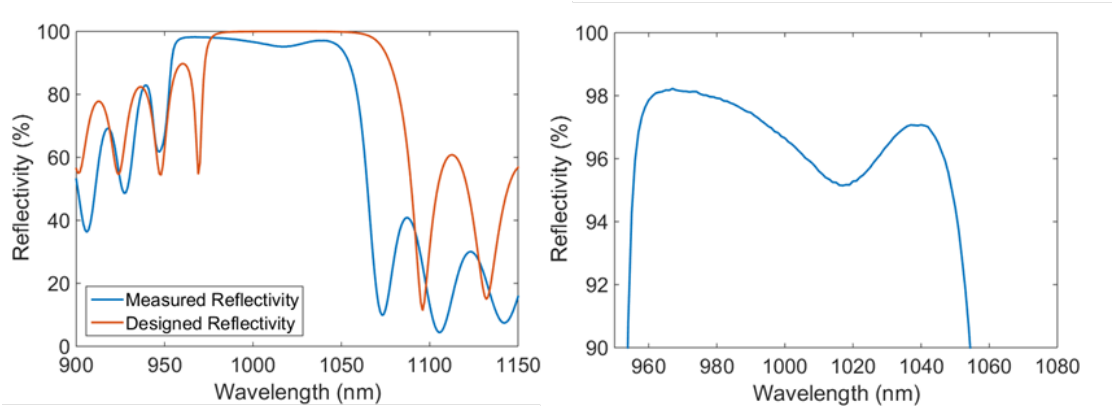

(a)

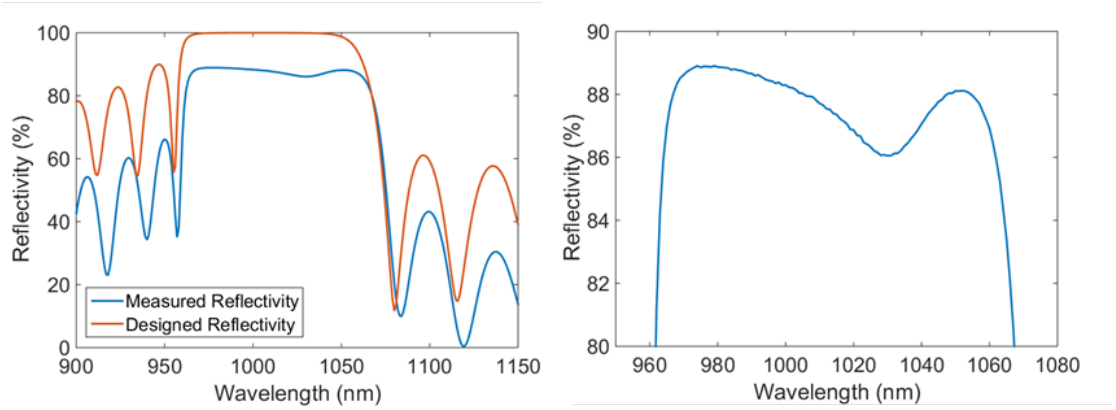

(b)

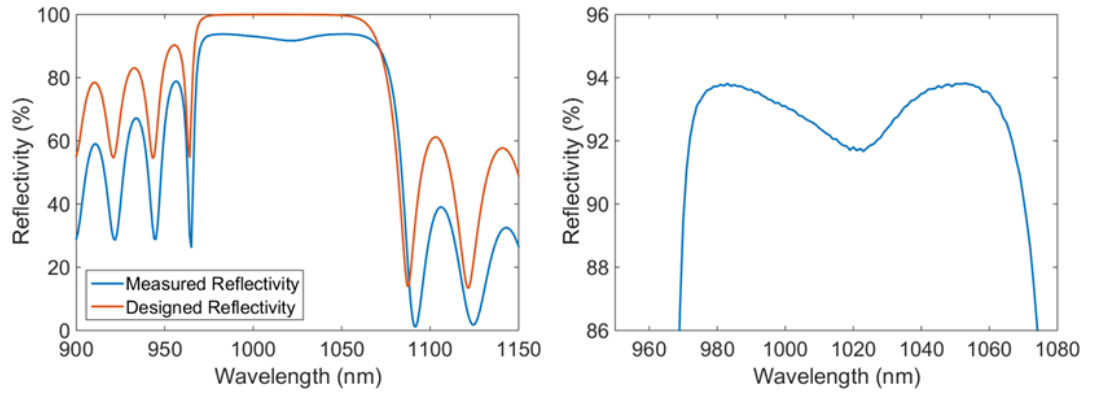

(c)

Figure 4.3: Broadband reflectivity measurements for (a) A4234, (b) V623, and (c) W255. The figure on the left shows the measured linear reflectivity (blue) and designed reflectivity (orange) as a function of wavelength. The right-hand figure shows an expanded view of the stop band and the measured absorption feature.

The broad width of the absorption feature measured for all three SESAMs under investigation is indicative of absorption not being dominated by an exciton transition. The location of the QW only 2-nm from the surface of the SESAM gives an asymmetric confinement potential resulting in an absorber layer that my not behave as a pure QW.

Although it is not possible to accurately determine the exact value of the absorption feature depth through linear reflectivity measurements due to the additional aperture losses, it is possible to determine the overall magnitude of the effect. All 3 absorbers demonstrate a maximum absorption feature depth on the order of several percent; significantly greater than the 0.7% calculated by Wilcox et al. (2008). The cause of the deviation between the calculated and measured values is unknown, though possibly due to the simple ratio used to determine the value. The exact values of modulation depth are determined by non-linear reflectivity measurements in the following section.

The operating wavelength of the structure increases as the indium concentration in the QW is increased, as shown in figure 2.4. For the 3 samples investigated, increasing the indium concentration shows no trend in the measured location of the centre of the absorption feature. Different MBE machines at the University of Cambridge were used to grown each structure. The variability of growth conditions across each machine shows the requirement of accurate growth calibration to ensure that structures are grown as designed.

The repeatability of QW location is also critical for further characterisation of SESAMs as both non-linear reflectivity and pump-probe measurements are performed using external pulsed lasers sources with a fixed operating wavelength and a laser bandwidth typically much smaller than the width of the absorption feature. However, the overlap of laser wavelength and absorber feature may not truly reflect the structure parameters under operating conditions.

The dispersion profile across the absorption feature is set by the relative location of the centre of the feature to the DBR stopband. As mentioned in section 3.2.3, it is difficult to determine the dispersion profile experimentally and we therefore rely on growth of the structure matching the design. A misgrowth of the QW relative to the DBR will alter the dispersion seen by the pulse and may result in longer pulses. For A4234

and V623 the discrepancy between the design of the DBR stopband and centre of the absorption feature will result in a dispersion profile with a more negative value of GDD than designed, as shown by a red-shift in the operating wavelength in figure 2.12.

4.3 Non-Linear Reflectivity Characterisation

The non-linear reflectivity of the structures detailed in table 4.1 was characterised using the experimental setup described by Maas et al. (2008). The reflectivity was probed over approximately four orders of magnitude of pulse fluence and the values of F_{sat}, ΔR, the non-saturable loss and F_2 were extracted.

The design considerations described in sections 2.1.3 and 3.2.2 imply that we require an absorber with a low saturation fluence, large modulation depth and low non-saturable loss.

In this section I detail the theory of slow absorber response to changing fluence and the resulting equation used to extract structure parameters. I describe the experimental setup used and the measured reflectivity as a function of fluence for the three structures under test.

4.3.1 SESAM Non-Linear Reflectivity Theory

A derivation of an analytic expression for the reflectivity of a SESAM as a function of fluence was presented by Haiml et al. (2004). The derivation is outlined here along with the function used to fit the measured non-linear reflectivity and extract the device parameters.

The absorber is approximated by a two-level system, ignoring any semiconductor band-structure and intraband relaxations. Carrier recombination on the timescale of the pulse is neglected, which is a good approximation for a slow saturable absorber such as a SESAM. We neglect any quantum coherence in the generated carriers, and as such have very short dephasing times. We assume no optical coherence and as a result only the electric field intensity is considered. Any effects from carrier diffusion and temperature

are neglected and the incident light is assumed to be monochromatic. In spite of the significant assumptions, Haiml et al. (2004) reported good agreement of the final model with experimentally measured results.

In order to calculate the effect of a saturable absorber on a pulse transmitted through the medium it is necessary to solve the following pair of coupled differential equations:

$$\frac{\partial \alpha(z,t)}{\partial t} = -\frac{\alpha(z,t)I(z,t)}{F_{sat}} \tag{4.2}$$

and

$$\frac{\partial I(z,t)}{\partial z} = -\alpha(z,t)I(z,t), \tag{4.3}$$

where $\alpha(z,t)$ is the time dependent absorption and $I(z,t)$ is the Intensity. In this model we are assuming a one-dimensional variation of both α and I, ignoring any spatial variation across the beam. An analytical solution to the above equations is derived by Siegman (1986) where the reflectivity of an absorber of length $L/2$ is treated as the transmission through an absorber of length L. The reflectivity of the absorber is defined as the ratio of the fluence before and after reflection:

$$R(F) = \frac{F_{out}}{F_{in}} = \frac{\int_{-\infty}^{\infty} I(L,t)dt}{\int_{-\infty}^{\infty} I(0,t)dt} \tag{4.4}$$

$$= R_{ns}\frac{ln[1 + R_{lin}/R_{ns}(e^{F/F_{sat}} - 1)]}{F/F_{sat}}, \tag{4.5}$$

where R_{ns} is the non-saturable loss of the SESAM arising from scattering losses at interfaces and the imperfect reflectivity of the DBR, R_{lin} arises from the unsaturated reflectivity of the SESAM where $F = 0$ and F_{sat} is the saturation fluence. The saturation fluence is defined as the point at which the reflectivity increases from R_{lin} by a factor of $1/e$ ($\simeq 36.8\%$) of the modulation depth of the SESAM, where the modulation depth, $\Delta\mathrm{R}, = \mathrm{R}_{ns} - \mathrm{R}_{lin}$.

It has been experimentally shown by Haiml et al. (2004) that as the fluence incident on a SESAM is increased to arbitrarily high amounts a roll-over in the reflectivity is observed. The reduction in reflectivity is attributed to non-linear effects such as two-photon absorption (TPA) and free carrier absorption and results in an extra induced absorption fitting parameter, F_2. F_2 is defined as the fluence at which the reflectivity has decreased to $1/e$ of R_{ns}. Combining all of the terms results in a fluence dependent reflectivity given by:

$$R(F) = R_{ns}\frac{ln[1 + R_{lin}/R_{ns}(e^{F/F_{sat}} - 1)]}{F/F_{sat}}e^{-\frac{F}{F_2}}. \tag{4.6}$$

The 4 fitting parameters of the model are R_{ns}, R_{lin}, F_2 and F_{sat}. The model has so far neglected any spatial variation of the pulse incident on the absorber, the incident light has been treated as having a flat-topped profile with spatially invariant pulse fluence, F_p, given by:

$$F_p = \frac{E_p}{\pi\omega^2}, \tag{4.7}$$

where ω is the spot radius and E_p is the pulse energy. Instead, we should assume a gaussian profile for the beam where the fluence is given by:

$$F_p^{Gauss}(r) = F_0 e^{\frac{-2r^2}{\omega^2}}, \tag{4.8}$$

where F_0 is the peak fluence of the pulse and ω is the $(1/e^2)$ radius of the beam. The pulse energy can then be defined as the integral of the fluence over the spot:

$$E_p = \int_{-\infty}^{\infty} F_p^{Gauss}(r)2\pi r dr = \frac{1}{2}F_0(\pi\omega^2). \tag{4.9}$$

From equation 4.7 and 4.9 it can be shown that the peak fluence experienced by the absorber is twice the value of F_p. The pulse fluence is defined identically for a flat-topped profile as a gaussian one, only the definition of the spot radius changes. We now

have to take into account the spatial energy distribution when performing the integral to calculate the reflectivity. Equation 4.4 becomes:

$$\begin{aligned} R^{Gauss} &= \frac{E_{out}}{E_{in}} \\ &= \frac{1}{E_p}\int_0^{\infty} 2\pi r \cdot R\left(F_p^{Gauss}(r)\right) \cdot F_p^{Gauss}(r)dr. \end{aligned} \tag{4.10}$$

We define the reflectivity in terms of pulse energy in order to simplify the spatial variation. Using substitution it can be shown that the reflectivity of a gaussian pulse for a given fluence, F_p, is given by:

$$R_{Gauss} = \frac{1}{2F_p}\int_0^{2F_p} R^{FlatTop}(z)dz, \tag{4.11}$$

where $R^{FlatTop}$ is given by equation 4.5:

$$R^{FlatTop}(z) = R_{ns}\frac{ln[1 + R_{lin}/R_{ns}(e^{(z/F_{sat})} - 1)]}{z/F_{sat}}e^{-\frac{z}{F_2}}. \tag{4.12}$$

Equations 4.11 and 4.12 are the functions that are used to extract the structure parameters from the measured non-linear reflectivity as a function of pulse fluence.

4.3.2 Non-Linear Reflectivity Experimental Setup

The experimental setup used to measure the non-linear reflectivity of the SESAMs under investigation is shown in figure 4.4. The output of a pulsed laser source was telescoped and collimated with a beam radius of 1 mm before entering the power attenuation optics consisting of a half-wave plate (HWP) and two polarising beam splitters (PBSs). The first PBS was mounted in a computer controlled rotation stage allowing polarisation rotation and in conjunction with the second PBS, allows attenuation of the power over up to 4 orders of magnitude whilst keeping the polarisation fixed. The attenuation was

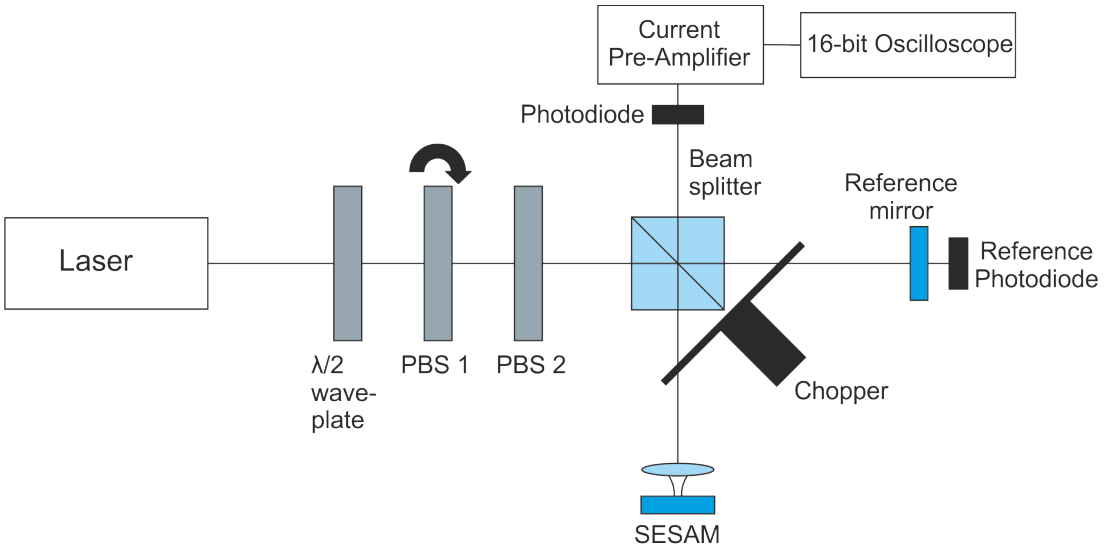

Figure 4.4: Experimental setup to measure the non-linear reflectivity of a SESAM. The pulses laser output is attenuated by the combination of a half-wave plate, rotating polarising beam splitter (PBS1) and a fixed polarising beam splitter (PBS 2). The beam is split into the SESAM and reference arm by a non-polarising beam splitter and modulated by a chopper. Both arms are retro-reflected and measured by a large area photodiode. The output of the photodiode is amplified by a current pre-amplifier and then is input to a PC controlled 16-bit oscilloscope.The reference photodiode behing the reference mirror is used to calibrate the fluence on the SESAM as a function of polariser angle.

set by the extinction ratio of the second PBS; for this setup we use 100,000:1 Glan-Thompson PBSs.

The laser source used in this experiment had an emission wavelength centred at 1030 nm, with a repetition rate of 3 MHz, pulse duration of 1 ps and an average output power of up to 6 W. The output power of the laser was attenuated down to approximately 200 mW prior to the power attenuation optics used in the non-linear reflectivity setup to access the range of fluences required to characterise the three structures under investigation. The fluence range used for characterising the non-linear reflectivity was from 1 - 1300 $\mu J/cm^2$.

A non-polarising 50:50 beam splitter then split the beam into two arms: the SESAM arm and the reference arm. A lens on the SESAM arm focused the beam onto the SESAM. A 20 mm focal length lens was used to achieve a spot radius of approximately 11 μm. Both arms were retro-reflected onto a large area photodiode where the signal

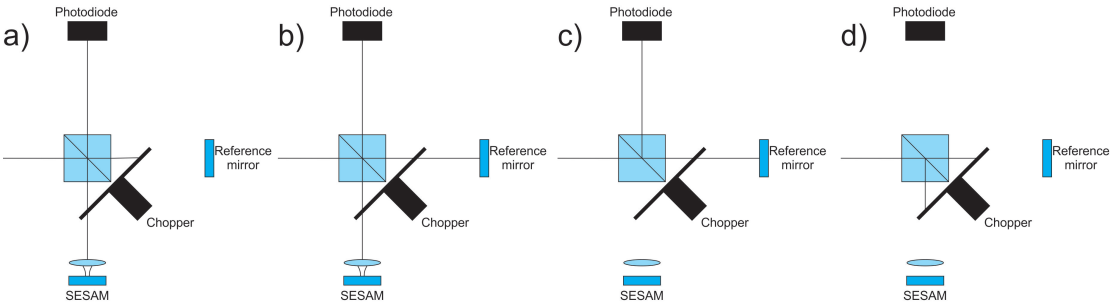

Figure 4.5: The signals recorded by the photodiode for a single cycle of the chopper. a) Signal returned from the SESAM. b) Signals returned from both SESAM and reference arms (not used in the reflectivity calculations). c) Signal returned from the reference mirror. d) Background measurement from both paths blocked.

was amplified by a current amplifier and then output to a 16-bit computer controlled oscilloscope. The signal was modulated by a chopper rotating at ∼100 Hz.

Fig. 4.5 shows the 4 possible states recorded by the photodiode as the chopper rotates. The signal returned from the SESAM is given by state A, where the chopper blocks the reference mirror. The signal returned from both arms (B) is not used in the calculation of the reflectivity. C is the signal returned from the reference mirror and D is the background measurement recorded when both beams are blocked. The reflectivity as a function of the fluence is then given by:

$$R(F) = C(F) \times \frac{A - D}{C - D}, \tag{4.13}$$

where C(F) is a calibration factor. The calibration factor was determined by performing the reflectivity measurement with a dielectric high-reflector in place of the SESAM ($R \simeq 99.99\%$). A mirror with very high reflectivity is needed to get an accurate measurement of both saturable and non-saturable losses. The calibration factor was calculated as a function of fluence in order to remove any systematic errors that may occur as a function of rotation angle, and hence fluence. The theoretical model given by equations 4.11 and 4.5 was then fit to the experimental data and the 4 fitting parameters are extracted.

In order to calibrate the power incident on the SESAM as a function of attenuator angle the high-reflector was replaced with a power meter. The recorded power meter reading was calibrated to a photodiode which measures a small fraction of a percentage of light leaked through the reference-arm mirror. Using the photodiode to reference the incident fluence used during the non-linear reflectivity measurements removed any variation in the fluence due to hysteresis in the motorized rotation stage and fluctuations in laser power.

To ensure that the SESAM was at the focus of the laser beam, the procedure as described by Haiml et al. (2004) was used. The SESAM was translated along the propagation direction and the beam waist occurs where the measured non-linearity is largest, resulting in the smallest measured value of F_{sat}.

In order to minimise measurement errors caused by misaligment when changing between structures under investigation, an alignment beam from a laser pointer was used to calibrate the sample position. The alignment beam is split into two components, as shown in figure 4.6. The first is directly incident onto the structure and the second is aligned onto the structure through a focussing lens. The reflection of the first beam is aligned to an aperture which allows calibration of the angular alignment, ϑ and φ, of the structure. The reflection of the second beam is re-collimated and then aligned to a second aperture, allowing sensitivity to the alignment in the direction of propagation, z. A 0.02% error in realignment is achieved through this method.

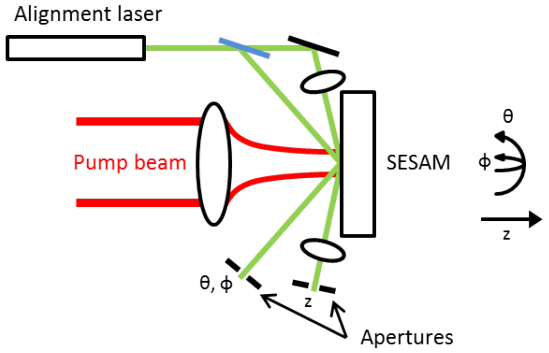

Figure 4.6: Schematic of the two alignment beams used to reproduce sample position.

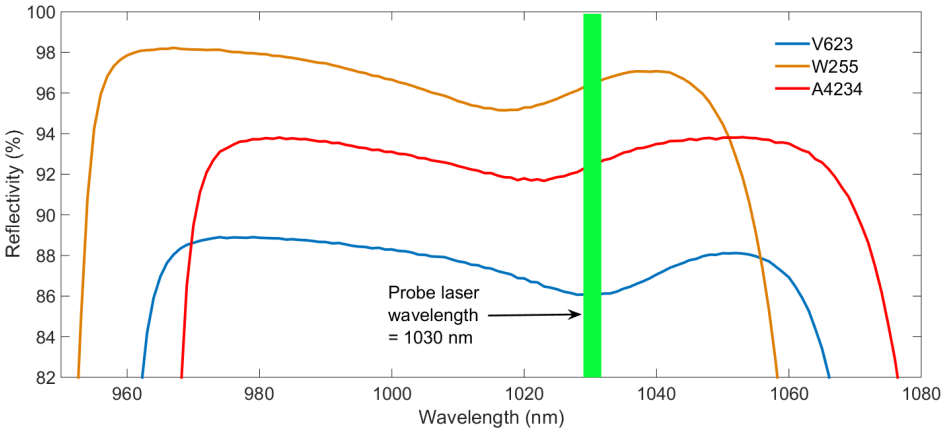

Figure 4.7: Measured reflectivity as a function of wavelength for the 3 structures under test. The green line indicates the overlap of the probe laser wavelength with the absorption feature for both the non-linear reflectivity and pump-probe measurements.

4.3.3 Measured Non-Linear Reflectivity

The 1030-nm probe laser used in this experiment is not spectrally aligned with the centre of the absorption feature, as shown by the linear reflectivity measurements in figure 4.7. Thus the resulting measurements may not accurately reflect the SESAM parameters at the operating wavelength. However, the extracted parameters will still be useful for evaluating the suitability of current SESAM designs for use in high average power ML-VECSELs.

Figure 4.8 shows the measured reflectivity and calculated theoretical fit as a function of incident pulse fluence for each of the structures under investigation. Figures 4.8 (a), (b) and (c) correspond to A4234, V623, and W255 respectively. The extracted fit parameters are listed in table 4.2. The results shown are representative of multiple measurements taken at different spots on each SESAM. I will consider each parameter individually and evaluate the effect on laser performance and cavity design.

4.3.3.1 Saturation Fluence, F_{Sat}

Potentially the most important of the extracted parameters is the saturation fluence as it dictates overall cavity design and achievable pulse energies as discussed in the previous

chapters. The characterisation of the QT1627 yielded a saturation fluence of 56 ± 3 μJ/cm^2 and as a result required gain-SESAM mode-area ratios between 20 and 40 to achieve mode-locked operation (Wilcox (2006)).

The measured saturation fluences for the three absorbers under investigation are of the order of 10 μJ/cm^2. A4234 has the largest F_{sat} of 12.2 ± 1.2 μJ/cm^2, caused by having the largest offset between laser wavelength and centre of the absorption feature, reducing the absorber-pulse interaction and therefore requiring more energy to saturate the QW. W255 has a F_{sat} of 8.6 ± 0.6 μJ/cm^2 and V623 has the lowest of 7.4 ± 0.4 μJ/cm^2 due to being closest to resonance with the centre of the absorption feature. The wavelength of the absorption feature with respect to the laser pulse is likely the main cause of the difference in saturation fluence between the structures. Although, small changes in structure design and therefore electric field enhancement on the QW are likely to contribute some effect in changing the saturation fluence.

The measured fluences being approximately five times less than the QT1627 greatly reduces the restrictions placed on cavity design and mode-area ratio required to support mode-locked operation. A five times reduction in saturation fluence corresponds to the laser supporting a mode-area on the SESAM five times greater than previously used whilst achieving the same pulse shaping and also reducing local heating.

It is possible to estimate the maximum average output power for an ultrafast VECSEL mode-locked using the SESAMs characterised here using the following equation:

$$P_{ave} = \frac{S \cdot F_{sat} \cdot A \cdot f_{rep}}{T_{oc}}, \tag{4.14}$$

where S is the saturation parameter of the SESAM, F_{sat} is the SESAM saturation fluence, A is the mode-area on the SESAM, f_{rep} is the cavity repetition rate, and T_{oc} is the transmission of the output coupler in percent. To maximise the pulse shortening per absorber interaction and, hence, minimise the pulse duration from the laser, we require a value of S to be on the order of 10 as shown by figure 3.2. For the measured F_{sat} of approximately 10 μJ/cm^2, a SESAM mode radius of 100 μm, a repetition rate of 1 GHz, and an output coupling of 1%, we arrive at an average output power of 300

mW. The laser parameters used in this calculation represent real world values used in current ML-VECSELs. By scaling the SESAM mode radius to 200 µm for the same laser parameters the average output power can be increased to 1.2 W. Using a 200-µm radius spot on the SESAM and a 1:1 mode-area ratio would require a mode radius of 200 µm on the gain structure. Mode-radii of 200 µm or greater can be supported using processed "flip-chip" gain structures (Chernikov et al. (2011)).

Although any gain interactions have been neglected, this simple calculation illustrates that the SESAMs under investigation are well suited to the desired Watt-level performance from a ML-VECSEL. The simulation by Sieber et al. (2013) indicated a required saturation fluence of 10 µJ/cm^2 with a SESAM mode-radius of 200 µm for the construction of a 1:1 mode-area ratio Watt-level 200-fs VECSEL. An investigation into the use of the surface-recombination SESAMs characterised here for 1:1 mode-area ratio mode-locking is reported in section 4.5.

4.3.3.2 Modulation Depth, ΔR

The extracted fit parameters yields a ΔR of 2.1 $\pm$ 0.04% for A4234, 3.11 $\pm$ 0.05% for V623, and 1.89 $\pm$ 0.03% for W255. These values indicate that the calculation Wilcox et al. (2008) used to arrive at the value of 0.7% is incomplete. The model presented by Sieber et al. (2013) gives a requirement for a SESAM to have a modulation depth of 2% for a 1-W 200-fs ML-VECSEL, which the structures under investigation are consitent with. In the case of V623 which has a modulation depth at 1030 nm of 3.1%, pulses shorter than 200 fs may be achievable but at the expense of higher average powers due to the greater loss.

Saraceno et al. (2011) derived an expression relating F$_{sat}$ and ΔR to the 2-D transparency carrier density, N_0, of the absorber:

$$F_{sat} \cdot \Delta R = h\nu N_0, \tag{4.15}$$

where $h\nu$ is the incident photon energy. For SESAMs with the same absorber section the product of F$_{sat}$ and ΔR remain constant. N_0 is dependent on the material composition,

wavelength, temperature and the electric field enhancement. However, as the 3 absorbers under investigation have similar designs we would expect values of N_0, and hence the product of F_{sat} and ΔR, to be constant.

Calculated values for the absorbers under investigation are: 25.6 ± 0.3 μm/cm^2 for A4234, 23.0 ± 0.1 μm/cm^2 for V623, and 16.3 ± 0.1 μm/cm^2 for W255. These values highlight that, although the absorber designs are similar, the value of N_0 for each SESAM varies across the 3 absorbers under investigation. The variation may be due to the observed discrepancies between the growth and design of the absorber structures shown in the linear reflectivity measurements. The growth discrepancies resulted in greater electric field enhancement on the QW for both A4234 and V623, although, this would reduce the fluence required to saturate the absorber and hence reduce the calculated product. As each SESAM was grown in a different MBE machine, the variation in growth across the three structures may result in differences in intrinsic material parameters which also affects the calculated product.

4.3.3.3 Non-saturable Loss, R_{ns}

To reduce the loss of output power from the insertion of the SESAM in the cavity, the structure non-saturable losses must be made small. Values on the order of a fraction of a percent are acceptable as they are small compared to saturable loss and typical cavity loss from output coupling. The extracted parameters give values of 0.2 ± 0.04% for A4234, 0.32 ± 0.03% for V623, and 0.27 ± 0.02% for W255. The values are small compared to the extracted modulation depth of the three SESAMs and fall within acceptable limits. No implanted defect sites were required to speed up absorber recovery rates, allowing the non-saturable loses in surface-recombination SESAM designs to be kept small. For high-average power operation high quality growth must be ensured to keep non-saturable losses small to limit thermal damage of the structure.

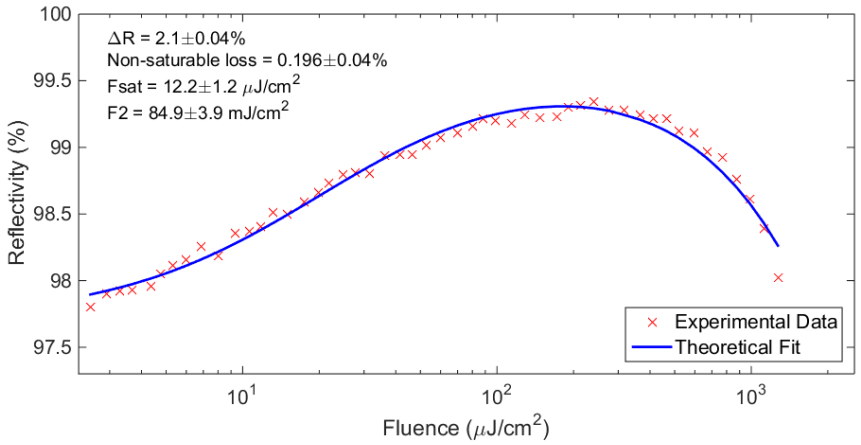

(a)

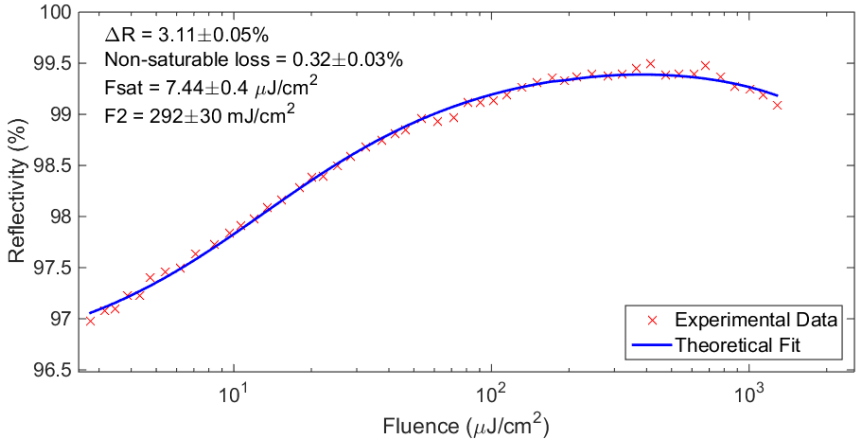

(b)

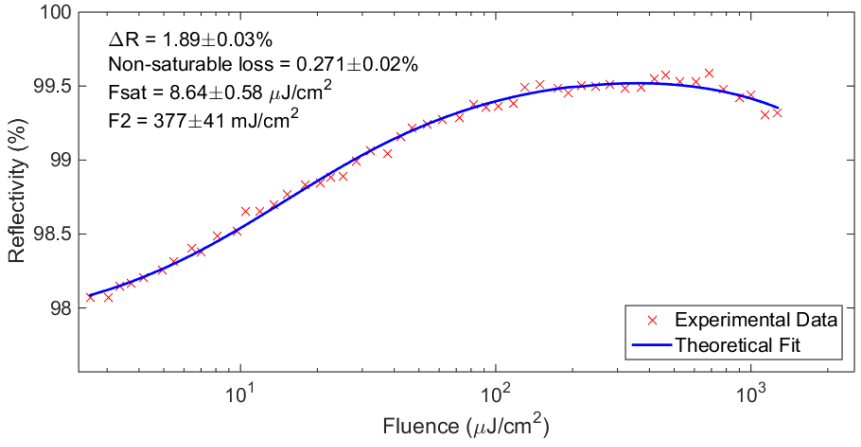

(c)

Figure 4.8: Non-linear reflectivity measurements as a function of pulse fluence for (a) A4234, (b) V623, and (c) W255. The theoretical fit applied to each measurement is from equation 4.11. The extracted parameters for the 3 structures under test are listed in table 4.2.

4.3.3.4 Induced Absorption, F_2

The induced absorption fit parameter F_2 in equation 4.6 is included to model the response of the absorber at large incident pulse fluences. We require the value of F_2 to be made large to reduce the roll-off in reflectivity at high pulse fluences. Induced absorption arises from second order effects such as TPA and, as a result, scales with the square of the pulse intensity. The non-linear effects increase with increasing power and decreasing pulse duration and, therefore, induced absorption is of particular interest in the pursuit of high-power ultrafast ML-VECSELs.

The probe laser has a pulse duration of 1 ps which will result in an extracted value of F_2 larger than the value a 200-fs pulse with the same pulse energy will experience under operating conditions. It will however provide a useful benchmark for comparing the suitability of the three SESAMs for high-power operation. Induced absorption is not solely due to pulse-QW interaction and, in fact, occurs through the whole absorber structure, including penetrating into the DBR. The overall thickness, and material composition of the SESAM will have the greatest effect on the magnitude of the F_2 parameter. Due to the similarity of the structure design and material composition of the three structures under investigation it is predicted that the measured values of F_2 should be of a similar magnitude.

The values of F_2 extracted from the non-linear reflectivity measurements are: 84.9 $\pm$ 3.9 mJ/cm^2 for A4234, 292 $\pm$ 30 mJ/cm^2 for V623, and 377 $\pm$ 41 mJ/cm^2 for W255. Figure 4.8(a) shows the reflectivity sharply dropping off for A4234, agreeing with a low value of F_2. The reason for A4234 having a value of F_2 approximately four times smaller than that of V623 and W255 is unknown as structure designs were similar as mentioned above. Other effects may contribute to induced absorption such as thermal effects and free carrier absorption, although TPA is the dominant effect at ultrafast pulse durations (Haiml et al. (2004)). All three structures were soldered to a copper heatsink with indium foil using the same process, therefore it is unlikely that thermal effects are the dominant cause of the reduction in F_2 for A4234. The relative errors in F_2 for V623 and W255 are approximately twice that of A4234 as there is less of a

response at high fluences, resulting in a larger error in the fit. With the greatest value of F_2, W255 appears to be the most promising SESAM for high-power operation.

There have been no reports on the required magnitude of F_2 for high-power VECSELs, and the effect is not included in the model presented by Sieber et al. (2013), although some consideration has been given in the design of SESAMs for high-power diode-pumped solid-state disk lasers (Saraceno et al. (2011)). As the dominant mechanism is TPA in the low-bandgap materials used in the absorber structure one method to increase the value of F_2 would be to replace the GaAs barrier with AlAs as has been demonstrated in low-temperature grown QW SESAMs (Mangold et al. (2013); Zaugg et al. (2014a)). However, due to the structure design of a surface-recombination SESAM this may not be possible. Replacing the 2-nm GaAs capping layer with AlAs is not feasible due to oxidation which would cause sample degradation. In order to reducing the TPA occuring in the absorber layer it would be possible to replace the spacer layer with AlAs, which may provide a route to maximising the value of F_2 although there would still be a significant contribution from the GaAs layer in the DBR. Future growths of absorber structures will be performed to investigate the effectiveness of replacing GaAs with AlAs.

Overall, the non-linear characterisation of the structures under investigation has given insight into their suitability for high-power sub-200 fs operation. The extracted values of F_{sat} and ΔR correspond to those put forward by Sieber et al. (2013) for the development of a 1-W 200-fs mode-locked VECSEL. The measurement of a value of F_{sat} approximately five times less than that of "low modulation depth" SESAM designs will greatly impact cavity design considerations for future mode-locked VECSELs. Of the three structure both W255 and V623 seem best suited to high-power operation with a larger value of F_2, however, with gain structures designed to operate at 1030-nm and above V623 may prove more promising when the measured absorption feature from the reflectivity measurement in figure 4.3 is also considered. V623 has been used to generate high-power ultrashort pulses as shown in chapter 6.

Sample Name	Saturation Fluence ($\mu J/cm^2$)	Modulation Depth (%)	Non-saturable Loss (%)	Induced Absorption (mJ/cm^2)
A4234	12.2 ± 1.2	2.1 ± 0.04	0.2 ± 0.04	85 ± 3.9
V623	7.4 ± 0.4	3.11 ± 0.05	0.32 ± 0.03	292 ± 30
W255	8.6 ± 0.6	1.89 ± 0.03	0.27 ± 0.02	377 ± 41

Table 4.2: Table containing the extracted parameters from the fit applied to the non-linear reflectivity measurements performed on the three samples under investigation. Equations 4.5 and 4.11 were used to fit the measurements shown in figure 4.8.

4.4 Pump Probe Characterisation

Based on the requirement of fast recombination times, SESAM structures are optimised either by design or by growth to provide fast recombination channels for the excited carriers, as described in section 2.1.3. By using a pump-probe setup it is possible to measure the time response of an absorber to an incident pulse and extract the time constants of the recovery channels. Initially a high energy pump pulse is used to saturate the absorber. The probe pulse is then delayed with respect to the pump pulse using either an optical or mechanical delay line allowing direct measurement of the absorber reflectivity as a function of time after the incident pump pulse.

There have been reports of a double exponential fit of the form:

$$R_{pp}(\tau) = A_1\ exp(-\tau/\tau_{slow}) + A_2\ exp(-\tau/\tau_{fast}), \tag{4.16}$$

used to fit the measured time response of a SESAM (Zorn et al. (2008); Hoffmann et al. (2010)). A_1 is the amplitude of the slow component and A_2 is the amplitude of the fast component and τ_{slow} and τ_{fast} are the slow and fast recover time constants respectively. Zorn et al. (2008) reported on the recovery rates of a dielectric coated surface-recombination SESAM extracting a value for τ_{fast} of 0.3 ps and τ_{slow} of 1.0 ps.

In the simulations performed by Sieber et al. (2012) the value of the response times was found to have little effect on the final steady-state pulse duration which contradicted measured femtosecond experimental results. However, both simulation and experiment agreed that a value of A_1 <50% was required for stable mode-locking. Overall maximising the speed of both recovery times seems to be a sensible course for the development of ultrafast ML-VECSELs.

In this section I describe the experimental setup used to measure the temporal response of a SESAM before evaluating the measured response from the 3 structures under investigation.

4.4.1 Pump-Probe Experimental Setup

Figure 4.9 shows a schematic of the pump-probe setup used to measure the temporal response of a SESAM. The initial output of a pulsed laser source is split into two beams: the high-power pump beam and the low-power probe beam. The energy of the probe pulse must be sufficient to saturate the absorber and the probe pulse must have a small enough fluence to not cause cause any further saturation effects. As a result the pump-probe fluence ratio must be greater than 10:1. Power attenuation on both pump and probe arms are used to set the pump and probe fluences. The pump beam is passed through an optical delay line on a computer-controlled mechanical stage to provide a temporal delay with respect to the probe pulse. The pump is then incident on the structure under investigation at a small angle. The probe beam hits the sample under normal incidence and is overlapped with the pump beam. Part of the reflected probe beam is then picked off and measured with a photodiode. For each time delay of the pump pulse the changes in absorber transmission are measured. To achieve high signal-to-noise both beams are intensity modulated by an acousto-optical-modulator (AOM) and lock-in detection is used.

The mode-locked Yb:YAG laser used had a centre wavelength of 1030 nm, an average output power of 105 mW, a repetition rate of 38.5 MHz and a 2-ps FWHM pulse width. The offset between laser wavelength and centre of the absorption feature is shown in figure 4.7.

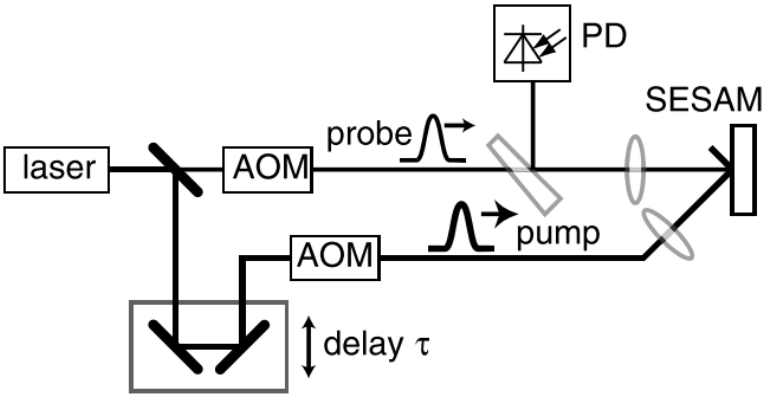

Figure 4.9: Schematic of a pump-probe setup used to characterise the temporal response of a SESAM. A pulsed laser is split into pump and probe beams. The pump beam is delayed with respect to the probe beam using a computer-controlled mechanical delay line. Pump and probe beam are then overlapped on the structure under investigation. Part of the reflected probe beam is picked off and directed onto a photodiode to measure the response of the SESAM as a function of the mechanical delay. Figure from Okhotnikov (2010).

4.4.2 Measured Pump-Probe Response

Figure 4.10 shows the measured absorber response for (a) A4234, (b) V623, and (c) W255 respectively for a range of pump and probe fluences. All of the figures show that using pump and probe pulse duration of 2 ps it is not possible to resolve the fast component of the recovery. In order to resolve and extract τ_{fast} a laser with a short pulse duration compared to the recovery time must be used, which at the time, was not possible.

The main slow recovery channel for surface-recombination SESAMs is the tunnelling of carriers to sites on the structure surface that facilitate carrier recombination. As the design of the thickness of the capping layer is identical for all three structures the only difference in recombination times will be down to and discrepancies in growth and the difference in band-gap of the QW. Figure 4.10 shows that for all the absorbers there is negligible slow component left 10 ps after the incident pump pulse giving an almost complete absorber recovery on that time-scale. A4234 appears to have the fastest recovery with the slow-recovery component barely distinguishable from the response of the pump and probe pulse. V623 has the longest recovery time with measurable slow-recovery tail at 10 ps after incident pump pulse.

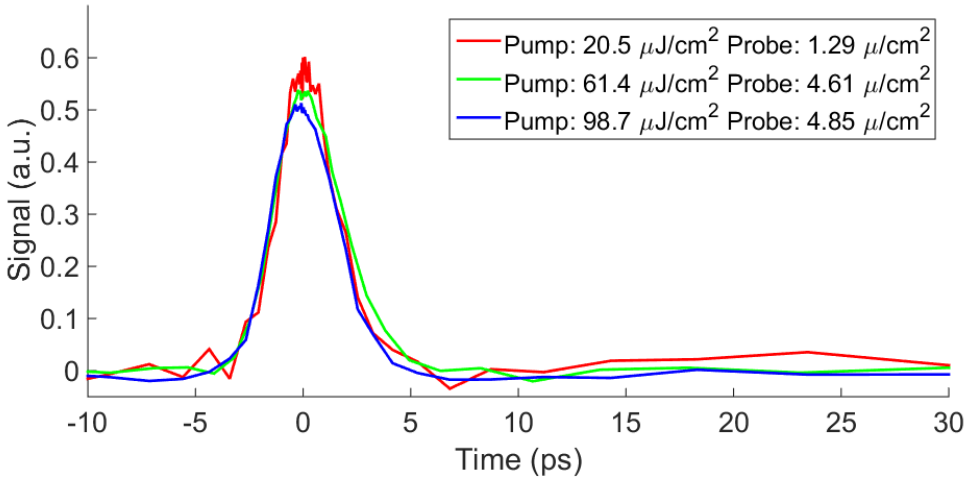

(a)

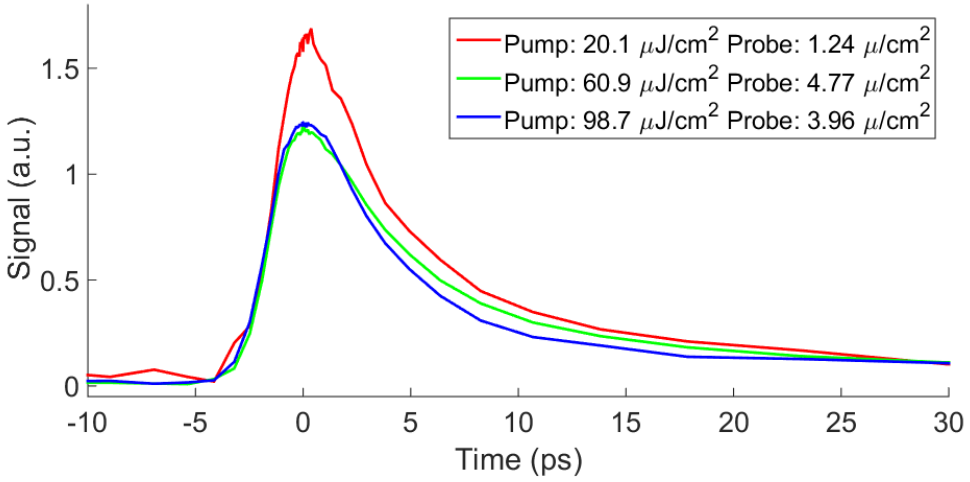

(b)

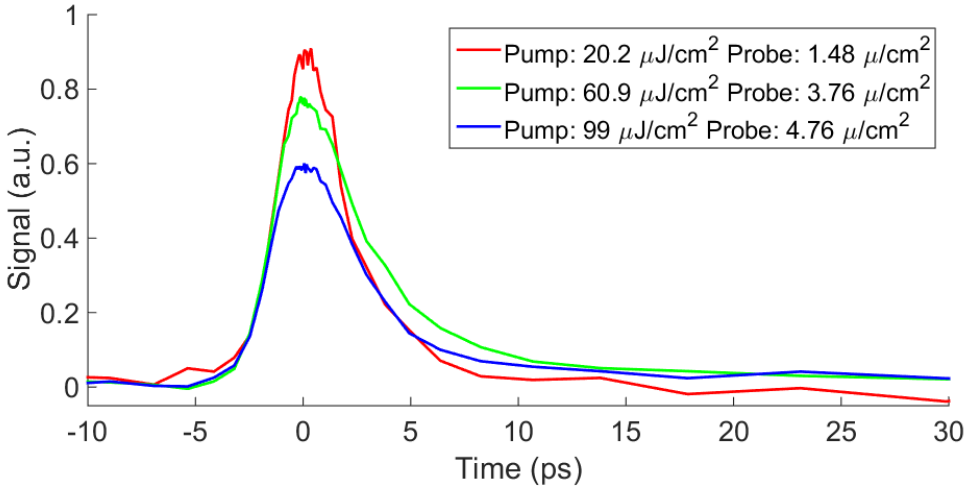

(c)

Figure 4.10: Pump-probe response for (a) A4234, (b) V623, and (c) W255 for three incident pump and probe fluences.

It was not possible to fit the double exponential function given in figure 4.16 due to the convolution of the pump pulse with the fast decay. A single exponential function was fit to the measured pump probe signals to extract an estimation for the slow recovery time. For A4234 the measured temporal profile of the recovery does not show any slow component and, therefore, it was not possible to determine a slow recovery rate. The exponential fits for V623 and W255 are shown in figure 4.11 for the pump fluence of 61 $\mu J/cm^2$ and a probe fluence of 4.7 $\mu J/cm^2$. The exponential fit for gave a value of 5.7 ± 0.5 ps for V623. The value of τ_{slow} extracted for W255 was 3.3 ± 0.3 ps. The values extracted from the fit are, at best, approximations, due to the possible convolution of the slow recovery rate with the pump pulse as the extracted values are on the order of the pulse duration. Difference in growth conditions may be the cause of the large variation in slow recovery rates across the three SESAMs, however, it is not possible to determine the exact cause. The slow recombination rates for other SESAMs reported on are shown in table 4.3. Zorn et al. (2008) measured values of the slow recovery component of 1 ps for a dielectric-coated surface-recombination SESAM with a 2-nm GaAs capping layer and 5.4 ps with a 5-nm GaAs capping layer. Garnache et al. (2003) reported a recombination time of 21 ps using a time resolved photoluminescence measurement. Zaugg et al. (2014a) and Mangold et al. (2014) reported recombination times of 2 ps and 4.1 ps respectively using a SESAM based on a single QW embedded in an AlAs barrier layer. Slow recovery times on the order of picoseconds have been shown to be fast enough to shape pulses down to 100-fs pulse durations (Klopp et al. (2009)). The measured recombination times on the order of ps mean the current design of absorber is well suited to forming ultrafast pulses.

The measurements were performed as for pump fluences between 20 and 100 $\mu J/cm^2$, approximately between 2 and 10 times F_{sat}. The peak signal in the pump-probe measurements should increase with fluence of the pump pulse corresponding to an increase in reflectivity with fluence as shown in figure 4.8. The peak response of the pump-probe measurements show no correlation between fluence and peak response for the absorbers. The results for A4234 show the response is almost constant, although slightly decreases, for increase pump fluence. The lowest pump fluence used in the measurement on V623

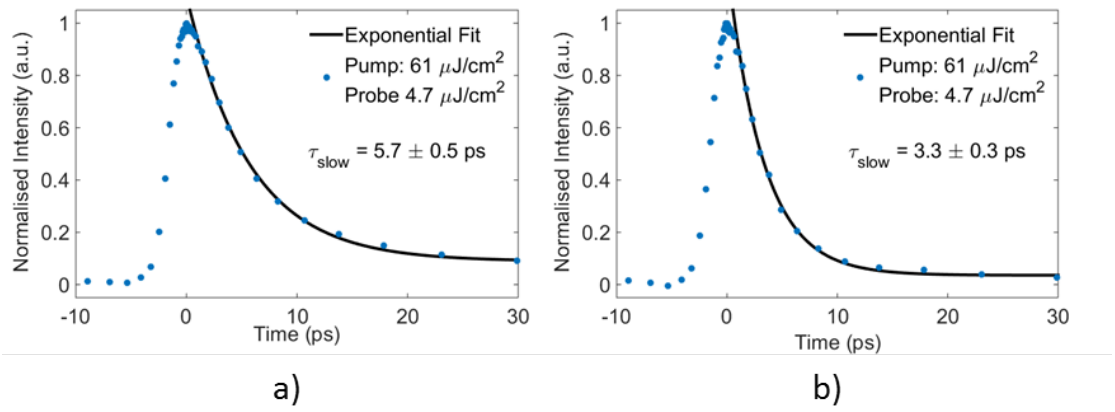

Figure 4.11: Pump probe response for a) V623 and b) W255 for a pump fluence of 61 μJ/cm^2 and a probe fluence of 4.7 μJ/cm^2. An exponential fit is applied to the temporal response for time >1 ps.

SESAM Recombination Times		
SESAM	Slow Recovery Time	Reference
V623	5.7 ± 0.5 ps	-
W255	3.3 ± 0.3 ps	-
Surface Recombination - 2-nm capping layer	1 ps	Zorn et al. (2008)
Surface Recombination - 5-nm capping layer	5.4 ps	Zorn et al. (2008)
Surface Recombination - 2-nm capping layer	21 ps	Garnache et al. (2003)
QD SESAM	15.9 ps	Hoffmann et al. (2011)
Embedded QW SESAM	2 ps	Zaugg et al. (2014a)
Embedded QW SESAM	4.1 ps	Mangold et al. (2014)

Table 4.3: Slow recombination rates for SESAM designs reported in VECSEL literature.

shows the greatest returned signal, with the other two almost constant. The measurements performed on W255 show a decreasing response for increasing pump fluence. The rather random nature of the peak temporal response of the SESAM to increasing fluence may be due to alignment error in the experimental setup.

The observation of almost complete absorber recovery on time-scales shorter than 10-ps make surface recombination SESAMs attractive for the pursuit of ultrafast mode-locked VECSELs at high GHz repetition rates. Although, further characterisation with a pump pulse duration short compared to the recovery times is required to make informed decisions on the effect structure design has on recovery rates.

4.5 Low Mode-Area Ratio VECSEL

Mode-area ratios for surface-recombination SESAM ML-VECSELs have ranged from 10 to 40 using A4234 or a similar structure designed for operation at 1000 nm (Quarterman et al. (2009); Wilcox et al. (2011b, 2008)). Dielectric-coated surface recombination SESAMs have been used with mode-area ratios of 25 (Klopp et al. (2009, 2011)). A ML-VECSEL with a mode-area ratio of 5.6 exhibiting pulses with 335-fs FWHM duration at 120 mW average output power was demonstrated by Wilcox et al. (2010a), representing the lowest mode-area ratio using a surface-recombination in VECSEL literature.

I investigated the possibility of 1:1 mode-locking using a surface-recombination SESAM of the above design designed for 1000 nm. It was not possible to use a SESAM characterised in this chapter due to the lack of suitable gain structure. Due to the similarity in structure design it was assumed that the 1000-nm SESAM had similar properties to the absorbers characterised above.

4.5.1 Gain and SESAM Description

The gain sample used, V629, was an unprocessed semiconductor anti-resonant structure designed for operation at 1000 nm. The active region was 7.5$\lambda/2$ thick containing 6 8-nm $In_{0.2}Ga_{0.8}As$ QWs. A $\lambda/4$ thick layer of AlAs capped the active region, resulting

in an anti-resonant structure. The 27.5 layer-pair GaAs/AlAs DBR was centred at 1000 nm. The structure was grown by the University of Cambridge on a 500-μm thick GaAs substrate.

The SESAM used, V628, was a surface-recombination structure designed for operation at 1000 nm. The single $In_{0.2}Ga_{0.8}As$ QW was separated from the DBR by a spacer layer thickness of 13 nm. The DBR was a 27.5 layer-pair GaAs/AlAs structure centred at 1010 nm. V628 was a regrowth of V623 with the QW grown correctly for 1000 nm. It was not possible to characterise the SESAM due to the lack of appropriate laser source at 1000-nm. The gain and SESAM structures were the same as used in the 5.6 mode-area ratio ML-VECSEL reported by Wilcox et al. (2010a).

4.5.2 Mode-locked Results

A 1.08 GHz Z-cavity, schematic shown in figure 2.2, was constructed with a 50 mm radius-of-curvature (RoC) 0.7% output coupler, gain structure, 50-mm RoC high-reflector (HR) fold mirror and the SESAM. The gain structure was pumped by a fibre-couple 808-nm diode laser providing up to 2.5 W of pump power in 60-μm radius spot. The laser mode-radius on the gain was matched to the pump radius. The gain-fold mirror and fold mirror-SESAM distance were varied to investigate a range of mode-radii on the SESAM.

No mode-locking was observed for a 1:1 mode-area ratio, suggesting that the gain saturation fluence of V629 is less than 100 $\mu J/cm^2$. Mode-locking was observed for a spot size of 43 μm on the SESAM, corresponding to an approximate mode-area ratio of 2:1. Gain and SESAM heatsink temperatures of 5 °C and 30 °C respectively were used. The measured spectrum and autocorrelation for an incident pump power of 2 W are given in figure 4.12 (a) and (b) respectively showing a FWHM pulse duration of 320 fs and a spectral width of 4.04 nm, resulting in a pulse 1.3 times transform limited. figure 4.12(c) shows the first 4 harmonics of the laser RF spectrum giving a fundamental repetition rate of 1.08 GHz. The small long wavelength feature in the spectrum is assumed to contribute to the pulse due to the observation of a pedestal-free autocorrelation. The laser had an average output power of 94 mW, which after intial mode-locking onset steadily

decreased over a several minute time duration, before the laser began CW operation. The reduction in output power is attributed to thermally induced loss in the SESAM.

The results here represent the best performance achievable from the laser cavity in this configuration. The laser performance and cavity design give a fluence on the SESAM of 230 $\mu J/cm^2$ and 115 $\mu J/cm^2$ on the gain. The fluence on the SESAM corresponds to a saturation parameter of 23, assuming a saturation fluence on the order of 10 $\mu J/cm^2$. Assuming a saturation parameter on the order of 100 $\mu J/cm^2$ for the gain structure, gives a gain saturation parameter of 1.

The saturation parameter of 23 using an area ratio of 2:1 corresponds to an almost three times reduction in the saturation parameter and mode-area ratio when compared to the results reported by Wilcox et al. (2008) using the same gain and SESAM structures. The reduction in saturation parameter and, hence, increase in pulse shortening per absorber interaction as shown in figure 3.2, has resulted in only a small, $\approx$ 15 fs, reduction in the pulse duration. without knowing the exact value of saturation fluence and modulation depth for the absorber used, the assertions here are, at best, an approximation. The laser characterised here represents the first demonstration of a surface-recombination SESAM ML-VECSEL with a 2:1 mode-area ratio. Although it was not possible to achieve 1:1 mode-locking, these results correspond to almost a reduction by a factor of 3 in required mode-area ratio to demonstrate mode-locked behaviour. The increased mode-area on the SESAM reduces the thermal load and will allow scaling to higher powers without thermally induced damage.

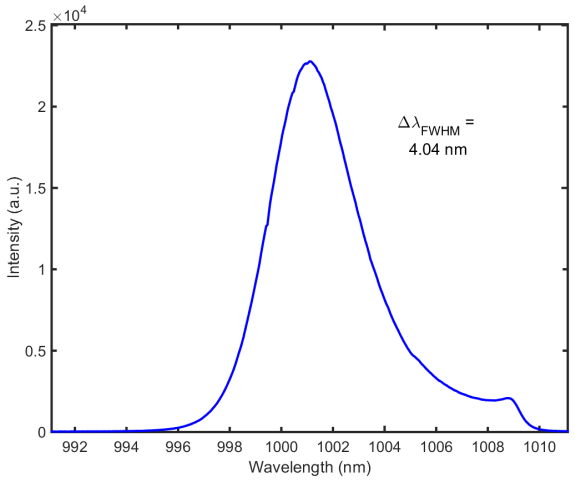

(a)

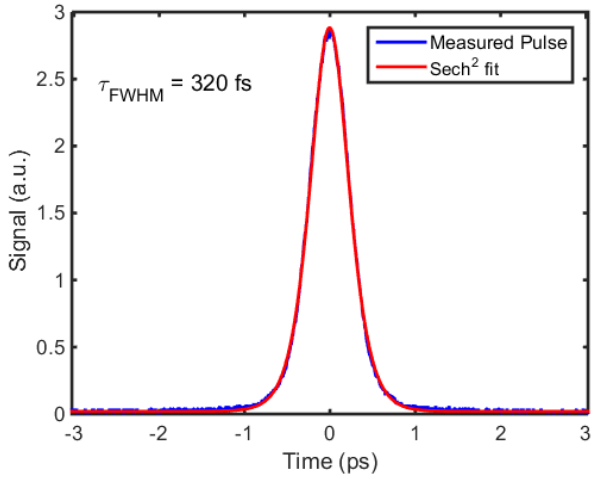

(b)

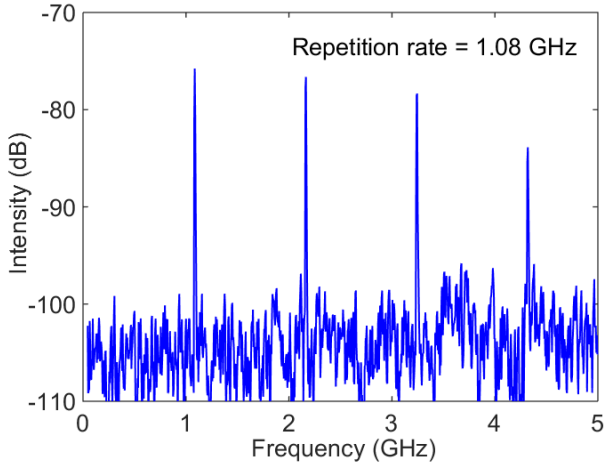

(c)

Figure 4.12: (a) Optical spectrum, (b) autocorrelation with sech^2 fit of pulse, and (c) RF spectrum showing the first 4 harmonics from a mode-locked VECSEL with a 2:1 mode-area ratio between the gain and SESAM. The extracted FWHM spectral bandwidth is 4.04 nm, the FWHM pulse width is 320 fs and the fundamental repetition rate is 1.08 GHz.

4.6 Conclusion

I have described the full characterisation of the three InGaAs QW surface-recombination SESAMs. A4234 and W255 were SESAMs designed for operation around 1030 nm. V623 was designed for 1000 nm, however due to mis-calibration of QW indium concentration the SESAM operated at 1030 nm. The change in structure design from previously characterised absorbers was the reduction of the spacer layer from 40 nm to approximately 13 nm, which caused an increase of the electric field enhancement on the QW. A modulation depth of 0.7% had been calculated for the SESAMs, however, the saturation fluence was unknown. Macroscopic structure parameters were successfully extracted for all three structures under investigation.

The first measurement to ascertain the agreement between structure design and growth was a high-accuracy broadband reflectivity measurement capable of resolving the location and width of the QW absorption feature. A4234 showed an approximate 10-nm discrepancy between design and growth of the DBR whereas V623 and W255 showed good agreement between design and growth. The measurement demonstrated no relation between the indium concentration and the location of the absorption feature, attributed to the differences in growth conditions across the three MBE machines used. Highly repeatable growth is required to ensure that there is little variation over subsequent growths of absorber, especially when evaluating the design choices on new SESAMs. Although all three structures operated at 1030 nm, only V623 had the centre of the absorption feature located at the design wavelength. It was possible to resolve the magnitude of the QW absorption feature, which for all three structures was greater than 2%, more than 3 times greater than the assumed modulation depth.

The second was a non-linear reflectivity measurement to characterise the reflectivity of the SESAMs as a function of incident pulse fluence extracting the modulation depth, saturation fluence, non-saturable losses and induced absorption parameter. The F_{sat} extracted for all three structures was approximately five times less than the "low modulation depth" structure designs, thus, greatly reducing the required mode-area ratio given in equation 3.6 to successfully form pulses. The measured modulation depth from

the three structures agreed with the broadband reflectivity measurement and gave values greater than 2%. The difference in modulation depth between the structures is due to the wavelength offset between of the absorption feature and the pulse. Both the extracted modulation depth and saturation fluence agree with values extracted from simulations performed by Sieber et al. (2013) for what is required for Watt-level 200-fs pulses from a passively mode-locked VECSEL. The extracted non-linear loss was within tolerance for high-power operation. No implanted defect sites were required to speed up absorber recovery rates, allowing the non-saturable loses in surface-recombination SESAM designs to be kept small.

The extracted F_2 values linked to induced absorption showed great variation in the SESAMs under investigation and therefore structure parameters that dominate the magnitude of F_2 require further investigation. Through changing absorber designs to maximise F_2 it will be possible to optimize surface-recombination SESAMs for high-power operation.

A pump-probe measurement was was performed to evaluate the temporal response of a SESAM to an incident pulse to characterise the absorber recovery times. Due to the length of the incident pump and probe pulse it was not possible to observe the fast recombination of the absorbers under investigation. It was observed that all three SESAMs had fully recombined approximately 10 ps after the incident pump pulse. The fast recovery makes surface-recombination SESAMs well suited for forming ultrashort pulses. Further investigation is required using a laser source with pulse durations much shorter than the recombination times, ideally on the order of 100 fs. The use of such a source, which was not possible at the time, will allow extraction of both fast and slow absorber response times and will make it possible to fully characterise any new designs of absorber.

The use of established characterisation techniques has highlighted certain limitations in the extraction of macroscopic structure parameters. The required used of an external laser source to probe the absorber response brings a limitation in excitation wavelength and pulse duration. As has been shown above, if the laser wavelength does not overlap with the absorption feature the resulting characterisation may not represent the absorber

under operating conditions. It also limits the possibility of characterising structures at a wavelength where a laser source is not available, for example, we have existing structures designed for 1000-nm that it was not possible to characterise due to lack of a 1000-nm pulsed laser source.

A laser source with a ps pulse duration will result in extraction of an F_2 parameter greater than experienced with pulse durations on the order of several hundred femtoseconds. Long pulse durations will also result in not resolving absorber response times as mentioned above. Reliance on external laser sources limits the application of the characterisation techniques used in this chapter and therefore developing a characterisation technique that can extract macroscopic parameters from a ML-VECSEL under operating conditions without the need for an external source would be a powerful tool. Pursuit of such a characterisation technique has motivated the work reported in chapter 5.

I have demonstrated a ML-VECSEL using two structures designed for 1000-nm with a mode-radius of 60 μm on the gain and 43 μm on the SESAM, resulting in a mode-area ratio of 2:1. The laser exhibited 320 fs pulses with an average output power of 94 mW in a 1 GHz cavity at a pump power of 2 W. The laser represents the lowest mode-area ratio demonstrated in a surface-recombination SESAM ML-VECSEL. The characteristics of the 1000 nm were assumed to be similar to the SESAMs characterised in this chapter due to the similarity in design.

The work in this chapter has provided a benchmark for absorber designs and parameters optimised for high-power ultrafast operation. New structure designs will be characterised using the above suite of techniques to determine the effect that design changes have on macroscopic parameters.

Chapter 5

Experimental Measurement of Spectrally-Resolved Pulse Formation

In this chapter I describe the work done studying the transient onset of lasing and ultra-short pulse formation in SESAM mode-locked VECSELs for characterisation of VECSEL structures under operating conditions and as an experimental technique to verify models used to predict pulse formation. The technique has its origins in the intracavity laser absorption spectroscopy (ICLAS) measurement used to determine gas phase spectra with good sensitivity using a relatively compact instrument (Garnache et al. (2000, 2007)). The measurement of mode-locking onset times in ML-VECSELs was first performed by Hoogland (2003) on 4.3 ps mode-locked VECSEL where the onset time was measured to be $\sim$4 µs.

Barnes et al. (2010) reported the first instance of a spectro-temporal measurement technique to characterise the spectral filter of a VECSEL gain structure and extract the corresponding parabolic gain bandwidth under operating conditions. The experiment was performed by using an intracavity optical chopper to block and unblock the laser mode of a CW-VECSEL. An acousto-optic modulator (AOM) was then used to deflect the laser spectrum onto a spectrometer at times after lasing onset. The rate narrowing of

the measured spectrum, or spectral condensation, was then used to extract the spectral filter of the gain structure. The gain structure characterised was used by Quarterman et al. (2009) to achieve 60 fs pulses and had a measured gain bandwidth of 51-nm. The temporal resolution was limited to 4 μs due to the response time of the AOM and it was also not possible to record spectra for early times, <18 μs, after lasing onset.

Head et al. (2014) reported an improvement to the above technique. The AOM and spectrometer were replaced with a 1-m stepper-motor-controlled grating monochromator to separate out and record the individual spectral components in the fundamental laser spectrum for times up to 100 μs after lasing onset. The increase in temporal resolution to 32 ns allowed measurement of the spectrum and observation of spectral condensation directly after lasing onset. Measurements were limited to low incident pump powers, and hence not representative of gain bandwidths achieved close to thermal roll-over where it would be broadest. With both high temporal and spectral resolution the technique reported by Head *et al.* would allow observation of the laser spectrum from lasing onset to steady-state operation in a ML-VECELs.

Transient measurements of mode-locking onset have been performed on SESAM mode-locked solid-state lasers (Sun et al. (2001); Sutter et al. (1998)). Typically the second harmonic of the laser output is recorded in parallel with the fundamental output power as a function of the time after lasing onset, where the measurement of a second harmonic signal indicates the presence of a pulse circulating in the cavity. Delay times of between 10 and 100 μs seconds were measured between the initial rise of the fundamental power and the presence second harmonic intensity. The time delay is known as the mode-locking onset time. Kaertner et al. (1995) derived criteria for the dynamic behaviour of SESAM mode-locking in solid-state lasers particularly for self-starting and suppression of Q-switching instabilities. They derived and expression for mode-locking onset time as a function of macroscopic laser parameters.

Using a streak camera, Sarukura and Ishida (1992) were able to measure the spectral evolution of a Ti:Sapphire laser mode-locked by a dye-based saturable absorber both with and without dispersion compensation from a prism pair. Mode-locking onset times of 200 μs and 400 μs were measured with and without the prism pair respectively.

Kuo et al. (1992) and Zinkiewicz et al. (2013) have measured the spectral evolution of a mode-locked solid-state laser along-side the power transients from lasing onset to steady-state operation. However, the use of an AOM limited these measurements to temporal resolutions of greater than 20 μs.

The work performed in this chapter combines the high time resolution spectro-temporal measurement described by Head et al. (2014) with the measurement of fundamental and second harmonic power transients, allowing characterisation of a ML-VECSEL from lasing onset to the final steady-state pulsed operation. These measurements will provide insight into the validity of predictive modelling used for ML-VECSELs and as a technique to understand the dynamics of pulse formation in VECSELs. To date, the spectral evolution of a ML-VECSEL from lasing onset has not been measured.

In the reports on ML-VECSELs there has been a range of structure and cavity designs used to form ultrashort pulses (Tropper et al. (2012)) and to date there has not been a systematic experimental investigation into the effect of changing laser parameters on the formation of pulses. The work presented here is the first attempt at developing a technique to characterise the influence of macroscopic laser parameters on the observed formation of pulses in a ML-VECSEL.

The work in this chapter has also been motivated by the limits of the characterisation techniques presented in the previous chapter, which have a reliance on an external laser source with stringent requirements on operating wavelength, pulse duration and pulse energy. The aim of the experimental technique in this chapter is to investigate the pulse formation dynamics in SESAM ML-VECSELs and provide a method of extracting macroscopic structure parameters under operating conditions.

5.1 Experimental Setup for Spectrally-Resolved Pulse Formation

5.1.1 ML-VECSEL Under Investigation

The laser was used in a z-cavity configuration formed by an 50-mm RoC output coupler, gain structure, 50-mm RoC HR and SESAM. The output coupler transmission was 0.3%. The gain structure was pumped by a fibre-couple 808-nm diode laser providing up to 2.5 W of pump power in 60-μm radius spot. The overall cavity length was approximately 15 cm, corresponding to a 1-GHz repetition rate, and was designed to give an approximate 2:1 mode area ratio between gain and SESAM. Both gain and SESAM were mounted on Peltier-controlled water-cooled copper heatsinks with the temperatures set to be -5 °C and 32 °C respectively. The cavity design and heat-sink temperatures were optimised for long-term laser stability.

The gain and SESAM structures used in this experiment were V628 and V629, described in section 4.5 to demonstrate a low mode-area ratio ML-VECSEL. The structures used were the same reported by Wilcox et al. (2010a) which were capable of 335-fs FWHM pulse durations with an average output power of 120 mW. The VECSEL exhibited stable mode-locked operation for incident pump powers in the range from 700 - 1200 mW. The laser output characteristics as a function of pump power are shown in table 5.1. Average output power and pulse duration as a function of pump power are shown in figure 5.1. Average output power increased from 17 mW to a maximum of 52 mW, with pulse durations decreasing from 410 fs to 345 fs over the range of pump powers used. It is useful to note that the decrease in performance from the laser reported by Wilcox et al. (2010a) was due to the optimisation of the laser for stability rather than performance. With increasing pump power both the FWHM maximum spectral width and multiple of the transform limit both increase also.

It would have been preferable to perform the experiment using 1030-nm absorber structures characterised in the chapter 4 as the macroscopic absorber parameters had been

Pump Power (mW)	Output Power (mW)	FWHM Pulse Duration (fs)	FWHM Spectral Width (nm)	Times Transform Limited
705	17	410	2.4	1.01
800	22	408	2.8	1.05
894	31	392	2.9	1.07
990	37	370	3.2	1.13
1082	43	363	3.5	1.26
1177	52	345	3.6	1.30

Table 5.1: Table containing the output power, FWHM pulse duration, FWHM spectral width and how many times transform limited the resulting pulse was as a function of incident pump power.

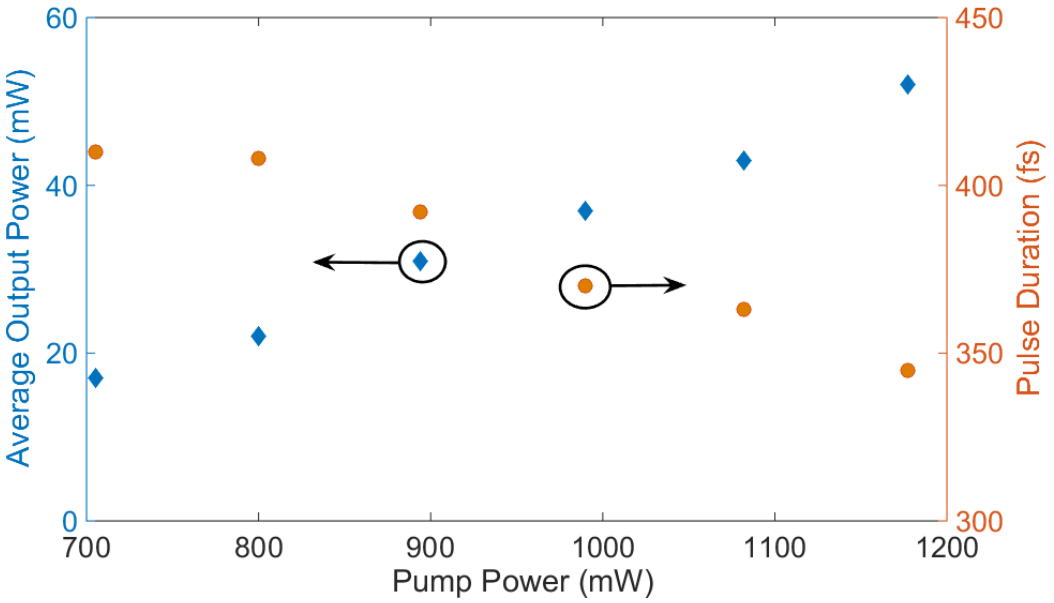

Figure 5.1: Average output power and FWHM pulse duration as a function of pump power of the 1 GHz ML-VECSEL containing V628 and V629.

extracted. However, a gain structure providing stable mode-locking was not available to build a ML-VECSEL.

5.1.2 Experimental Setup

Figure 5.2 shows a schematic of the setup used to investigate mode-locking onset and pulse evolution. An optical chopper was placed in the cavity next to the SESAM in order to block and unblock the laser cavity mode whilst keeping the pumping conditions

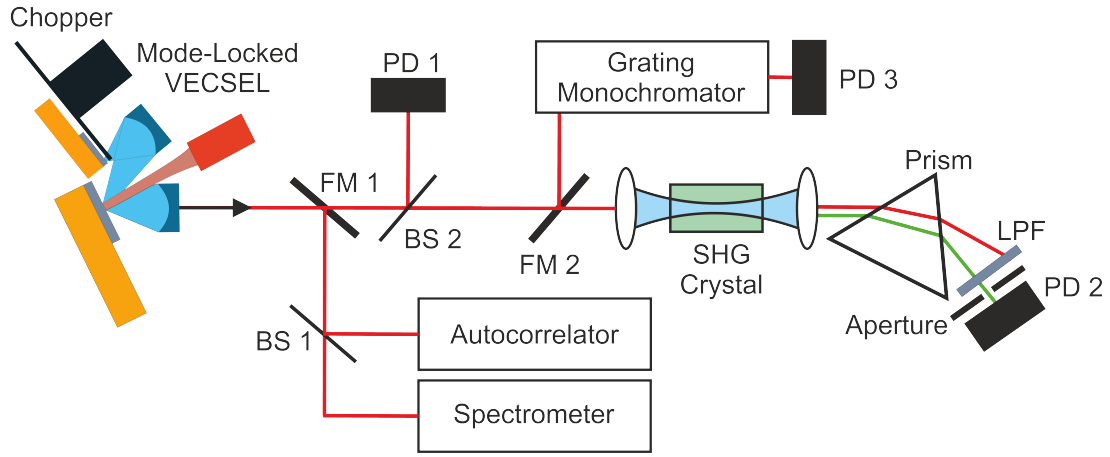

Figure 5.2: A schematic of the spectrally-resolved mode-locked rise-time setup. An intracavity chopper is used to block and unblock the mode of the laser. The fundamental intracavity power rise is measured on a fast photodiode (PD1). The second harmonic is generated in a 300 μm BBO crystal and is then measured on a silicon photodiode (PD 2). The fundamental is spatially separated and removed using a prism, low-pass filter (LPF) and aperture. A flipper mirror (FM2) is used to direct the fundamental through a stepper-motor-controlled grating monochromator and onto another fast photodiode (PD3). The inital output can be directed onto laser diagnostics using FM1.

constant. It was necessary to position the chopper near to a focus in the cavity to ensure the chopper blade uncovered the mode in a time short compared to the rise-time of the laser. The chopper was set to rotate at 170 Hz giving an open window time of ~350 μs. the remaining time the laser mode was covered allowing the laser to fully recover before being switched on again.

A flipper mirror (FM) was placed in the initial beam path before the first beamsplitter (BS) to allow the output of the laser to be characterised by diagnostic equipment. The output of the laser was then split with a 90:10 BS with the low power path directed onto a fast photodiode to observe the fundamental intracavity power rise. The remaining power was focussed through a 300-μm thick BBO crystal for second-harmonic generation. After the non-linear crystal the remaining fundamental was spatially separated from the second harmonic using a prism. A combination of low-pass filer and aperture were used to ensure that no fundamental was incident onto a silicon-based photodiode used to measure the rise of the second harmonic.

A FM was placed before the non-linear crystal to direct the beam through a 1-m, stepper-motor-controlled, grating monochromator and onto a fast photodiode at the monochromator exit. At each stepper motor position the averaged rise for each wavelength component in the fundamental was recorded. Through combining both measurements it is possible to spectrally resolve the evolution of the pulse in the cavity from lasing onset.

The spectro-temporal measurement of the evolution of pulses in the ML-VECSEL under investigation was performed for the range of pump powers over which stable mode-locking was observed. For pump powers in the range of 700 to 1200 mW, in steps of approximately 100 mW, both the transients from lasing onset and the spectral evolution was measured. The length of each measurement was approximately 20 minutes and as a result, laser stability was crucial for performing this experiment.

5.2 Theory of Mode-Locking Onset and Pulse Formation

It is useful to consider three regimes when considering a description of pulse formation based on the above experimental setup. The first is the time period from lasing onset to mode-locking onset. Using the above experimental setup, the first regime is defined as the period from the initial fundamental power rise of the laser to the first detection of a second harmonic component. The second regime is from mode-locking onset to the final steady-state of the laser. The evolution of the second harmonic signal and spectrum over the second regime will indicate how the pulse is forming per round trip. The final regime is the steady-state laser operation. As the laser spectrum and measured power transients do not change in this regime, no information can be gathered about changes of the pulse due to interaction with cavity elements. In the final steady-state regime the required information can be obtained through conventional diagnostics, i.e. autocorrelation and spectrum measurements.

5.2.1 Onset of Mode-locking

Kaertner et al. (1995) have analysed the onset of pulse formation in self-starting SESAM mode-locked solid-state lasers. With the approximation that mode-locking forms from a

Mode-Locking Onset Parameters			
F_{sat}	10 μJ/cm^2	T_{RT}	1 ns
$2q_0$	2%	A_{abs}	5.03×10^{-5} cm^2
τ_{abs}	5 ps		

Table 5.2: Parameters used to calculate the theoretical mode-locking onset time shown in figure 5.3.

single longitudinal cavity mode that couples energy to automatically phase-locked sidebands an expression the mode-locking onset time (T_{MBT}) can be well approximated by:

$$\frac{1}{T_{MBT}} \approx \frac{2\, q_0\, \tau_{abs}}{F_{sat,abs}\, A_{abs}\, T_{RT}} P_{int}, \tag{5.1}$$

where $2q_0$ is the modulation depth of the absorber, τ_{abs} is the absorber recovery time, and $F_{sat,abs}$ is the absorber saturation fluence, A_{abs} is the mode area on the absorber. P_{int} is the average intracavity power and T_{RT} is the cavity round-trip time. The result of 5.1 is based on the assumption that both the upper-state lifetime and round-trip time are long compared to the absorber recovery time and that the upper-state lifetime is long compared to the round-trip time. It neglects any dispersion and spectral hole burning effects and also makes the assumption of monochromatic light and spectrally invariant macroscopic parameters.

Figure 5.3 shows the simulated mode-locking onset time as a function of average output power calculated using equation 5.1 and the parameters in table 5.2. The blue crosses show the calculated theoretical onset times for the average output powers listed in table 5.1. As the average output power of the laser is increased the mode-locking onset time decreases from ∼1 μs at the lowest average output power to ∼ 200 ns at the highest. It is interesting to note that the product of the intracavity power and the mode-locking onset time should remain constant.

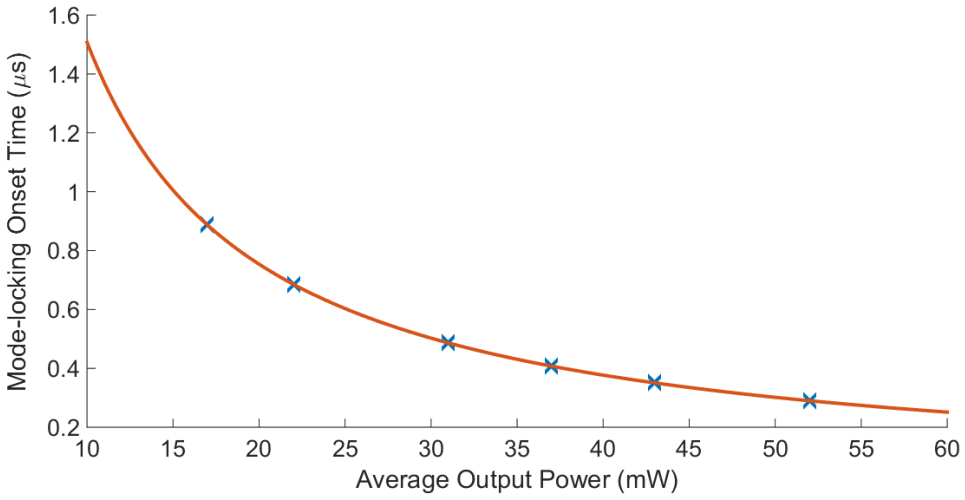

Figure 5.3: Simulated mode-locking onset time as a function of average output power calculated from equation 5.1. The theoretical curve (orange line) is calculated using the measured SESAM parameters from chapter 4 of $F_{sat,abs} = 10$ μJ/cm^2, $2q_0 = 2\%$, and $\tau_{abs} = 5$ ps. Using the cavity parameters for the laser in this experiment gives an $A_{abs} = 5.03 \times 10^{-5}$ cm^2 and a $T_{RT} = 1$ ns. The blue crosses show the theoretical mode-locking onset times for the 6 average output powers given in table 5.1.

5.2.2 Pulse Evolution

Once the mode-locking has started, it is possible to measure how the pulse changes as a function of time by looking at the evolution of the frequency doubled output of the laser. Once the laser is close to stable steady-state mode-locked operation, we can assume that a single pulse is circulating in the cavity, of duration τ, which differs from the steady state value and has a near hyperbolic secant profile. As the second harmonic generated is dependent on the square of the intensity of the pulse we have the following relationships:

$$\begin{aligned} P_{fun}(T) &= \int I(T) \cdot f\left(\frac{t}{\tau(T)}\right) dt \\ &= \tau(T) I(T) \int f(x) dx \end{aligned} \tag{5.2}$$

and

$$P_{shg}(T) = \eta \int I^2(T) \cdot f^2\left(\frac{t}{\tau(T)}\right) dt$$
$$= \eta\tau(T) I^2(T) \int f^2(x)\, dx \tag{5.3}$$

where, $P_{fun}(T)$ and $P_{shg}(T)$ are the integrated fundamental and second harmonic powers respectively as functions of the time after mode-locking onset, T; the signals that would be measured on a photodiode. t is the time in a pulse-centered reference frame and η is a conversion efficiency between the fundamental and second harmonic. We use a function, $f(x)$ to describe the envelope of the pulse, the exact form is not important although it is assumed to be near sech^2. $I(T)$ is the intensity of the pulse.

By squaring the fundamental and dividing it by the SHG signal we can arrive at a relation where the measured value is directly proportional to the pulse length at that point in the rise. The resulting equation is then:

$$\frac{(P(T)_{fun})^2}{P(T)_{SHG}} = \frac{\left(\tau(T) I(T) \int f(x) dx\right)^2}{\eta\tau(T) I^2(T) \int f^2(x)\, dx}$$
$$\propto \tau(T). \tag{5.4}$$

Based on the measurement of the fundamental and second harmonic transients, the above relationship will allow an experimental characterisation of how the pulse length changes per round trip. Increasing the pump power increases the local temperature of the structure and the carrier density, causing a broadening of the gain bandwidth and a reduction of the spectral filter. As a result with increasing pump power, the lengthening contribution from the gain structure per round trip should decrease. As the pump power in increased, below thermal roll-over, the intracavity power will increase increasing the saturation parameter on the absorber. Above a certain saturation parameter, as shown in figure 3.2, increasing the intracavity power will decrease the pulse shortening per round trip from the absorber.

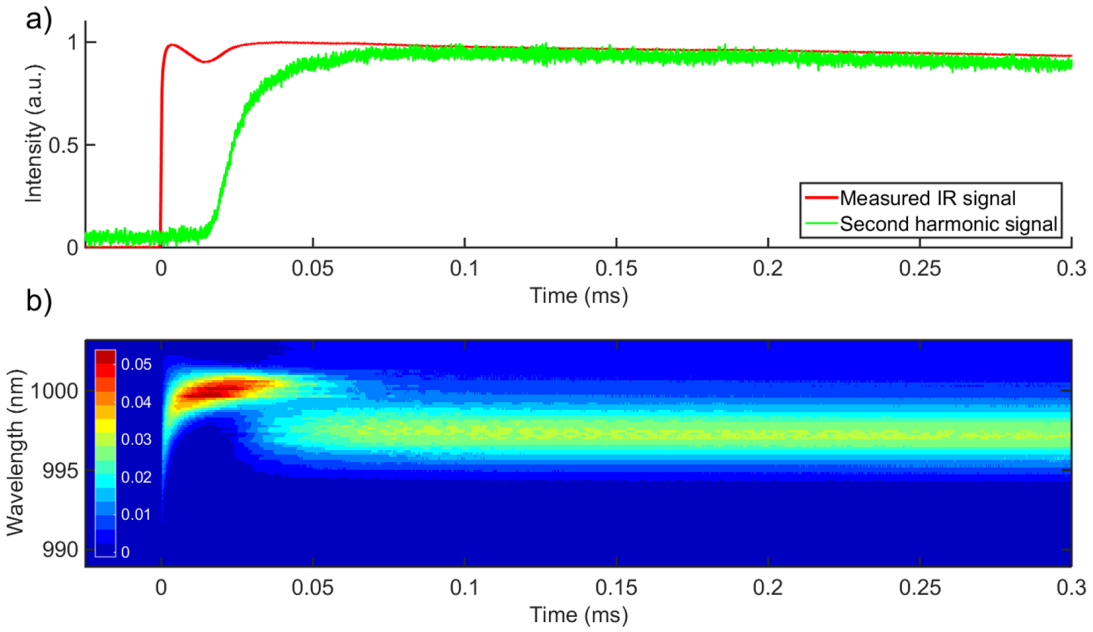

Figure 5.4: Spectrally resolved mode-locked rise time for an incident pump power of 1100 mW. a) Evolution of the fundamental intracavity power (red) and second harmonic of the laser output (green). b) The spectrally resolved intensity of the fundamental laser output.

5.3 Experimental Results and Discussion

Figure 5.4a) shows the fundamental intracavity power rise, the second harmonic and the integrated spectral power as a function of the time after the mode is unblocked for a pump power of 1100 mW. It was chosen as a representative pump power; the transients measured for all other pump powers show the same dynamics when linked with the spectral data. The figure shows that after the initial rise from uncovering the mode and power build up there is reduction in intracavity power followed by a second rise before reaching a steady state. The local minimum in the measured fundamental occurs at the same time that the second harmonic signal rises out of the noise, giving the starting point for the pulse evolution. The decrease in measured fundamental signal indicates the presence of some damped relaxation oscillation prior to the initial formation of the mode-locked pulse. From this time the second harmonic signal rises non-linearly until again reaching a steady state. From the graph we can divide the rise into the three regimes described in section 5.2.

From both the second harmonic signal and the fundamental we can infer that the second rise in the power is the increased saturating of the SESAM as the pulse builds to a steady state. The initial noise spike will not fully saturate the SESAM, resulting in residual saturable losses. As the forming pulse grows in intensity it is further able to saturate the absorber resulting in increased power. The intracavity power reaches a steady state before the second harmonic meaning that, although the intracavity power is constant, pulse shaping mechanisms are not yet balanced. At first the second harmonic signal grows very rapidly with time before slowing down and subsequently levelling off suggesting that once the noise spike has begun saturating the SESAM the initial pulse intensity forms quickly before slowing. The time reported by Sieber et al. (2013) for their model to reach a steady-state pulse solution was approximately 10^4 round trips. Here, where a round trip is approximately 1 ns, the rise takes place over a longer time scale, approximately 50,000 round trips. The assumptions of the model, neglecting real world spectral dependence and unknown parameters, may cause it to converge to a final solution faster. It would be necessary to characterise the gain and absorber used here to simulate the expected formation time based on the model of Sieber *et al.* .

Figure 5.4b) shows the spectral intensity of the fundamental as a function of time. By lining up the time-scales directly with the power measurements we can see the spectral components present at each point in the rise. The initial part of the spectral evolution is a rapid spectral condensation which was reported by Head et al. (2014) in CW-VECSEL lasing onset measurements as the cause of spectral evolution in early times after lasing onset before the steady-state was reached. As the spectrum narrows it moves towards a longer wavelength and forms a noise spike that starts saturating the SESAM. The spectral bandwidth of the laser is directly linked to the temporal width, and hence intensity, of noise-spikes present in the cavity (Siegman (1986)), we can assume that a certain degree of spectral condensation is required to form a noise-spike intense enough to begin the saturation process. The spectral condensation coincides temporally with the observed decrease in the measured fundamental intracavity power. The shift in laser wavelength and decrease in power indicates some damped spectral relaxation oscillation occurring prior to the mode-locking onset.

As the second harmonic begins to rise we see a separate spectral component forming the pulse present, similar to the process seen by Sarukura and Ishida (1992) in a mode-locked Ti:Sapphire. The shift in wavelength indicates that prior to saturating the SESAM, the gain peak was at a longer wavelength, where the loss introduced by the SESAM was lower. The gain peak for the saturated SESAM is at a shorter wavelength and remains constant over the course of the pulse evolution. As the pulse forms the CW part of the spectrum sees more loss and is attenuated over the course of many cavity round trips, until eventually the pulse spectrum reaches a steady-state and remains unchanging over subsequent round trips.

Figure 5.5 shows the spectrally resolved rise of the lasers as a function of incident pump power, which correspond sequentially to the pump powers given in table 5.3. We can see from the graphs that as we increase the pump power the initial CW component of the spectrum moves to longer wavelengths; consistent with the increasing local temperature of the active region. At a pump power between 800 and 894 mW, figure 5.5b) and 5.5c), we can see that the initial peak gain occur at the same wavelength as the final, saturated gain peak. It was noticeable from laser operation that the higher the pump power, and hence longer the CW-peak wavelength, the less stable the laser was in long term operation.

5.3.1 Noise Spike Dependence on Laser Bandwidth

As shown in figure 5.5 the time before the second harmonic signal is measured is dominated by the presence of a CW spectrum undergoing spectral condensation for all pump powers. The CW spectrum forms the noise spike that is used to initially saturate the SESAM, allowing a self reproducing pulse to build up in the cavity.

I have modelled the energy of the largest noise spike from the summation of longitudinal cavity modes given by equation 3.2, based on a gaussian spectrum with no fixed phase relation between each mode. The intracavity energy for the largest noise spike is calculated for an average output power of 20 mW and a 0.3% output coupler. The cavity repetition rate, and hence mode-spacing, was set to be 1 GHz. A saturation fluence of 10 $\mu J/cm^2$ and SESAM mode radius of 40 μm were used to calculated the saturation

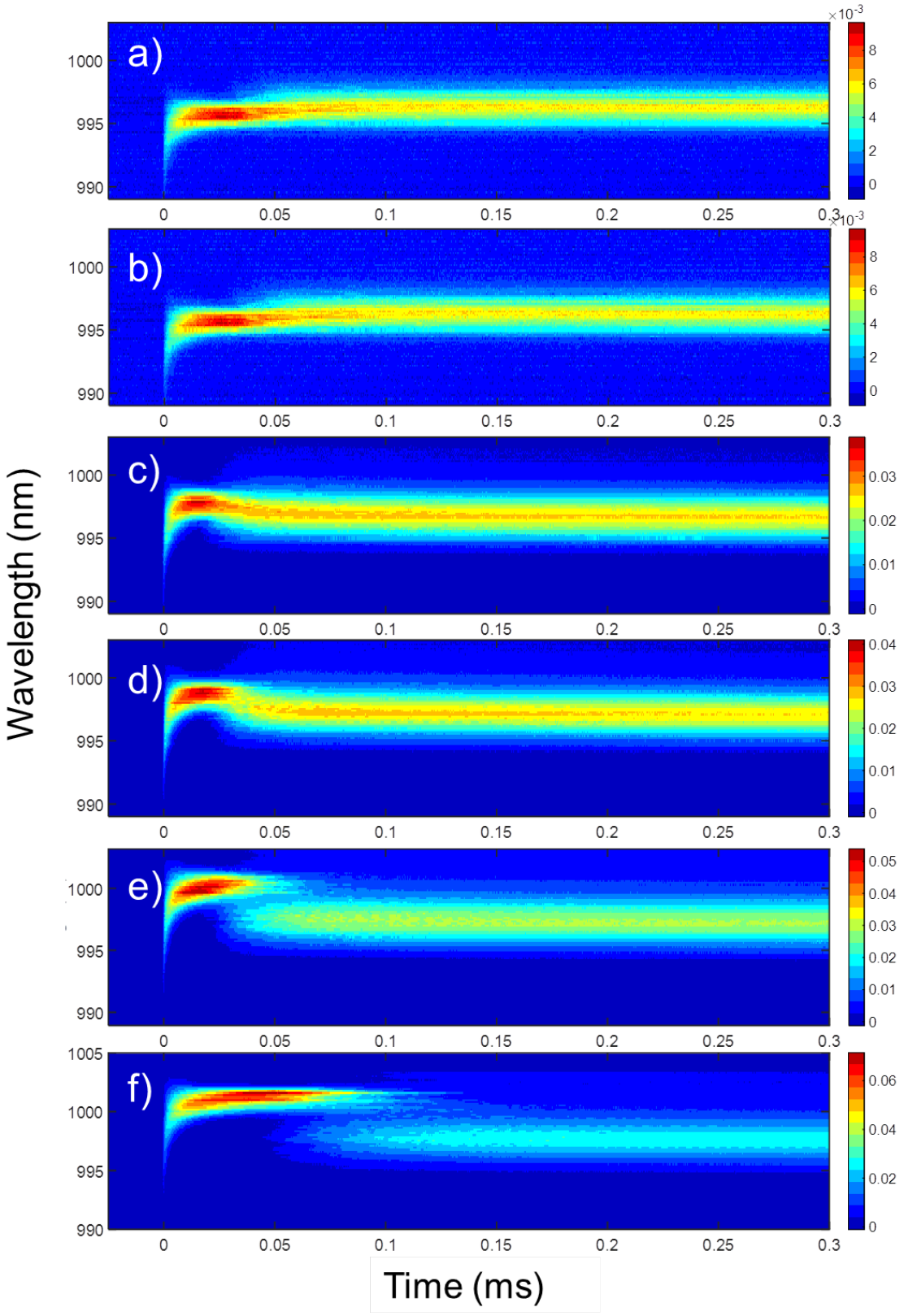

Figure 5.5: Spectral evolution of mode-locked VECSEL as a function of pump power. For incident pump powers of a) 705 mW, b) 800 mW, c) 894 mW, d) 990 mW, e) 1082 mW, and f) 1177 mW.

parameter. The model was performed over 100 simulations of the cavity due to the random nature of the cavity phases and noise spike formation. The laser parameters used approximately reflect those of the structure used in this experiment.

The noise spike energy and SESAM saturation parameter is shown as a function of FWHM spectral bandwidth in figure 5.6. An increase in spike energy, and hence saturation parameter is observed for a decrease in bandwidth. The increase in energy is, at first glance, counter intuitive as the temporal width of the noise spike is proportional to the reciprocal of the spectral bandwidth. Therefore broader spectrum results in a greater peak power. There is also an increase in peak power with increasing bandwidth due to the random walk nature of the summation of spectral modes; the peak power is proportional to the reciprocal of the square root of the number of cavity modes. However, with an greater bandwidth there are a more noise spikes circulating in the cavity due to the reduced temporal noise spike width, as a result the cavity energy is divided between more spikes. For a reduced bandwidth there are fewer, broader, more energetic spikes circulating in the cavity.

The spike energy increases from 0.03 nJ to 0.1 nJ and saturation parameter increases from 0.03 to 0.1 as the FWHM bandwidth decreases from 5 nm to 1 nm which is of the order of the reduction that is observed for the figures 5.5a) and b) before mode-locking onset. However, there is no well defined threshold for the saturation of the absorber required for the onset of mode-locking. Sieber et al. (2013) begin their model from a 10 nW noise floor and neglect any spectral considerations to reach a steady-state solution, which is smaller than the values I have extracted here. I have demonstrated here that there is a definite spectral component involved prior to the onset of mode-locking.

5.3.2 Mode-Locking Onset Times

Figure 5.7 shows the measured mode-locking onset time as a function of incident pump power. The onset times are more than 30 times greater than the theoretical values shown in figure 5.3. The mode-locking onset times do not show the trend given by equation 5.1 as the product of the intracavity power and the onset time should be constant. The first 3 pump powers give a constant value to within 10%, however, this relationship breaks

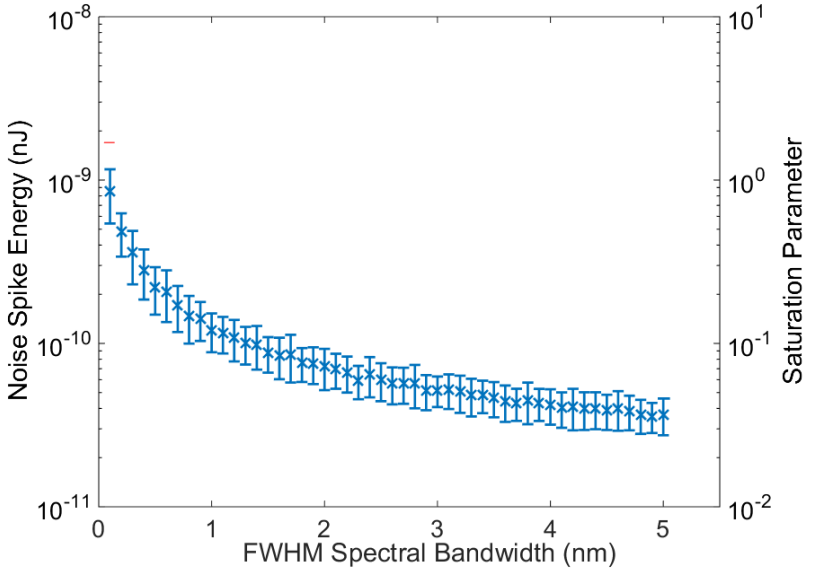

Figure 5.6: Simulated noise spike energy and saturation parameter as a function of FWHM spectral bandwidth

down for the final 3 pump powers. We can attribute this to the simplicity of the model used as it assumes all photons at the same wavelength and from figure 5.5 it has been shown that the initial formation of the pulse is dominated by a spectral condensation and relaxation process. As both the gain and the absorption, and consequently the saturation fluence, are dependent on wavelength it may be necessary to create a more sophisticated model of mode-locking onset that can take into account spectral mismatch between the gain and absorber wavelengths and relaxation dynamics. With a model of mode-locking onset time that matches the experimental data shown here it may be possible to extract macroscopic laser parameters under operation. However, further testing using ML-VECSELs with different cavity designs and gain-SESAM combinations must be tried to investigate if the dynamics observed here occur elsewhere.

5.3.3 Pulse Shortening per Round-Trip

The final parameter we are interested in is the rate of change of pulse duration after mode-locking onset. As shown in equation 5.4 by plotting the fundamental power rise squared and dividing by the second harmonic signal we obtain a plot proportional to the pulse duration at that time after onset, an example is shown in figure 5.8. By fitting

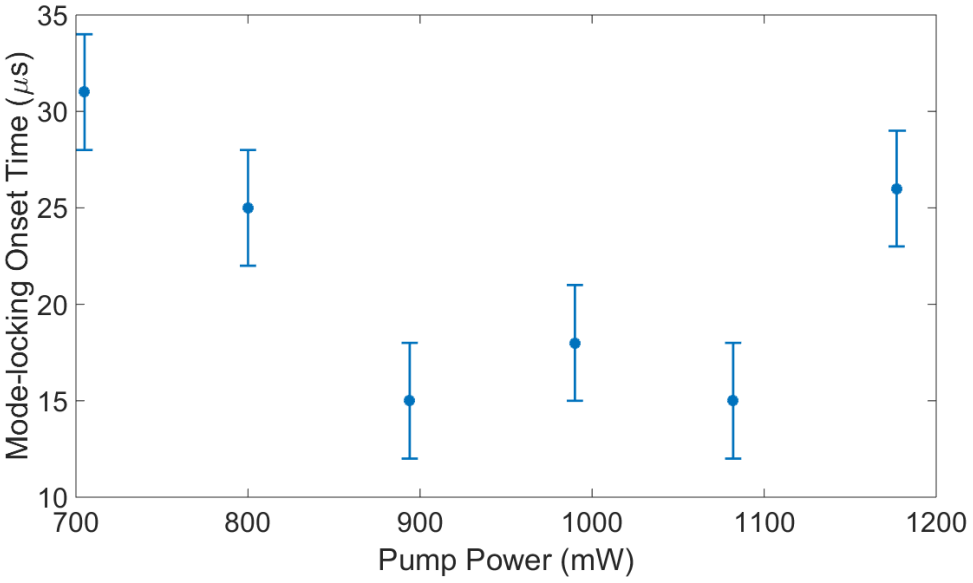

Figure 5.7: Measured mode-locking onset time as a function of incident pump power. The onset time is defined as the difference between initial fundamental and second harmonic signal measurements.

an exponential decay function we can obtain a value for the pulse shortening per round trip in the laser. The equation used to fit the data is:

$$Y_{signal}(T) = A_0 \left(1 + \epsilon_0 \cdot exp\left(-\frac{T - T_0}{T_{decay}}\right)\right), \tag{5.5}$$

where $Y_{signal}(T) \propto \tau(T)$ from equation 5.4, A_0 and ϵ_0 are fitting parameters and T_{decay} is the decay time given by the relationship:

$$T_{decay} = \frac{\tau_0 T_R}{S}. \tag{5.6}$$

τ_0 is the steady-state pulse duration and S is the pulse shortening per round trip (Wilcox et al. (2010b)).

The extracted pulse shortening for each value of pump power is given in table 5.3. Pump powers from 700 - 900 mW give an increase in pulse shortening per round trip from 0.011 fs to 0.040 fs. The more pump power incident on the structure, the hotter the local temperature and the broader the gain bandwidth, which results in a reduction

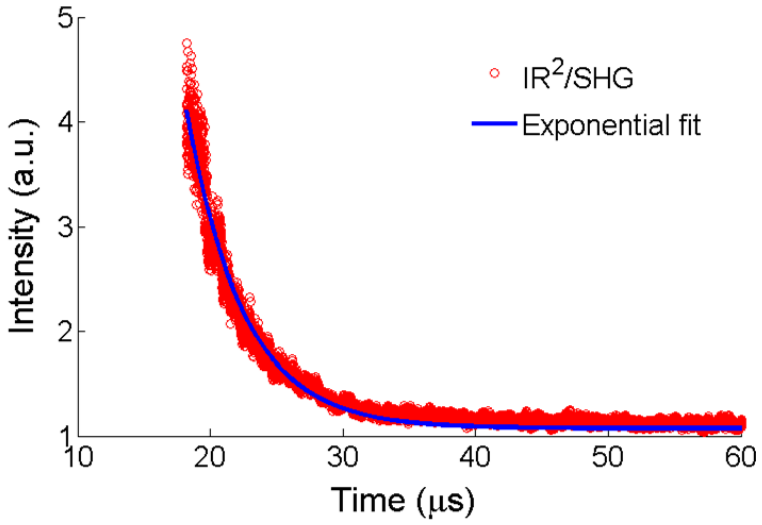

Figure 5.8: Graph showing an example of the evolution of the pulse as a function of the time after lasing onset. The IR^2/SHG is taken from the curves in figure 5.4a) and the exponential fit used is of the form given in equation 5.4.

of the filtering on the spectrum and a reduced lengthening of the pulse by the gain. For pump powers above 800 mW we can see an decrease in pulse shortening per round trip from 0.039 fs to 0.025 fs. The gain filtering effect on the pulse shaping will be weaker for higher pump powers and as such we would expect a larger net shortening per round trip.

Although with a higher intracavity power we have a larger fluence on the SESAM and hence greater saturation parameter which results in an absorber that is less strongly modulating the pulse; the wings of the pulse are enough to saturate the SESAM causing a reduction in the modulation effect. Pulse shortening as a function of the saturation parameter, S, on the SESAM is shown in figure 5.9, where the saturation parameter is calculated using an absorber F_{sat} of 10 $\mu J/cm^2$.

In spite of the reduced shortening by the SESAM at high intracavity fluences, a shorter pulse duration is reached in the steady-state due to broader available gain bandwidth and hence, reduced filtering, however, a longer time is required to reach the steady-state solution where effects from the gain and absorber are balanced. Of the two competing effects the absorber is dominant in the evolution of the pulse at high powers. However, it is very difficult to fully isolate one parameter to fully quantify any effect on pulse

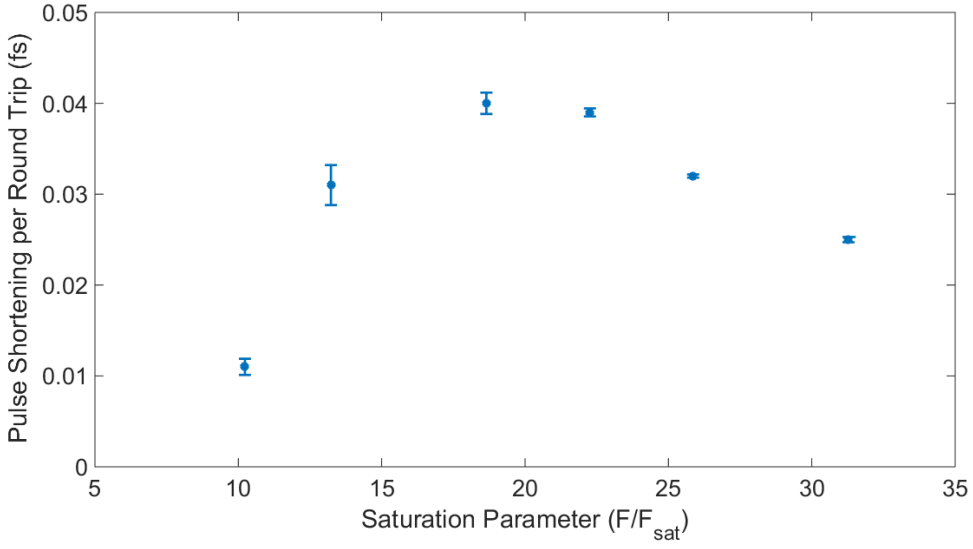

Figure 5.9: Calculated pulse shortening per round trip as a function of the SESAM saturation parameter. The SESAM parameter is calculated assuming a value of 10 $\mu J/cm^2$. The pulse shortening is extracted from the recorded fundamental and second harmonic power transients using equation 5.5.

formation and evolution due to the complex and inherently interlinked nature of the laser parameters.

I have neglected any pulse shortening or stretching due to dispersive effects in this analysis as due to the formed pulses being close to the transform limit and any pulse shaping effects over the course of a round trip to be small. As we approach the final steady-state bandwidth it can be assumed that per round trip the non-linear and linear dispersion are close to being balanced. As pulse durations decrease, and hence spectral bandwidths increase, dispersion will have a greater effect on the final steady-state pulse solution. Sarukura and Ishida (1992) showed that the introduction of a dispersion compensating prism pair into a passively mode-locked Ti:Sapphire reduced the onset time, reduced the pulse formation time, and increased laser stability. It would be interesting to perform an analysis of pulse formation using the experimental technique shown here combined with the dispersion analysis technique presented by Hoffmann et al. (2010) to resolve the effect of cavity dispersion on pulse formation.

The model developed for extracting the pulse-shortening per round trip does not assume monochromatic light. However, the presence of two distinct spectral components in the

Pump Power (mW)	Onset Time (μs)	Shortening per Round Trip (fs)
705	31 ± 3	0.011 ± 9×10^{-4}
800	25 ± 3	0.031 ± 2×10^{-3}
894	15 ± 3	0.040 ± 1×10^{-3}
990	18 ± 3	0.039 ± 4×10^{-4}
1082	15 ± 3	0.032 ± 2×10^{-4}
1177	26 ± 3	0.025 ± 3×10^{-4}

Table 5.3: Table containing the mode-locking onset times and extracted pulse shortening per round trip as a function of incident pump power. The pulse shortening is extracted from the recorded fundamental and second harmonic power transients using equation 5.5.

formation of the steady-state spectrum at the highest average powers indicates that not all of the measured fundamental power will be contributed to the pulse formation. It is difficult to separate the spectral components as there is not a clearly defined wavelength separation between the two components.

Measurement of the gain bandwidth through the method reported by Mangold et al. (2012) will allow measurement of the gain filter applied over a full range of incident pump powers and an indication of the magnitude of pulse lengthening from the gain contributed by the structures used in this experiment.

Implementation of a model based on macroscopic laser parameters which does not assume monochromatic light will be necessary to test the laser behaviour observed in this experiment.

5.4 Conclusions and Future Work

In this chapter I have demonstrated the first spectrally-resolved measurement of pulse formation in a ML-VECSEL alongside the measured fundamental and second harmonic power transients. The ML-VECSEL used exhibited stable mode-locking for pump powers from 700 - 1200 mW and the spectral rise and power transients were measured at steps of approximately 100 mW.

The measured power transients showed a initial rapid rise of the fundamental after the laser mode was uncovered. A small reduction in the intracavity power followed before rising to a steady-state value. The measured local minimum in the fundamental occurred at the same time as the initial measurement of the second harmonic. The measured second harmonic signal rose until reaching a steady-state value indicating no further evolution of the pulse was taking place.

The spectrally-resolved pulse formation showed for all pump powers a CW spectral component undergoing spectral condensation after lasing onset. The centre wavelength of the CW spectrum shifts to longer wavelength with increasing pump power. The spectral components of the pulse begin to form once the spectral condensation has narrowed the spectrum sufficiently. Whether the spectral condensation is required to form noise spikes of sufficient energy to begin bleaching the absorber or is an effect of greater magnitude than the weaker pulse shaping effects is unknown. However, it is clear that the spectral components associated with the final steady-state pulse spectrum do not begin to form until spectral condensation has occured. The presence of effects dependent on the laser spectrum in commencing mode-locked operation are not considered in any of the models used to predict ML-VECSEL behaviour. As a result it will be necessary to implement certain aspects of spectral dependence in future models developed.

From the fundamental and second harmonic power transients it was possible to extract a value for the pulse shortening per round trip as a function of the pump power and saturation parameter on the absorber. The pulse shortening initially increased for pump powers in the range 700 - 900 mW before decreasing again. More pump power increases the carrier density and local temperature, increasing the gain bandwidth. As a result the spectral filter is reduced and therefore there is less pulse stretching from the gain. As the pump power is increased there is an increase in intracavity power and hence saturation parameter on the SESAM. As a result at high pump powers there is a reduced shortening by the SESAM which serves to reduce the net shortening per round trip. As the structures had not been fully characterised it is not possible to suggest anything other than a purely phenomenological description of the effects that alter the pulse shortening. It will be necessary to extract macroscopic parameters of the structures under test

to establish the magnitude of pulse shortening from gain and SESAM interactions to validate the numbers extracted here.

From this small set of results it has not been possible to extract structure parameters under operating conditions due to the complex and interlinked nature of gain-absorber interactions. However, they have provided a clear phenomenological illustration of the mechanisms present in pulse formation in ML-VECSELs. Further experimentation will hopefully provide a way to disentangle as-yet unmeasured laser parameters.

In order to better understand the dynamics of mode-locking in VECSELs it will be necessary to perform the experiment detailed in this chapter over a greater number of ML-VECSELs. By applying this technique to different gain and absorber structures, and different cavity designs it will be possible to map out the full parameter space of macroscopic VECSEL parameters. Investigating different pulse durations and output powers will provide a route to determining mode-locking dynamics present as peak power increases, and as pulse durations near the de-phasing time-scales of the absorber.

Further modelling will be required to link what has been observed in the experimental data presented above to theories of pulse formation. Most models considered in this thesis have lacked any spectral dependence, resulting in assumptions made about the dynamic present. It will be necessary to consider spectral effects, such as the spectral profile of the SESAM absorption feature in further models constructed.

Overall, this technique has been demonstrated to be a powerful tool in resolving fundamental laser dynamics present in VECSELs. Further work is required to extract structure parameters under operating conditions. However, it has been used to develop a phenomenological understanding of pulse formation in ML-VECSELs.

Chapter 6

Experimental Results from "Short-Microcavity" Gain Structures

This chapter contains an account of the CW and mode-locked performance of VECSELs built from the new "short-microcavity" gain structure, W728, described in section 2.1.1.1. Initially the CW laser characteristics is compared to that of an existing 7.5λ/2 "long-microcavity" gain structure before moving on to describe the mode-locked results achieved. Next, I report on the mode-locked performance of a fully processed "flip-chip" structure, H28, provided by the University of Ulm.

ML-VECSELs with multi-Watt output powers have been limited to pulse durations longer than 400-fs (Scheller et al. (2012); Wilcox et al. (2013)) and sub-200 fs single-pulses have been limited to milliwatt average powers (Klopp et al. (2011)).

Klopp et al. (2011) used a processed "flip-chip" dielectric-AR-coated gain structure with 3 QWs. They reported pulse splitting as the limit of both pulse duration and output power from the ML-VECSEL. The semiconductor anti-resonant structures used in this work have a smaller LCF at the design wavelength than the dielectric-AR-coated structures and therefore have an increased gain saturation energy, allowing higher energy pulses to be supported in the cavity.

The work in this chapter describes the performance of ML-VECSELs constructed with the gain structures introduced in section 2.1.1.1. The "short-microcavity" structures were designed as a first investigation into the use of a shorter active region to broaden the gain bandwidth of a semiconductor anti-resonant gain structure to reduce pulse durations below sub-200 fs.

The gain structures in this chapter were sources from 2 groups. The unprocessed "short-microcavity" gain structure W728 was grown by I. Farrer at the University of Cambridge. Fully processed "flip-chip" structures designed for high-average output power mode-locked operation were provided by the group of Prof. P. Unger at the University of Ulm. H28, the structure used here was processed and soldered to a diamond submount by A. Hein.

6.1 Laser Performance Using "Short-Microcavity" Gain Structures

The design of W728 is described in section 2.1.1.1 and shown in figure 2.7. The active region was designed with the LCF minimum and QW emission set at 1000 nm. The structure was grown on a 500-μm thick GaAs substrate by MBE at Cambridge University and was unprocessed. The MBE reactors at Cambridge do not use phosphorous, therefore, it was not possible to include GaP strain compensation layers in the structure. The dark-line defects resulting from strain-induced relaxation will affect device performance. However, a pump spot with minimal number of dark-line defects can be chosen to reduce the loss.

6.1.1 CW Characterisation

The initial test of gain sample performance was to construct a straight cavity to measure CW average output powers and lasing spectra. W728 was attached to a copper heatsink with thermally conductive paint and then a 50-mm RoC 0.3% output coupler completed

the cavity. A fibre-coupled, 830-nm, 2-W diode laser was used to pump a 60-μm radius spot on the gain structure.

Figure 6.1 (a) shows the measured output power as a function of incident pump power and heat-sink temperature. The maximum power from the structure at 20 °C was approximately 185 mW at 1.1 W increasing up to approximately 270 mW for 1.25 W at -5 °C . The laser threshold was approximately 200 mW for all three heat-sink temperatures. An output coupling of 0.3% resulted in the best CW average output power; a reduction was observed for output couplers with a higher transmission. As a comparison, the "long-microcavity" gain structure V629 has a maximum output power of approximately 280 mW at 20 °C with 0.3% output coupling. The measured output power has been reduced in proportion to the number of QWs in the gain structure. Although there is a reduction in output power of W728, when compared with V629, as the purpose of the structure is for ultrafast operation, average power is a secondary concern.

Figure 6.1 shows the emission spectrum for three values of incident pump power with a heatsink temperature of 20 °C . It shows that at the maximum output power recorded in figure 6.1(a) the peak emission wavelength is approximately 1015 nm. In this wafer the measured QW photoluminescence peaked at 1015 nm, rather than the designed 1000 nm. The separation of the fringes observed in the emission spectra correspond to the FSR of a sub-cavity formed by the 500 μm thick substrate. Although the operating wavelength of W728 does not match the design wavelength, it is possible to use heat-sink temperature to tune the gain emission wavelength to spectrally overlap the absorption feature of a SESAM used for mode-locking.

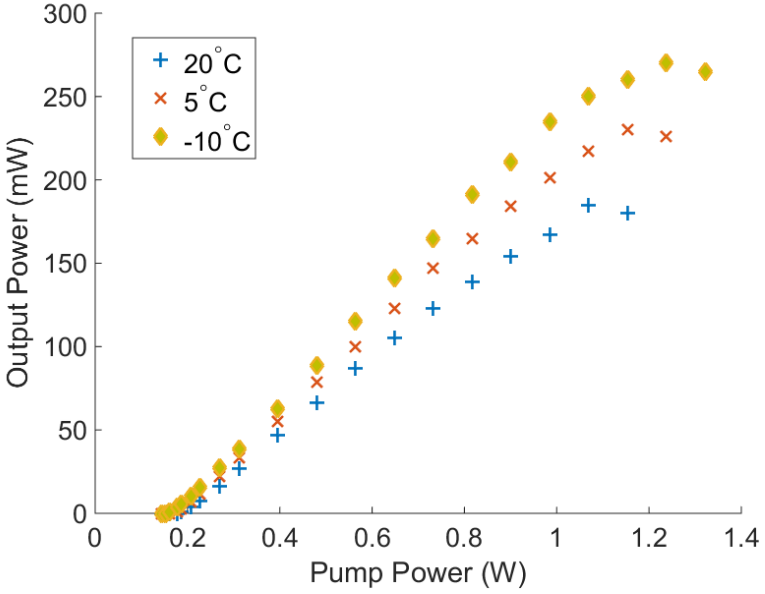

(a)

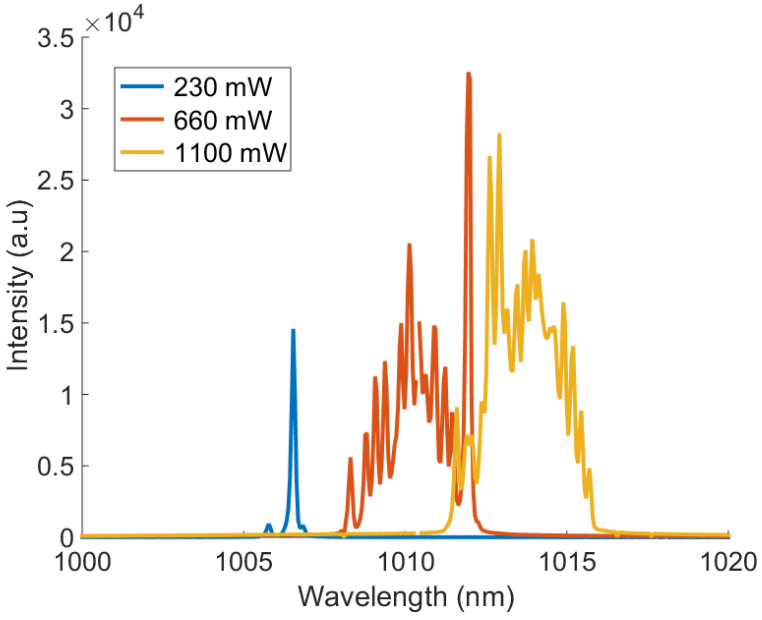

(b)

Figure 6.1: (a) Average output power as a function of incident pump power and heatsink temperature and (b) laser wavelength as a function of pump power for a CW-VECESL using the unprocessed "short-microcavity" gain structure and a 0.3% 50 mm RoC output coupler.

6.1.2 "Short-Microcavity" Mode-Locked Results

With an emission wavelength of approximately 1015 nm, the "short-microcavity" gain structures operated between the two wavelengths where existing gain samples and SESAMs work: 1000 nm and 1030 nm. Mode-locking of the "short-microcavity" structures was therefore attempted with both a 1000-nm and a 1030-nm SESAM. The 1000-nm SESAM, V628, used was the same reported in the previous chapter. The 1030-nm SESAM used was A4234, one of the structure characterised in chapter 4. It is important to note that the work performed here using W728 was completed prior to the characterisation detailed in chapter 4, and as a result some of the lasers were designed on the assumption that the SESAM modulation depth was 0.7% and without knowledge of the spectral profile of the absorption feature or the saturation fluence.

The laser cavity used here was a Z-cavity, of the type shown in figure 2.2, with the SESAM forming one end mirror of the cavity and a 0.15% output coupler forming the other. An output coupling of 0.15% was used, less than was applied in CW characterisation, in order to compensate for the introduction of saturable and non-saturable loss from the SESAM. The mode radius on the gain structure was 60 μm and a focusing fold mirror was used to set a mode radius on the SESAM of approximately 12 μm giving a mode-area ratio of approximately 25. Both gain structure and SESAM were mounted on water-cooled heatsinks with active temperature control provided by Peltier elements. The overall cavity length of 15 cm corresponded to a repetition of 1 GHz.

6.1.2.1 Mode-Locking with 1000-nm SESAM

The first attempt to mode-lock W728 structure was made with the V628. A CW laser output centred at 1015 nm was observed for the lowest temperature to which the gain heatsink could be cooled, -30 °C . In order to mode-lock the laser the SESAM had to be heated. For SESAM heatsink temperatures up to 70 °C CW lasing was still observed. As the SESAM heatsink temperature was increased above room temperature the threshold pump power of the laser increased and the output power decreased from

approximately 20 mW at room temperature down to 2 mW above 60 °C until the laser stopped operating for heatsink temperatures above 100 °C .

We assume that V628 has an absorption profile of similar shape to shown for V623 in figure 4.3(b), only displaced to a shorter wavelength by ≈30 nm as the design is the same. Heating tunes the absorption profiles of the SESAM to a longer wavelength, increasing the modulation depth seen by the laser. The temperature at which mode-locking occurred was where the effects from structure parameters such as gain, loss and dispersion balanced as discussed in chapter 3.

Single pulse mode-locking at an average output power of 2 mW was achieved for a gain heatsink temperature of -23 °C and a SESAM heatsink temperature of 85 °C and an incident pump power of 1 W. Figure 6.2 shows an example of the optical spectrum and intensity autocorrelation of the observed pulses. With a FWHM spectral bandwidth of 6.2 nm and a FWHM pulse length of 205 fs the pulses were 1.3 times transform limited. The long wavelength feature present in the spectrum has been observed in other ML-VECSELs with pulse durations on the order of, or below, 200-fs (Klopp et al. (2009, 2011); Quarterman et al. (2009)). As the autocorrelation was pedestal free the components of the long wavelength feature are assumed to contribute to the pulse. The mode-locked laser was unstable, with a pulse train visible for less than 30 seconds making it not possible to measure an RF spectrum and hence determine the repetition rate precisely. The average power and approximate repetition rate correspond to a pulse energy of 2 pJ and a peak power of 8.6 W.

The lack of stability observed in this laser could be attributed to the broad gain bandwidth of the sample, which allowed operation at wavelengths where values of GDD and modulation depth did not support stable mode-locked operation. At the highest pump powers, above 1.4 W, the laser would cease unstable mode-locked operation and jump to a longer wavelength of 1015 nm in CW operation.

The ability for the laser to operate with a mode-locked spectrum centred at 986 nm and 1015 nm in CW operation indicates a gain structure with a >29 nm gain bandwidth. Overall, in spite of the large temperature difference required to force overlap of the gain and SESAM operating wavelength, and the subsequent reduction in output power,

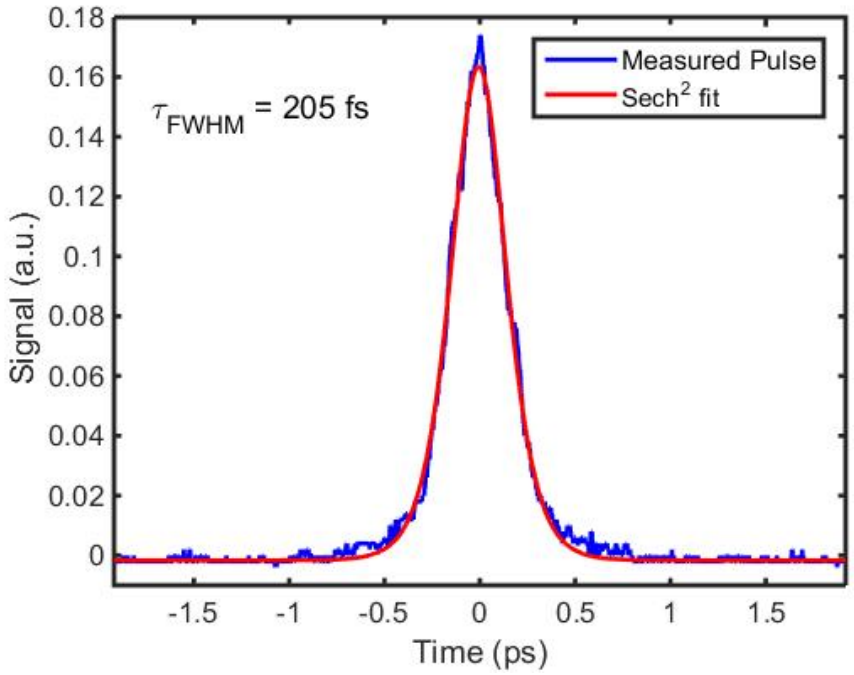

(a)

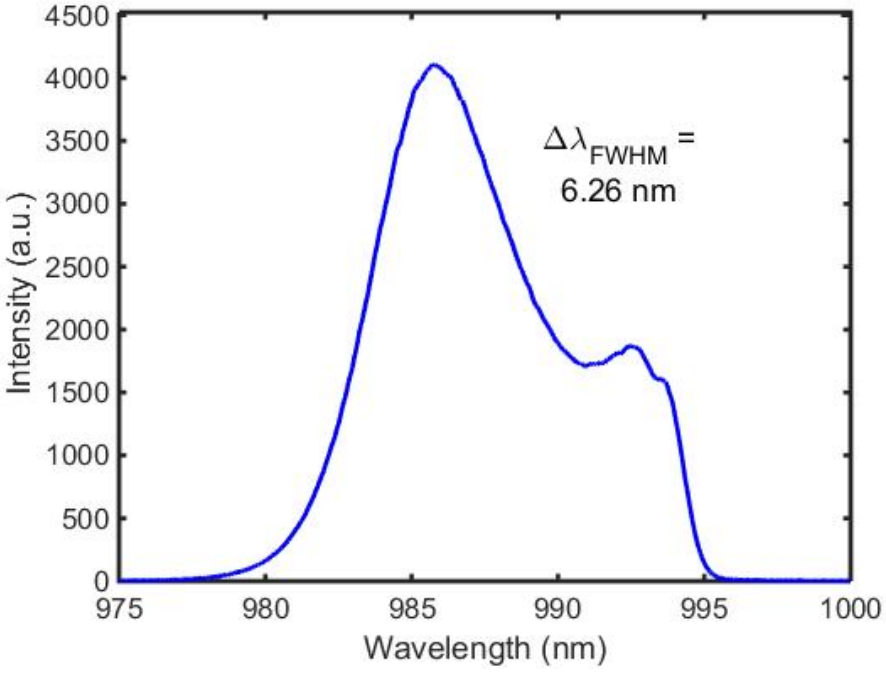

(b)

Figure 6.2: Example of mode-locked results using the 1000 nm SESAM. Figure (a) shows the autocorrelation of the pulse with a sech^2 fit giving a pulse length of 205 fs. Figure (b) shows the spectrum associated with the pulse, centred on 987 nm with a FWHM bandwidth of 6.2 nm.

the measurement of 200-fs pulses with 1.3 times transform limited indicate that the overall gain design is suitable to generation of pulses approximately 150 fs in duration if transform limited. Regrowth of the gain sample with the QWs centred at the correct wavelength would be required to further test device performance.

6.1.2.2 Mode-Locking with 1030-nm SESAM

To avoid the loss incurred by heating the SESAM we switched to a second saturable absorber structure designed for 1030 nm; A4234 as described in chapter 4. With A4234 in the cavity and the gain structure heatsink at room temperature it was not possible to achieve lasing. Cooling of the gain structure was found to be necessary to overcome the insertion loss of the SESAM. The laser cavity was identical to the one used with the 1000 nm SESAM.

With both the gain and the SESAM heatsink temperatures set to -12 °C single-pulse mode-locked operation was observed with an output power of 13 mW, though still with limited stability. Figure 6.3 shows the autocorrelation and optical spectrum of the mode-locked output. 260 fs pulses were observed with a spectral bandwidth of 8 nm leading to pulses that are 2 times transform limited. A long wavelength feature is present in the optical spectrum, similar to the one observed in the spectrum using V628. It is unclear whether the spectral feature contributes to the pulse, or is a CW component, however the presence of a pedestal free autocorrelation indicates the former.

The centre of the spectrum lay at 996 nm, which from the reflectivity measurements in chapter 4 is approximately 20 nm from the centre of the absorption of the cooled SESAM. The broadband reflectivity of A4234, shown in figure 4.3, indicates that there was still saturable absorption of approximately 1% at 996 nm. As both gain and SESAM are operating far from design wavelength the GDD contribution is a likely source of phase structure on the pulse leading to the large time bandwidth product.

Using a 1030-nm SESAM rather than the 1000-nm SESAM has, therefore, resulted in a 6-fold increase in output power, to 13-mW which, at the 1 GHz pulse repetition frequency, corresponds to a pulse energy of 13 pJ and peak power of 50 W. Although

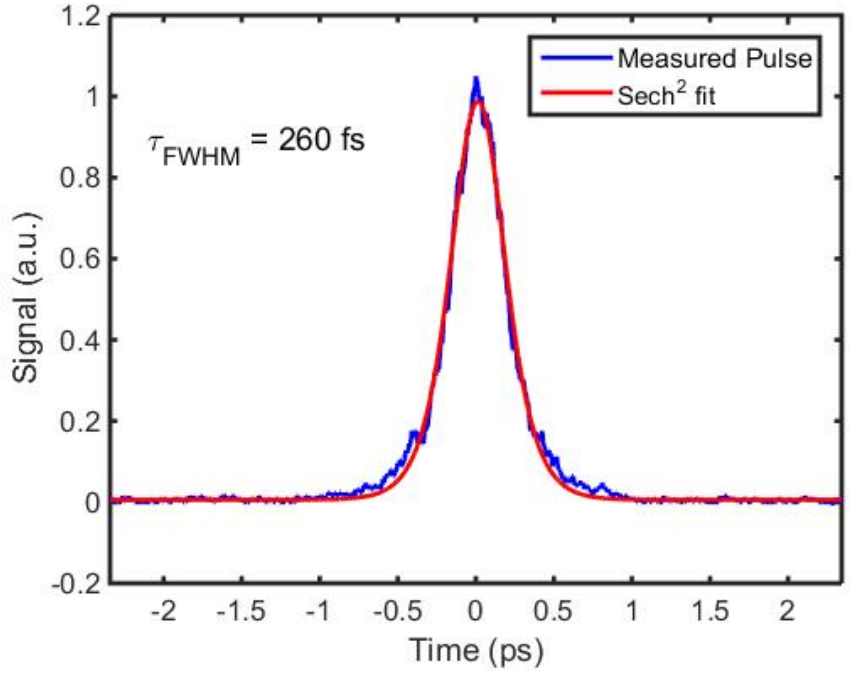

(a)

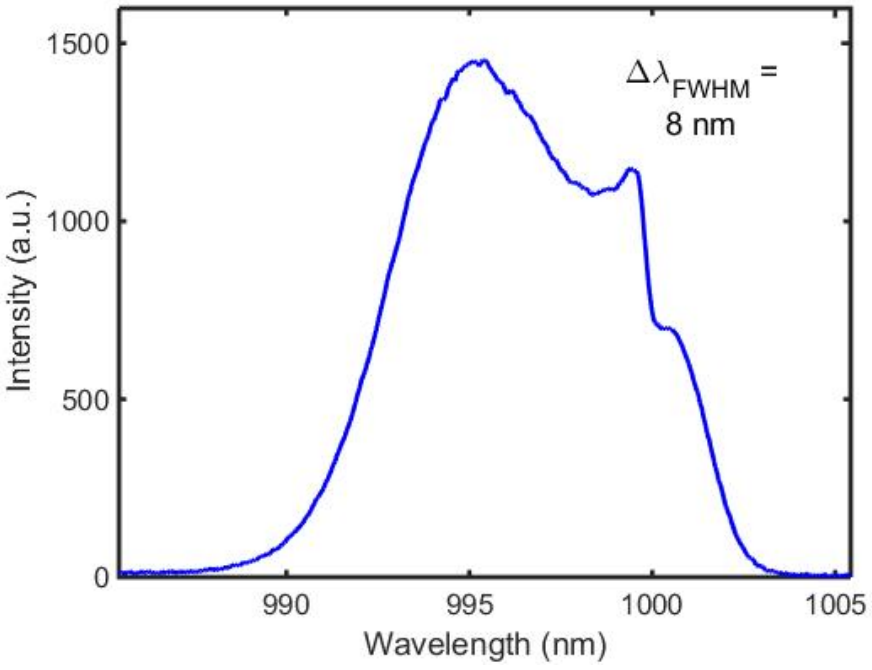

(b)

Figure 6.3: Example of mode-locked results using the 1030 nm SESAM. Figure (a) shows the autocorrelation of the pulse with a sech^2 fit giving a pulse length of 260 fs. Figure (b) shows the spectrum associated with the pulse, centred on 996 nm with a FWHM bandwidth of 8 nm.

the pulse duration was increased to 260-fs, the increase in spectral bandwidth indicates that much shorter pulse, ≈ 130 fs, could be supported if the net cavity dispersion were to be corrected.

Overall, in-spite of the incorrect QW operating wavelength, the initial test of using a "short-microcavity" structure was promising showing a greater laser bandwidth than had been shown by any previous structure used in single-pulsed operation. Regrowths of the structures were pursued to correct the QW wavelength, however, subsequent samples exhibited much reduced output power in CW operation and as a result mode-locking was not possible. Technical problems with the MBE growth machines at Cambridge resulted in further growth being unavailable for a considerable period of time.

6.2 "Flip-Chip" Structure for High Power

As discussed in section 2.2 it is possible to use substrate removal to increase heat extraction from the active region of a VECSEL gain structure to access higher output powers. Through collaboration with Prof. Unger's VECSEL group at the University of Ulm, fully processed "flip-chip" gain structures have been made available. The gain sample, H28, reported here was processed and soldered to high-conductivity diamond submounts by A. Hein. The access to fully processed samples allow investigation of "short-microcavity" gain structures designed for accessing higher average mode-locked output powers.

6.2.1 "Flip-Chip" Gain Structure Design

Figure 6.4 shows a schematic of the fully-processed, dielectric-AR coated structure used here. The active region was designed to be resonant with a length of 6λ/2 containing 8, 7-nm InGaAs QWs. Two QWs were situated at each anti-node of the electric field and were spaced by 20-nm of bulk GaAs. GaP layers were included in the structure for strain compensation. 220-nm of $Al_{0.3}Ga_{0.7}As$ capped the semiconductor active region, giving resonant enhancement at the design wavelength. The active region was grown on a 27.5 layer-pair $Al_{0.15}Ga_{0.85}As$/GaAs DBR. 160-nm Al_2O_3 was deposited on the gain

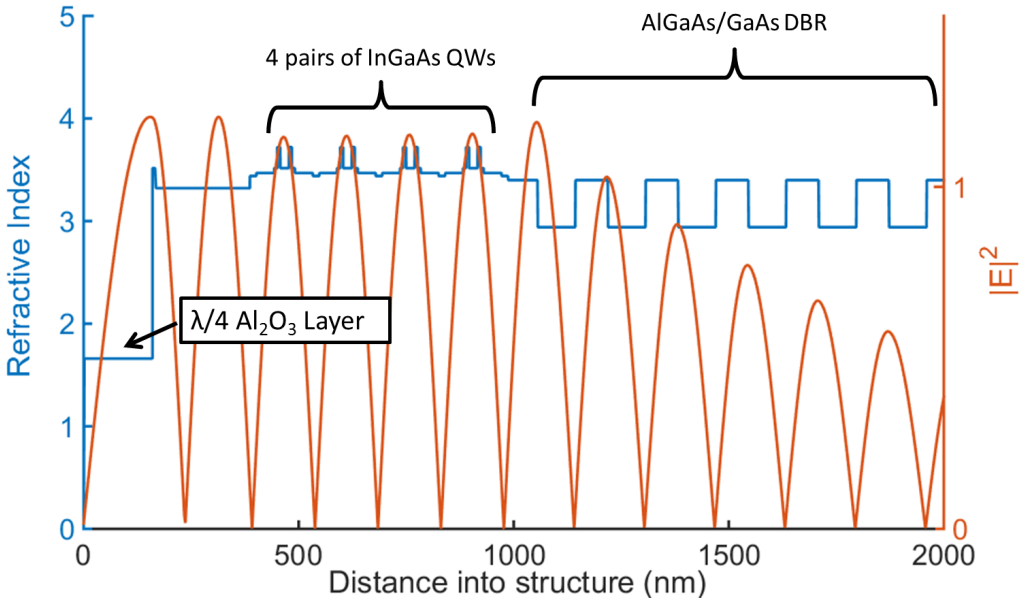

Figure 6.4: Schematic of a "flip-chip" gain structure. The active region is a $6\lambda/2$ resonant structure containing 4 pairs of 7-nm thick InGaAs QWs situated at the anti-node of the electric field. The QWs at each anti-node are separated by 20-nm of bulk GaAs. GaP strain compensation layers are placed between each QW pair. The active region is grown on a 27.5 layer-pair $Al_{0.15}Ga_{0.85}As$/GaAs DBR. The structure is capped by a 160-nm Al_2O_3 layer.

structure; the dielectric coating is used to broaden the LCF and smooth the GDD profile (Hein et al. (2012)). The LCF and GDD profile of the structure is shown in figure 6.5. The GDD has very little variation and is close to zero around the design wavelength.

Including 2 QWs at each anti-node is only possible with structures processed for thermal management as the required pump intensity to reach transparency would be sufficiently high to cause local temperature induced loss effects to dominate before lasing occurred. In a processed structure the inclusion of more QWs, compared the previous "short-microcavity" structures used above, will provide more gain, allowing higher output powers to be reached. These structures demonstrate the first test of the thermally managed gain samples from Ulm University..

6.2.2 Mode-Locked Performance of "Flip-Chip" Structures

Gain structures of the above design were provided with design wavelengths of 1010 nm and 1030 nm. Due to wavelength mismatch with the SESAM no stable mode-locking was

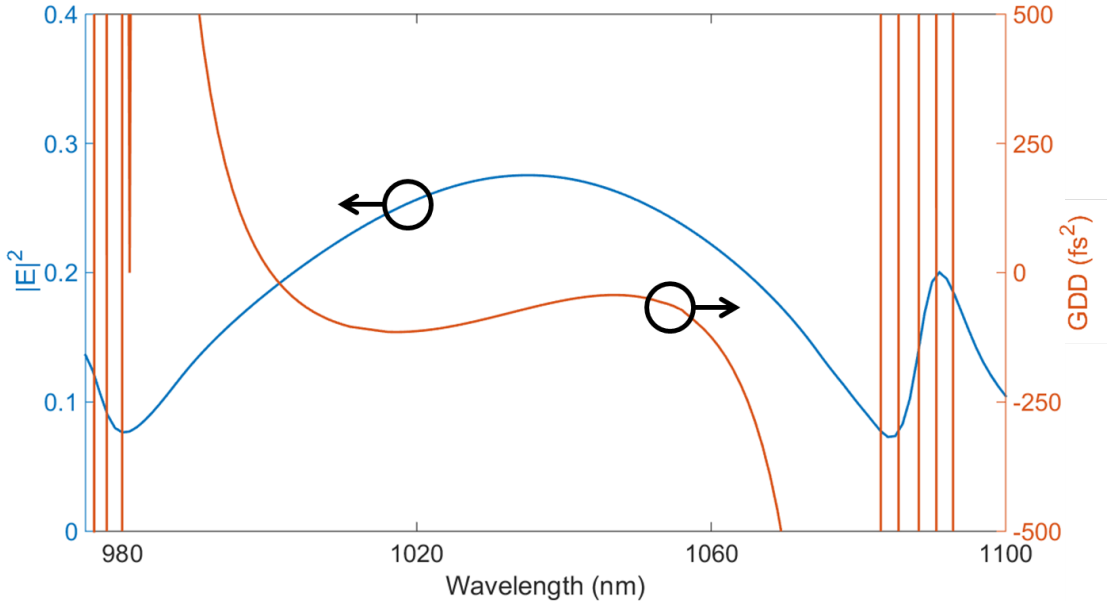

Figure 6.5: Shows the LCF (blue) and GDD (orange) as a function of wavelength for the sample design described in figure 6.4.

observed for the 1010-nm structure. This section will detail experimental mode-locked results from the 1030nm gain structure, H28.

The laser constructed was a V-cavity configuration with a SESAM forming one cavity-end mirror and a 1.45% 100-mm RoC output coupler forming the other. The gain was situated in the middle of the cavity. The overall cavity length was 9.4 cm corresponding to a repetition rate of 1.6 GHz. The heat-sink temperatures were set to be 15 °C for the gain and 0 °C for the SESAM. A 30-W fibre-coupled 808-nm diode laser was used to pump a spot with radius of approximately 200 μm on the gain. The mode-radius on the SESAM was approximately 100 μm, giving a mode-area ratio of 4.

The SESAM used in this laser was V623, one of the absorbers characterised in chapter 4. Through characterisation V623 was discovered to have the macroscopic properties suited best to the pursuit of a high-power ML-VECSEL, with the lowest F_{sat}, highest modulation depth. The centre of the absorption dip was 1030-nm which matched well to the operating wavelength of H26.

The gain structure was found to have a maximum average output power of 5.2 W for 30 W of incident pump power in CW operation, with a highly-reflective cavity mirror

replacing the SESAM.

Figure 6.6 shows the measured autocorrelation and spectrum from the laser described above. The extracted FWHM pulse duration was 193 fs with an 11.8-nm spectral width, resulting in a pulse that was approximately 2.1 times transform limited. The long wavelengths shoulder in the spectrum contributes to the measured FWHM spectral width for this laser, however, the measurement of a pedestal-free autocorrelation indicates that the full spectrum contributes to the pulse.

The average output power was initially measured to be 400 mW before decreasing over the course of several minutes and reaching a steady state of 200 mW. The reduction in output power is attributed to heating of the SESAM causing increased loss. In CW operation with a HR in place of the SESAM, no power reduction as a function of time was observed. At an average power of 400 mW the peak output power of the laser was approximately 1 KW.

The large transform limit of the optical pulses indicates that phase structure, probably arising from net cavity dispersion, has extended the duration of the pulse. The gain structure was designed with close to zero dispersion, although slightly negative at -70 fs^2. As mentioned in section 4.1, V623 is a SESAM designed for operation at 1000 nm that operates at 1030 nm. As can be seen in figure 2.12, at a point 30 nm above the design wavelength the GDD is approximately -500 fs^2. For a pulse duration of 92 fs, assuming a gaussian pulse profile, a net GDD of -500 fs^2 will cause a pulse lengthening of approximately 1.2 fs per pulse-absorber interaction. The 1.2 fs pulse stretching per round trip is large compared to the weak, ≈ 0.05 fs, pulse shaping that occurs per round trip that was reported in section 5.3.3. The stretching contribution from the GDD is sufficient, over many thousands of round trips, to cause the pulse lengthening shown here. It will be necessary for the next designs of both gain and absorber structures to ensure that net dispersion is minimised in the cavity, whilst maintaining the device performance exhibited here.

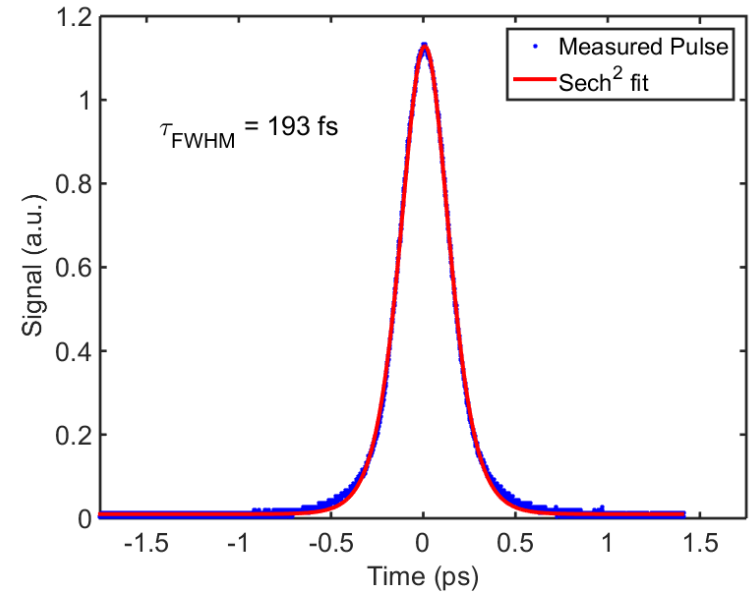

(a)

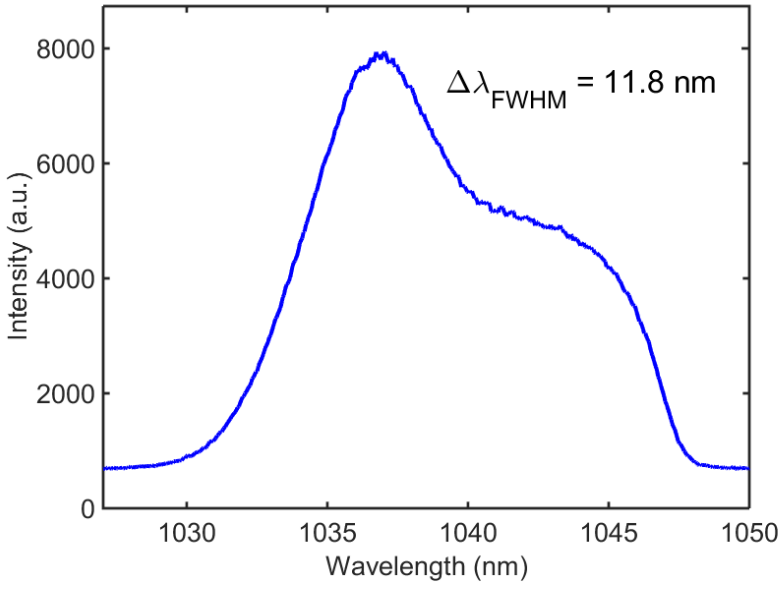

(b)

Figure 6.6: (a) Autocorrelation and (b) optical spectrum of the mode-locked VECSEL using the gain structure shown in 6.4 and V623. The extracted FWHM pulse duration was 193 fs and the FWHM optical bandwidth was 11.8 nm.

6.3 Conclusions and Future Work

In this chapter I have demonstrated the first mode-locked results from new "short-microcavity" gain structures. The 4.5λ/2 gain structures contained 4 QWs and were designed for 1000 nm grown by MBE at Cambridge University. However, due to mis-calibration of the indium concentration in the QWs the lasing wavelength was approximately 1015 nm. Mode-locking was achieved by temperature tuning the operating wavelength to overlap with the SESAM wavelength. Attempts were made with two absorbers, one designed for 1000 nm and one for 1030 nm.

Using the 1000-nm absorber, 205 fs pulses were observed with a spectral bandwidth of 6.2 nm centred at 986 nm, giving pulses that were 1.3 time transform limited. The output power was limited to 2 mW due to the large SESAM heat-sink temperature required. When the laser dropped out of mode-locked operation it returned to CW lasing at 1015 nm. Overall, the large wavelength jump indicates a structure with a very large intrinsic gain bandwidth.

The 1030-nm SESAM yielded 260-fs pulses with a laser bandwidth of 8 nm, resulting in pulses twice transform limited. The 996 nm central wavelength was approximately 20 nm from the design of the SESAM and, as a result, there was significant dispersion contribution from the absorber. Although the pulses were longer, the broader laser bandwidth indicated gain structures of a similar design would support sub 150 fs pulses. The increased output power indicates that the gain can support higher energy pulses than dielectric-AR coated gain structures.

Through collaboration with the University of Ulm, gain structures processed for improved thermal management were investigated. The gain samples were designed as a first attempt at performing high-power mode-locking and consisted of a 6λ/2 active region with 4 pairs of QWs at the electric field anti-notes. The structure was capped by a dielectric-AR Al_2O_3 layer. The gain structure was mode-locked with V623, the SESAM identified by the characterisation work in chapter 4 as the best suited for high-power operation at 1030 nm.

The measured pulses had a FWHM duration of 193 fs and a FWHM spectral bandwidth of 11.8 nm. The pulses were approximately two times transform limited. The average output power was initially 400 mW before decaying to a steady-state value of 200 mW. The reduction of laser performance was due to thermally induced loss in the SESAM. At the average power of 400 mW the peak power was 1 KW, representing the first result KW-level peak power from a ML-VECSEL with a sub-200 fs pulse duration.

In order to reduce thermal effects, improved heat extraction from the absorber must be implemented in further structure designs. The surface-recombination design makes substrate removal difficult to implement due to the need to stop the etch on the 2-nm GaAs capping layer. Use of an intracavity heat-spreader may be preferable, however, dispersion, loss, and spectral filtering from the inserted material must be taken into account.

The prevalence of chirped pulses shown in this chapter means that better characterisation of optical pulses is required. Frequency-resolved-optical grating (FROG) measurements will allow the extraction of the spectral phase across the optical spectrum allowing analysis of the dispersion properties of the laser cavity.

Further structure designs will be pursued to optimize net cavity dispersion through contributions from gain and absorber. It has been made clear from the work presented here that the use of absorbers not carefully designed to spectrally match the gain structures used has led to pulses with large transform limits or limited stability. Future designs will also compare the performance between dielectric-AR coated and semiconductor anti-resonant structures optimised for high-power operation.

It will also be necessary to perform characterisation of gain structures, as reported by Mangold et al. (2012), to provide full comparison of the effect of altering design parameters. Optimisation of gain structure designs will be necessary to pursue pulse durations towards 100-fs.

Overall, the structures used here have shown promise for the realisation of a Watt-level ML-VECSEL with pulse durations below 200-fs. Although, further structure designs and full characterisation will be required to reach that goal.

Chapter 7

Conclusions

The work presented in this thesis has demonstrated use of characterisation techniques and design of structures to realise high-power ultrafast ML-VECSELs, and represents a significant advance in reaching the device performance required for ML-VECSELs to be a practical source for applications.

An investigation into characterising the macroscopic structure parameters of three surface-recombination SESAMs was performed. Extracted values of saturation fluence were on the order of 10 $\mu J/cm^2$, five times less than "low-modulation depth" designs initially characterised by R. Grange in 2005. The reduction in saturation fluence allowed the mode-area ratio constraints to be relaxed for mode-locked operation. As a result, I have demonstrated a ML-VECSEL with a 2:1 mode-area ratio between gain and SESAM; the smallest reported mode-area ratio using a surface-recombination SESAM. A low-area ratio is useful to avoid thermally induced damage as VECSEL performance is scaled to high average output powers.

The modulation depths of the SESAMs under investigation was reported by Wilcox et al. (2008) to be 0.7%, however, when measured was determined to be >2% for all three structures. The measured modulation depth and saturation fluence coincide with the values reported by Sieber et al. (2013) for the development of a 1-W 200-fs ML-VECSEL. As a result the surface-recombination SESAMs characterised seem well suited to the development of a high-power ultrafast ML-VECSEL. The response time of the

absorbers was measured to be less than 10 ps, with the measurement resolution limited by the temporal width of the pump and probe pulse used. A response time of this magnitude means the absorbers will be well suited to mode-locked operation at very high GHz repetition rates.

I have demonstrated for the first time spectrally-resolved pulse formation in ML-VECSELs. The measurements of the fundamental and second harmonic power transients alongside the fundamental spectral evolution has allowed us to establish a phenomenological model of pulse formation. The detection of a CW spectral component dominating the pulse formation in early times after lasing onset has lead us to the conclusion that the assumption of monochromatic light made by current predictive models is insufficient to simulate real-world mode-locking dynamics. Further experiments will be required to investigate pulse formation over a range of powers, pulse durations, and structure designs. It was not possible to extract laser parameters under operating conditions due to the complex and interlinked nature of gain-absorber interactions. As a result, more sophisticated modelling and fully characterised structures will be required to consolidate the experimental results acquired here with theories of pulse formation.

The mode-locked performance of new gain structure designs has also been presented. A $4.5\lambda/2$ "short-microcavity" gain structure grown at the university of Cambridge was investigated as a route towards sub-200 fs pulse duration with higher pulse energy than reported in literature at the time. Growth errors caused the laser to operate at a wavelength 15 nm longer than the design wavelength. A FWHM pulse duration of 205 fs was achieved using a SESAM designed for 1000-nm with 3 mW of average output power. 260-fs pulses that were twice transform limited were obtained using a SESAM designed for 1030 nm with an increased power of 13 mW. Although sub-200 fs operation was not achieved the broad laser bandwidth of the 260-fs pulses suggested that shorter pulses could be supported with correct structure growth.

Processed gain structures designed for high-power ultrafast operation were provided by the University of Ulm. When mode-locked, 193-fs pulses with initially 400 mW average power were achieved. The average power after mode-locking onset decayed to a steady-state 200 mW over a minute long timescale. The decay in output power is attributed

to the heating of the SESAM, and as a result it will be necessary to implement thermal management of the absorber structures. At 400 mW the laser had a peak power of 1 KW, which is the highest peak power reported to date for a laser with sub-200 fs pulse duration.

7.1 Future Work

In order to reach the, rather strict, requirements on laser performance for ML-VECSELs to be a competitive source, particularly for the generation of coherent octave-spanning supercontinuum, certain aspects must be improved upon. Although this work has demonstrated significant advances in performance at sub-200 fs pulse durations, improvements in average power and pulse duration are still required.

One of the limits in average output power seen in this work was thermally induced loss in the absorber structures. Processing of surface-recombination SESAMs presents a difficult technological challenge as any wet-chemical etching must stop on the 2-nm capping layer or risk seriously affecting device performance. Characterisation of the surface-recombination SESAM structures has shown that they are well suited to high-power ultrafast performance, although further structure designs will be investigated to further optimise the macroscopic parameters, for example the use of dielectric coatings to smooth the dispersion profile.

The gain structures used in this thesis have demonstrated a sufficient gain bandwidth to support pulses approaching 100-fs in pulse duration. Full characterisation of the gain structures will be required to make informed decisions about further structure designs. Of particular interest is the magnitude of gain saturation energy, which has not been measured for semiconductor anti-resonant structures, and is known to be a limiting factor in the pursuit of high average power ML-VECSELs.

Improved characterisation of the structures will allow the pulse formation dynamics that I have observed in this thesis to be fully investigated. Known parameters will allow a full exploration of the effect of macroscopic laser parameters on the ML-VECSEL output and the overall laser stability. It will also be possible to investigate the presence of

any fast-recombination pulse shaping effects present in the formation of pulses using high-power ultrafast ML-VECSELs; effects that have been theorised to exist but never experimentally verified.

Although current ML-VECSEL performance does not meet the strict requirements for supercontinuum generation, it is now sufficient for other applications. One of interest is providing a compact source for broadband THz radiation. An initial report by Mihoubi et al. (2008) demonstrated a ML-VECSEL capable of driving only the generation scheme of a THz-time-domain-setup (THz-TDS). With recent advances in peak output power a compact THz-TDS with detection and generation driven by a tunable repetition-rate VECSEL employing optical sampling by cavity tuning (OSCAT) (Hochrein et al. (2010)) as the variable delay line.

References

Govind P. Agrawal and Charles M. Bowden. Concept of linewidth enhancement factor in semiconductor lasers. Its usefulness and limitations. *IEEE Photonics Technology Letters*, 5(6):640–642, 1993.

A.G. Baca and C.I.H. Ashby. *Fabrication of GaAs devices*. 2005.

M E Barnes, Z Mihoubi, K G Wilcox, a H Quarterman, I Farrer, D a Ritchie, a Garnache, S Hoogland, V Apostolopoulos, and a C Tropper. Gain bandwidth characterization of surface-emitting quantum well laser gain structures for femtosecond operation. *Optics express*, 18(20):21330–41, September 2010.

I Barycka and I Zubel. Chemical etching of (100) GaAs in a sulphuric acid-hydrogen peroxide-water system. *Journal of Materials Science*, 22:1299–1304, 1987.

R. Bek, H. Kahle, T. Schwarzbäck, M. Jetter, and P. Michler. Mode-locked red-emitting semiconductor disk laser with sub-250 fs pulses. *Applied Physics Letters*, 103(24): 2011–2015, 2013.

Carl Borgentun, Jörgen Bengtsson, and Anders Larsson. Direct measurement of the spectral reflectance of OP-SDL gain elements under optical pumping. *Optics express*, 19(18):16890–7, August 2011.

T. Brabec, Ch. Spielmann, P. F. Curley, and F. Krausz. Kerr lens mode locking. *Opt. Lett.*, 17(18):1292–1294, Sep 1992.

O. Casel, D. Woll, M. a. Tremont, H. Fuchs, R. Wallenstein, E. Gerster, P. Unger, M. Zorn, and M. Weyers. Blue 489-nm picosecond pulses generated by intracavity

frequency doubling in a passively mode-locked optically pumped semiconductor disk laser. *Applied Physics B*, 81(4):443–446, July 2005.

Y. F. Chen, Y. C. Lee, H. C. Liang, K. Y. Lin, K. W. Su, and K. F. Huang. Femtosecond high-power spontaneous mode-locked operation in vertical-external cavity surface-emitting laser with gigahertz oscillation. *Optics Letters*, 36(23):4581, 2011.

Alexej Chernikov, Jens Herrmann, Martin Koch, Bernardette Kunert, Wolfgang Stolz, Sangam Chatterjee, Stephan W. Koch, Tsuei Lian Wang, Yushi Kaneda, J. Michael Yarborough, Jörg Hader, and Jerome V. Moloney. Heat management in high-power vertical-external-cavity surface-emitting lasers. *IEEE Journal on Selected Topics in Quantum Electronics*, 17(6):1772–1778, 2011.

A.R Clawson. Guide to references on IIIV semiconductor chemical etching. *Materials Science and Engineering: R: Reports*, 31(1-6):1–438, January 2001.

Coherent Inc. Verdi G Series.

L.A. Coldren and S.W. Corzine. *Diode lasers and photonic integrated circuits*. Wiley Series in Microwave and Optical Engineering. Wiley, 2005.

Scott W. Corzine, Randall S. Geels, Jeff W. Scott, Ran Hong Yan, and Larry a. Coldren. Design of Fabry-Perot surface-emitting lasers with a periodic gain structure. *IEEE Journal of Quantum Electronics*, 25(6):1513–1524, 1989.

R Fleischhaker, N Krauss, F Schättiger, and T Dekorsy. Consistent characterization of semiconductor saturable absorber mirrors with single-pulse and pump-probe spectroscopy. *Optics express*, 21(6):6764–76, March 2013.

Mahmoud Gaafar, Philipp Richter, Hakan Keskin, Christoph Möller, Matthias Wichmann, Wolfgang Stolz, Arash Rahimi-Iman, and Martin Koch. Self-mode-locking semiconductor disk laser. *Optics express*, 22(23):28390–9, November 2014.

A. Garnache, S. Hoogland, A. C. Tropper, I. Sagnes, G. Saint-Girons, and J. S. Roberts. Sub-500-fs soliton-like pulse in a passively mode-locked broadband surface-emitting laser with 100 mW average power. *Applied Physics Letters*, 80(21):3892–3894, 2002.

A. Garnache, A. A. Kachanov, F. Stoeckel, and R. Houdré. Diode-pumped broad-band vertical-external-cavity surface-emitting semiconductor laser applied to high-sensitivity intracavity absorption spectroscopy. *J. Opt. Soc. Am. B*, 17(9):1589–1598, Sep 2000.

A Garnache, A Ouvrard, and D Romanini. Single-Frequency operation of External-Cavity VCSELs: Non-linear multimode temporal dynamics and quantum limit. *Optics express*, 15(15):9403–9417, 2007.

A. Garnache, B. Sermage, R. Teissier, G. Saint-Giro, and I. Sagnes. A new kind of fast quantum-well semiconductor saturable-absorber mirror with low losses for ps pulse generation. In *Indium Phosphide and Related Materials, 2003. International Conference on*, pages 247–250, May 2003.

Anastassia Gosteva, Markus Haiml, Ruediger Paschotta, and Ursula Keller. Noise-related resolution limit of dispersion measurements with white-light interferometers. *Journal of the Optical Society of America B*, 22(9):1868, 2005.

Philippe Grelu and Nail Akhmediev. Dissipative solitons for mode-locked lasers. *Nature Photonics*, 6(2):84–92, February 2012.

Jörg Hader, Tsuei Lian Wang, J. Michael Yarborough, Colm a. Dineen, Yushi Kaneda, Jerome V. Moloney, Bernardette Kunert, Wolfgang Stolz, and Stephan W. Koch. VECSEL optimization using microscopic many-body physics. *IEEE Journal on Selected Topics in Quantum Electronics*, 17(6):1753–1762, 2011.

M. Haiml, R. Grange, and U. Keller. Optical characterization of semiconductor saturable absorbers. *Applied Physics B*, 79(3):331–339, June 2004.

Antti Härkönen, Jussi Rautiainen, Lasse Orsila, Mircea Guina, Karl Rößner, Michael Hümmer, Thomas Lehnhardt, Mirjam Müller, Alfred Forchel, Marc Fischer, Johannes Koeth, and Oleg G. Okhotnikov. 2-m Mode-Locked Semiconductor Disk Laser Synchronously Pumped Using an Amplified Diode Laser. *IEEE Photonics Technology Letters*, 20(15):1332–1334, 2008.

Jennifer Hastie, Stephane Calvez, Martin Dawson, Tomi Leinonen, Antti Laakso, Jari Lyytikäinen, and Markus Pessa. High power CW red VECSEL with linearly polarized TEM00 output beam. *Optics express*, 13(1):77–81, January 2005.

Herman Haus. Mode-Locking of Lasers. *IEEE Journal on Selected topics in Quantum Electronics*, 6(6):1173–1185, 2000.

C Robin Head, Keith G Wilcox, Andrew P Turnbull, Oliver J Morris, Edward a Shaw, and Anne C Tropper. Saturated gain spectrum of VECSELs determined by transient measurement of lasing onset. *Optics express*, 22(6):6919–24, March 2014.

Christopher Robin Head, Ho Yin Chan, James S. Feehan, David P. Shepherd, Shaif Ul Alam, Anne C. Tropper, Jonathan H V Price, and Keith G. Wilcox. Supercontinuum generation with GHz repetition rate femtosecond-pulse fiber-amplified VECSELs. *IEEE Photonics Technology Letters*, 25(5):464–467, 2013.

A. Hein, S. Menzel, and P. Unger. High-power high-efficiency optically pumped semiconductor disk lasers in the green spectral region with a broad tuning range. *Applied Physics Letters*, 101(11), 2012.

B. Heinen, T.-L. Wang, M. Sparenberg, a. Weber, B. Kunert, J. Hader, S.W. Koch, J.V. Moloney, M. Koch, and W. Stolz. 106 W continuous-wave output power from vertical-external-cavity surface-emitting laser. *Electronics Letters*, 48(9):516, 2012.

Thomas Hochrein, Rafal Wilk, Michael Mei, Ronald Holzwarth, Norman Krumbholz, and Martin Koch. Optical sampling by laser cavity tuning. *Optics express*, 18(2): 1613–1617, 2010.

Martin Hoffmann, Oliver D Sieber, Deran J H C Maas, Valentin J Wittwer, Matthias Golling, Thomas Südmeyer, and Ursula Keller. Experimental verification of soliton-like pulse-shaping mechanisms in passively mode-locked VECSELs. *Optics express*, 18(10):10143–53, May 2010.

Martin Hoffmann, Oliver D Sieber, Valentin J Wittwer, Igor L Krestnikov, Daniil a Livshits, Yohan Barbarin, Thomas Südmeyer, and Ursula Keller. Femtosecond high-power quantum dot vertical external cavity surface emitting laser. *Optics express*, 19 (9):8108–16, April 2011.

S Hoogland, S Dhanjal, A C Tropper, J S Roberts, R Häring, R Paschotta, and U Keller. Passively Mode-Locked Diode-Pumped Surface-Emitting Semiconductor Laser. *IEEE Photonics Technology Letters*, 12(9):1135–1137, 2000.

Sjoerd Hoogland. *Optically-pumped vertical-external-cavity surface-emitting semiconductor lasers*. PhD thesis, University of Southampton, 2003.

Jack L. Jewell, J. P. Harbison, A. Scherer, Y. H. Lee, and L. T. Florez. Vertical-cavity surface-emitting lasers: Design, growth, fabrication, characterization. *IEEE Journal of Quantum Electronics*, 27(6):1332–1346, 1991.

S. Jin and H. Mavoori. Processing and properties of CVD diamond for thermal management. *Journal of Electronic Materials*, 27(11):1148–1153, November 1998.

FX Kaertner, LR Brovelli, D Kopf, M Kamp, GC Irio, and U Keller. Control of solid state laser dynamics by semiconductor devices. *Optical Engineering*, 34(7):2024–2036, 1995.

Hermann Kahle, Roman Bek, Matthias Heldmaier, Thomas Schwarzbäck, Michael Jetter, and Peter Michler. High optical output power in the UVA range of a frequency-doubled, strain-compensated AlGaInP-VECSEL. *Applied Physics Express*, 7(9), 2014.

F. X. Kärtner, I D Jung, and U Keller. Soliton mode-locking with saturable absorbers. *IEEE Journal on Selected Topics in Quantum Electronics*, 2(3):540–556, 1996.

U Keller, D A Miller, G D Boyd, T H Chiu, J F Ferguson, and M T Asom. Solid-state low-loss intracavity saturable absorber for Nd:YLF lasers: an antiresonant semiconductor Fabry-Perot saturable absorber. *Optics letters*, 17(7):505–507, 1992.

U Keller and A.C. Tropper. Passively modelocked surface-emitting semiconductor lasers. *Physics Reports*, 429:67–120, 2006.

Ursula Keller, Kurt J Weingarten, X K Franz, Daniel Kopf, Bernd Braun, Isabella D Jung, Regula Fluck, H Clemens, Nicolai Matuschek, and Juerg Aus Der Au. Semiconductor Saturable Absorber Mirrors (SESAMs) for Femtosecond to Nanosecond Pulse Generation in Solid-State Lasers. *IEEE Journal on Selected Topics in Quantum Electronics*, 2(3):435–453, 1996.

Alexander Klenner, Stéphane Schilt, Thomas Südmeyer, and Ursula Keller. Gigahertz frequency comb from a diode-pumped solid-state laser. *Optics Express*, 22(25):31008, 2014.

P. Klopp, U. Griebner, M. Zorn, and M. Weyers. Pulse repetition rate up to 92 GHz or pulse duration shorter than 110 fs from a mode-locked semiconductor disk laser. *Applied Physics Letters*, 98(7):071103, 2011.

Peter Klopp, Uwe Griebner, Martin Zorn, Andreas Klehr, Armin Liero, Markus Weyers, and Götz Erbert. Mode-locked InGaAs-AlGaAs disk laser generating sub-200-fs pulses, pulse picking and amplification by a tapered diode amplifier. *Optics express*, 17(13):10820–34, June 2009.

L. Kornaszewski, G. Maker, G.P.a. Malcolm, M. Butkus, E.U. Rafailov, and C.J. Hamilton. SESAM-free mode-locked semiconductor disk laser. *Laser & Photonics Reviews*, 6(6):L20–L23, November 2012.

Jahn-Chung Kuo, Jia-Min Shieh, Chin-Der Hwang, C.-S. Chang, Ci-Ling Pan, and Kaung-Hsiung Wu. Pulse-forming dynamics of a cw passively mode-locked Ti:sapphire/DDI laser. *Optics Letters*, 17(5):334, 1992.

M Kuznetsov, F Hakimi, R Sprague, and A Mooradian. High-Power (¿0.5-W CW) Diode-Pumped Vertical-External-Cavity Surface-Emitting Semiconductor Lasers with Circular TEM00 Beams. *IEEE Photonics Technology Letters*, 9(8):1063–1065, 1997.

Alexandre Laurain, Maik Scheller, Tsuei-Lian Wang, Jorg Hader, Jerome V. Moloney, Stephan W. Koch, Bernd Heinen, Martin Koch, Bernardette Kunert, and Wolfgang Stolz. Recent advances in power scaling of high-power optically-pumped semiconductor lasers for ultrashort pulse generation and continuous wave single frequency operation, 2013.

Hans Lindberg, Martin Strassner, Jörgen Bengtsson, and Anders Larsson. High-power optically pumped 1550-nm VECSEL with a bonded silicon heat spreader. *IEEE Photonics Technology Letters*, 16(5):1233–1235, 2004.

D J Maas, B Rudin, a R Bellancourt, D Iwaniuk, S V Marchese, T Südmeyer, and U Keller. High precision optical characterization of semiconductor saturable absorber mirrors. *Optics express*, 16(10):7571–9, May 2008.

D. J H C Maas, a. R. Bellancourt, B. Rudin, M. Golling, H. J. Unold, T. Südmeyer, and U. Keller. Vertical integration of ultrafast semiconductor lasers. *Applied Physics B: Lasers and Optics*, 88(4):493–497, 2007.

A. J. Maclean, R. B. Birch, P. W. Roth, a. J. Kemp, and D. Burns. Limits on efficiency and power scaling in semiconductor disk lasers with diamond heatspreaders. *Journal of the Optical Society of America B*, 26(12):2228, November 2009.

Mario Mangold, Valentin J Wittwer, Oliver D Sieber, Martin Hoffmann, Igor L Krestnikov, Daniil a Livshits, Matthias Golling, Thomas Südmeyer, and Ursula Keller. VECSEL gain characterization. *Optics express*, 20(4):4136–48, February 2012.

Mario Mangold, Valentin J Wittwer, Christian A Zaugg, Sandro M Link, Matthias Golling, Bauke W Tilma, and Ursula Keller. Femtosecond pulses from a modelocked integrated external-cavity surface emitting laser (MIXSEL). *Optics Express*, 21(21): 24904–24911, 2013.

Mario Mangold, Christian A. Zaugg, Sandro M. Link, Matthias Golling, Bauke W. Tilma, and Ursula Keller. Pulse repetition rate scaling from 5 to 100 GHz with a high-power semiconductor disk laser. *Optics Express*, 22(5):6099, 2014.

Zakaria Mihoubi, Keith G Wilcox, Stephen Elsmere, Adrian Quarterman, Rakchanok Rungsawang, Ian Farrer, Harvey E Beere, David a Ritchie, Anne Tropper, and Vasileios Apostolopoulos. All-semiconductor room-temperature terahertz time domain spectrometer. *Optics letters*, 33(18):2125–2127, 2008.

J V Moloney, I Kilen, A Bäumner, M Scheller, and S W Koch. Nonequilibrium and thermal effects in mode- locked VECSELs. *Optics express*, 22(6):6422–6427, 2014.

U Morgner, F X Kärtner, S H Cho, Y Chen, H a Haus, J G Fujimoto, E P Ippen, V Scheuer, G Angelow, and T Tschudi. Sub-two-cycle pulses from a Kerr-lens mode-locked Ti:sapphire laser. *Optics letters*, 24(6):411–413, 1999.

Oliver J Morris. *Cryogenic operation and room temperature application of an optically-pumped surface-emitting semiconductor laser*. PhD thesis, University of Southampton, 2014.

Oliver J. Morris, Robert J. A. Francis-Jones, Keith G. Wilcox, Anne C. Tropper, and Peter J. Mosley. Photon-pair generation in photonic crystal fibre with a 1.5GHz modelocked VECSEL. *Optics Communications*, 327:39–44, 2014.

M. Mvara, M. Sellahi, a. Laurain, a. Garnache, a. Michon, and I. Sagnes. Noise properties of NIR and MIR VeCSELs. *2013 22nd International Conference on Noise and Fluctuations, ICNF 2013*, 2013.

Oleg G. Okhotnikov. *Semiconductor Disk Lasers: Physics and Technology*. Wilet-VCH, 2010.

Andrey G. Okhrimchuk and Petr a. Obraztsov. 11-GHz waveguide Nd:YAG laser CW mode-locked with single-layer graphene. *Scientific Reports*, 5:11172, 2015.

W. P. Pallmann, C. A. Zaugg, M. Mangold, I. Dahhan, M. Golling, B. W. Tilma, B. Witzigmann, and U. Keller. Ultrafast electrically pumped VECSELs. *IEEE Photonics Journal*, 5(4), 2013.

R Paschotta. Noise of mode-locked lasers (Part I): numerical model. *Applied Physics B-Lasers and Optics*, 79:153–162, 2004.

R. Paschotta, R. Häring, A. Garnache, S. Hoogland, A. C. Tropper, and U. Keller. Soliton-like pulse-shaping mechanism in passively mode-locked surface-emitting semiconductor lasers. *Applied Physics B: Lasers and Optics*, 75(4-5):445–451, 2002.

R. Paschotta and U. Keller. Passive mode locking with slow saturable absorbers. *Applied Physics B: Lasers and Optics*, 73(7):653–662, 2001.

Selina Pekarek, Alexander Klenner, Thomas Südmeyer, Christian Fiebig, Katrin Paschke, Götz Erbert, and Ursula Keller. Femtosecond diode-pumped solid-state laser with a repetition rate of 4.8 GHz. *Optics Express*, 20(4):4248, 2012.

Selina Pekarek, Thomas Südmeyer, Steve Lecomte, Stefan Kundermann, John M. Dudley, and Ursula Keller. Self-referenceable frequency comb from a gigahertz diode-pumped solid-state laser. *Optics Express*, 19(17):16491, 2011.

A. H. Quarterman, M. A. Tyrk, and K. G. Wilcox. Z-scan measurements of the nonlinear refractive index of a pumped semiconductor disk laser gain medium. *Applied Physics Letters*, 106(1):011105, 2015.

Adrian H Quarterman, Keith G Wilcox, Vasilis Apostolopoulos, Zakaria Mihoubi, Stephen P Elsmere, Ian Farrer, David A Ritchie, and Anne Tropper. A passively mode-locked external-cavity semiconductor laser emitting 60-fs pulses. *Nature Photonics*, 3(November):729–731, 2009.

Adrian H. Quarterman, Keith G. Wilcox, Alex Perevedentsev, Vasilis Apostolopoulos, Zakaria Mihoubi, Aaron L. Chung, Harvey E. Beere, Ian Farrer, David a. Ritchie, and Anne C. Tropper. 169 GHz repetition rate passively harmonically mode-locked VECSEL emitting 265 fs pulses. In *SPIE*, volume 7919, pages 791910–791910–7, 2011.

A.H. Quarterman and K. G. Wilcox. Design of a solar-pumped semiconductor laser. *Optica*, 2(1):56–61, 2015.

M. Rahim, a. Khiar, F. Felder, M. Fill, H. Zogg, and M. W. Sigrist. 5-μm vertical external-cavity surface-emitting laser (VECSEL) for spectroscopic applications. *Applied Physics B*, 100(2):261–264, June 2010.

Sanna Ranta, Antti Härkönen, Tomi Leinonen, Lasse Orsila, Jari Lyytikäinen, Günter Steinmeyer, and Mircea Guina. Mode-locked VECSEL emitting 5 ps pulses at 675 nm. *Optics letters*, 38(13):2289–2291, 2013.

Jussi Rautiainen, Ville-Markus Korpijärvi, Janne Puustinen, Mircea Guina, and Oleg Okhotnikov. Passively mode-locked GaInNAs disk laser operating at 1220 nm. *Optics express*, 16(20):15964–15969, 2008.

B Rudin, V J Wittwer, D J H C Maas, M Hoffmann, O D Sieber, Y Barbarin, M Golling, T Südmeyer, and U Keller. High-power MIXSEL: an integrated ultrafast semiconductor laser with 6.4 W average power. *Optics express*, 18(26):27582–8, December 2010.

E.J. Saarinen, A. Rantamaki, A. Chamorovskiy, and O.G. Okhotnikov. 200GHz 1W semiconductor disc laser emitting 800fs pulses. *Electronics Letters*, 48(21):1355, 2012.

Esa J Saarinen, Valery Filippov, Yuri Chamorovskiy, Konstantin Golant, Miki Tavast, Antti Rantamäki, and Oleg G Okhotnikov. 193-GHz 53-W Subpicosecond Pulse Source. *IEEE Photonics Technology Letters*, 27(7):778–781, 2015.

C. J. Saraceno, C. Schriber, M. Mangold, M. Hoffmann, O. H. Heckl, C. R. E. Baer, M. Golling, T. Sudmeyer, and U. Keller. SESAMs for high power oscillators: Damage thresholds and design guidelines. *IEEE Journal of Selected Topics in Quantum Electronics*, 18(1):29–41, 2011.

Nobuhiko Sarukura and Yuzo Ishida. Pulse evolution dynamics of a femtosecond passively mode-locked Ti:sapphire laser. *Optics Letters*, 17(1):61, January 1992.

M. Scheller, T.-L. Wang, B. Kunert, W. Stolz, S.W. Koch, and J.V. Moloney. Passively modelocked VECSEL emitting 682fs pulses with 5.1W of average output power. *Electronics Letters*, 48(10):588, 2012.

Maik Scheller, Caleb W. Baker, Kokou Gbele, Stephan W. Koch, R. Jason Jones, and Jerome V. Moloney. Ultrafast in-situ probing of passively mode-locked VECSEL dynamics. *SPIE: VECSELs V*, 9349:93490H, 2015.

Maik Scheller, Joe M Yarborough, Jerome V Moloney, Mahmoud Fallahi, Martin Koch, and Stephan W Koch. Room temperature continuous wave milliwatt terahertz source. *Optics express*, 18(26):27112–27117, 2010.

E.F. Schubert. *Light-emitting diodes*. Proceedings of SPIE - The International Society for Optical Engineering. Cambridge University Press, 2006.

Nicola Schulz, John Mark Hopkins, Marcel Rattunde, David Burns, and Joachim Wagner. High-brightness long-wavelength semiconductor disk lasers. *Laser and Photonics Reviews*, 2(3):160–181, July 2008.

O. D. Sieber, V. J. Wittwer, M. Hoffmann, I. L. Krestnikov, S. S. Mikhrin, D. A. Livshits, M. Golling, T. Suedmeyer, and U. Keller. High-average power femtosecond VECSELs

with tunable repetition rates up to 10 GHz. volume 8242 of *Proceedings of SPIE*. SPIE, 2012.

Oliver D. Sieber, Martin Hoffmann, Valentin J. Wittwer, Mario Mangold, Matthias Golling, Bauke W. Tilma, Thomas Südmeyer, and Ursula Keller. Experimentally verified pulse formation model for high-power femtosecond vecsels. *Applied Physics B*, 113(1):133–145, 2013.

Oliver D. Sieber, Valentin J. Wittwer, Mario Mangold, Martin Hoffmann, Matthias Golling, Thomas Südmeyer, and Ursula Keller. Femtosecond VECSEL with tunable multi-gigahertz repetition rate. *Optics Express*, 19(23):23538, 2011.

A.E. Siegman. *Lasers*. University Science Books, 1986.

Jinghua Sun, Ruobing Zhang, Qingyue Wang, Lu Chai, Dongqing Pang, Jianming Dai, Zhigang Zhang, Kenji Torizuka, Tadashi Nakagawa, and Takeyoshi Sugaya. Ti:Sapphire laser with a broadband semiconductor saturable-absorber mirror. *Applied Optics*, 40(21):3539–3541, 2001.

D H Sutter, G Steinmeyer, L Gallmann, N Matuschek, F Morier-Genoud, U Keller, V Scheuer, G Angelow, and T Tschudi. Semiconductor saturable-absorber mirror-assisted Kerr-lens mode-locked Ti : sapphire laser producing pulses in the two- cycle regime. *Optics Letters*, 24(9):631–633, 1999.

Dirk H Sutter, Isabella D Jung, X K Franz, Nicolai Matuschek, François Morier-genoud, V Scheuer, M Tilsch, T Tschudi, and Ursula Keller. Self-Starting 6.5-fs Pulses from a Ti:Sapphire Laser Using a Semiconductor Saturable Absorber and Double-Chirped Mirrors. *IEEE Journal of Selected Topics in Quantum Electronics*, 4(2):169–178, 1998.

O. Svelto. *Principles of lasers*. Springer, 2010.

Anne C. Tropper, Adrian H. Quarterman, and Keith G. Wilcox. *Ultrafast Vertical-External-Cavity Surface-Emitting Semiconductor Lasers*, volume 86. Elsevier Inc., 1 edition, 2012.

C.E. Webb and J.D.C. Jones. *Handbook of laser technology and applications: Applications*. Handbook of Laser Technology and Applications. Institute of Physics, 2004.

K. G. Wilcox, A. H. Quarterman, H. E. Beere, D. A. Ritchie, and A. C. Tropper. Variable repetition frequency femtosecond-pulse surface emitting semiconductor laser. *Applied Physics Letters*, 99(13):131107, 2011a.

Keith G Wilcox. *Ultrashort pulse surface emitting semiconductor lasers*. PhD thesis, University of Southampton, 2006.

Keith G Wilcox, Zakaria Mihoubi, G J Daniell, Stephen Elsmere, Adrian Quarterman, Ian Farrer, David A Ritchie, and Anne C Tropper. Ultrafast optical Stark mode-locked semiconductor laser. *Optics letters*, 33(23):2797–2799, 2008.

Keith G. Wilcox, Adrian H. Quarterman, Vasilis Apostolopoulos, Harvey E. Beere, Ian Farrer, David a. Ritchie, and Anne C. Tropper. 175 GHz, 400-fs-pulse harmonically mode-locked surface emitting semiconductor laser. *Optics Express*, 20(7):7040–7045, 2012.

Keith G Wilcox, Adrian H Quarterman, Harvey Beere, David A Ritchie, and Anne C Tropper. High Peak Power Femtosecond Pulse Passively Mode-locked Vertical-External-Cavity Surface-Emitting Laser. *IEEE Photonics Technology Letters*, 22(14): 1021–1023, 2010a.

Keith G Wilcox, Adrian H Quarterman, Harvey E Beere, David A Ritchie, and Anne C Tropper. Repetition-frequency-tunable mode-locked surface emitting semiconductor laser between 2.79 and 7.87 GHz. *Optics express*, 19(23):23453–23459, 2011b.

Keith G. Wilcox and Anne C. Tropper. Comment on SESAM-free mode-locked semiconductor disk laser. *Laser & Photonics Reviews*, 7(3):422–423, May 2013.

Keith G Wilcox, Anne C Tropper, Harvey E Beere, David A Ritchie, Bernd Heinen, and Wolfgang Stolz. 4.35 kW peak power femtosecond pulse mode-locked VECSEL for supercontinuum generation. *Optics express*, 21(2):1599–1605, 2013.

K.G. Wilcox, A.H. Quarterman, S. Carswell, Z. Mihoubi, V. Apostolopoulos, A. Chung, and A. Tropper. Mode-locking build-up measurements: probing the mode-locking-mechanisms in vertical-external-cavity surface-emitting lasers. In *Lasers and Electro-Optics (CLEO) and Quantum Electronics and Laser Science Conference (QELS), 2010 Conference on*, pages 1–2, May 2010b.

C. A. Zaugg, S. Gronenborn, H. Moench, M. Mangold, M. Miller, U. Weichmann, W. P. Pallmann, M. Golling, B. W. Tilma, and U. Keller. Absorber and gain chip optimization to improve performance from a passively modelocked electrically pumped vertical external cavity surface emitting laser. *Applied Physics Letters*, 104(12):1–5, 2014a.

CA Zaugg, Alexander Klenner, and Mario Mangold. Gigahertz self-referenceable frequency comb from a semiconductor disk laser. *Optics Express*, 22:1332–1334, 2014b.

Christian A. Zaugg, Alexander Klenner, Oliver D. Sieber, Matthias Golling, Bauke W. Tilma, and Ursula Keller. Sub-100 mhz passively modelocked vecsel. In *CLEO: 2013*, page CW1G.6. Optical Society of America, 2013.

Rong Zhao, Wai Shing Lau, Tow Chong Chong, and Ming Fu Li. A comparison of the selective etching characteristics of conventional and low-temperature-grown gaas over alas by various etching solutions. *Japanese Journal of Applied Physics*, 35(1R):22, 1996.

Zinkiewicz, F Ozimek, and P Wasylczyk. Witnessing the pulse birthtransient dynamics in a passively mode-locked femtosecond laser. *Laser Physics Letters*, 10(12):125003, December 2013.

M. Zorn, P. Klopp, F. Saas, A. Ginolas, O. Krüger, U. Griebner, and M. Weyers. Semiconductor components for femtosecond semiconductor disk lasers grown by MOVPE. *Journal of Crystal Growth*, 310(23):5187–5190, November 2008.

Appendix A: List of Publications

Turnbull, A. P., Head, C. R., Shaw. E. A., Chen-Sverre, T. and Tropper, A. C.(2013). Spectrally resolved pulse evolution in a mode-locked vertical-external-cavity surface-emitting laser from lasing onset measurements. *Proceedings of SPIE Photonics West, San Francisco, USA (6 February, 2015)*, 93490I.

Turnbull, A. P., Wilcox, K. G., Head, C. R., Morris, O. J., Farrer, I., Ritchie, D. A. and Tropper, A. C.(2013). Generation of 200-fs pulses with a short microcavity VECSEL. *Proceedings of SPIE Photonics West, San Francisco, USA (18 February, 2013)*, 86060O.

Head, C Robin and Wilcox, Keith G and Turnbull, Andrew P and Morris, Oliver J and Shaw, Edward A and Tropper, Anne C Saturated gain spectrum of VECSELs determined by transient measurement of lasing onset. *Optics express*, 22(6):6919–24.

Head, C.R.; Hein, A.; Shaw, E.A.; Turnbull, A.P.; Unger, P.; Tropper, A.C. Femtosecond mode-locked VECSEL from widely cw-tunable gain chips. Conference on Laser and Electro-Optics CLEO/US, San Jose,(8-13 June 2014)

Head, C. R., Wilcox, K. G., Morris, O. J., Turnbull, A. P., Farrer, I., Beere, H. E., Ritchie, D. A. and Tropper, A. C.(2013). Spectral gain and cavity loss characterization of an optically-pumped external-cavity surface-emitting quantum well laser. *Conference on Laser and Electro-Optics CLEO/Europe, Munich, Germany (12-16 May 2013)*,

Morris, O. J., Wilcox, K. G., Head, C. R., Turnbull, A. P., Farrer, I., Beere, H. E., Ritchie, D. A. and Tropper, A. C.(2013). Effects of cryogenic temperatures on the performance of CW VECSELs. *Proceedings of SPIE Photonics West, San Francisco, USA (18 February, 2013)*, 86060L.

Morris, O. J., Wilcox, K. G., Head, C. R., Turnbull, A. P., Mosley, P. J., Quarterman, A. H., Kbashi, H. J., Farrer, I. Beere, H. E., ritchie, D. A., and Tropper, A. C. (2012). A wavelength tuneable 2-ps pulse VECSEL *Proceedings of SPIE Photonics West, San Francisco, USA (9 February, 2012)* 824212

Wilcox, K. G., Quarterman, A. H., Apostolopoulos, V., Morris, O. J., Head, C. R., Turnbull, A. P., Beere, H. E., Farrer, I., Ritchie, D. A., and Tropper, A. C. (2012). Femtosecond semiconductor laser emitting high average power 175-GHz pulse train. *Conference on Lasers and Electro-Optics CLEO/US, San Jose, USA (6-11 May, 2012)*, JW2A.102